공학박사학위논문

Numerical Analysis on the Unsteady Flow Characteristics in Insects' Flapping Flight

곤충 날갯짓 비행에서 발생하는 비정상 유동 현상에 대한 수치적 연구

2014년 2월

서울대학교 대학원
계산과학 협동과정
이 근 배

Numerical Analysis on the Unsteady Flow Characteristics in Insects' Flapping Flight

곤충 날갯짓 비행에서 발생하는 비정상 유동 현상에 대한 수치적 연구

지도교수 김 종 암

이 논문을 공학박사학위 논문으로 제출함
2013 년 12 월

서울대학교 대학원
계산과학 협동과정
이 근 배

이근배의 공학박사학위 논문을 인준함
2013 년 12 월

위 원 장 : _____

부위원장 : _____

위 원 : _____

위 원 : _____

위 원 : _____

Abstract

The present thesis investigates the unsteady flow characteristics in insects' flapping motion under forward flight condition. A realistic wing trajectory, called the 'figure-of-eight' motion, is extracted from a blowfly's (*Phormia regina*) tethered flight experiment. In the preliminary research, the two- and three-dimensional blowfly's wing motion were numerically investigated, and the results revealed interesting and distinctive vortical flow fields, which provided a decisive clue in understanding the rapid maneuverability of insect's flight. Based on the previous work, two primary topics are discussed: the aerodynamic effect of structural flexibility in two-dimensional flapping wing motion and the three-dimensional unsteady aerodynamic features of wing-body-vortex interactions in insects' flapping flight.

Interaction between a flexible flapping wing and the ambient fluid is of considerable importance in realistic flapping flight. In order to examine realistic flow features of insects' flapping motion and to investigate aerodynamic change due to structural flexibility of insect wing, two-dimensional FSI (Fluid-Structure Interaction) simulations are conducted under a forward flight condition. Three types of airfoils are considered to reflect structural deformation. Compared with earlier studies regarding two-dimensional rigid airfoil simulations, the same key physical phenomena and flow patterns could be observed in flexible case. On the other hand, the quantitative aspect of flow fields is somewhat different. Structural deformation does affect aerodynamic force generation pattern, and thus structural flexibility has a significant impact on aerodynamic performance. Aerodynamic force coefficient and propulsive efficiency

are enhanced compared to the case of a rigid airfoil. In addition, numerical simulations are performed to inspect effects of aerodynamic parameters such as the Reynolds number and reduced frequency. From extensive numerical comparisons, it is observed that key physical phenomena such as vortex pairing and vortex staying are still observed in other flow conditions.

Three-dimensional unsteady aerodynamic features of wing-body-vortex interactions and the effects of geometric factors, such as wing shape and body angle, in insects' flapping motions are investigated under forward flight condition. From the authors' previous researches on two- and three-dimensional rigid wing simulation, it has been observed that the pattern of vortical flows and the interaction of vortices play a significant role in generating unsteady aerodynamic forces and determining the propulsive efficiency of flapping motion. Detailed numerical simulations of five types of wings are carried out under various body angles to examine unsteady flow characteristics resulting from the complicated wing-body-vortex interactions, and the results are compared with those of the wing only case. From numerical results, there exist three kinds of interactions in three-dimensional full-body simulations: wing-vortex interactions, vortex-vortex interactions and wing-body interactions. Also, it is revealed that realistic geometric considerations have a considerable influence on the aerodynamic force generation in insects’ flapping flight.

Consequently, the aerodynamic effects of structural flexibility analyzed in this work can be beneficially exploited in the development of flapping micro-aerial-vehicles. Also, complicated wing-body interactions and geometric factors, such as body angle and wing shape, should be considered for investigating the aerodynamic

performance of flapping flight and this can be used in the design of small sized aerial-vehicles as well.

Keywords: CFD, FSI simulation, Insect flight, Unsteady flow, Aerodynamic force generation, Wing trajectory, Vortex pairing, Vortex ring, Small-sized flapping aerial-vehicles

Student number: 2009-30870

Name: Lee, Kuen-Bae

Table of Contents

Nomenclature

English Symbols

$\hat{A}, \hat{B}, \hat{C}$	inviscid flux Jacobian
c	reference chord
C_d	drag coefficient
C_l	lift coefficient
C_p	power input coefficient
C_t	thrust coefficient
$\hat{E}, \hat{F}, \hat{G}$	inviscid flux vector
$\hat{E}_v, \hat{F}_v, \hat{G}_v$	viscous flux vector
F	force
f	flapping frequency in Hertz
I	identity matrix
J	transformed Jacobian
k	reduced frequency in terms of c_m
P	power input
p	pressure
Q	conservative variable vector
Str	Strouhal number
Re	Reynolds number
t	non-dimensional time
T	non-dimensional flapping period
u, v, w	velocity

U, V, W	contravariant velocity
x, y, z	Cartesian coordinate
$x(t)$	lagging motion (horizontal direction motion)
$y(t)$	translation motion (vertical direction motion)
h_a	dimensionless plunging amplitude
$[M]$	mass matrix
$[C]$	damping matrix
$[K]$	stiffness matrix
$\{U\}$	nodal displacement
$\{F\}$	external aerodynamic load
E	modulus of elasticity
N_s^j	shape function
e_c	a number of sub-element
$\tilde{t}_f$	force vector on fluid mesh
R_s^j	force vector on solid mesh
e_i	area coefficient
S	area of the Delaunay graph

Greek Symbols

α	angle of attack
β	pseudo-compressibility parameter
λ	eigenvalues
μ	molecular viscosity
ν	kinematic molecular viscosity
ρ	density

τ	pseudo time
$\tau_{i,j,k}$	molecular stress tensor
$\hat{\tau}_{i,j,k}$	Reynolds stress tensor
η	propulsive efficiency
ξ, η, ζ	generalized curvilinear coordinates
$\alpha(t)$	pitch angle motion
Γ	common refinement boundary

Mathematical Symbol

∇	gradient
Δ	increment

Subscripts

i, j,k	grid indices
v	viscous
∞	freestream condition
m	mean value
n	normal direction
t	tangential direction

List of Tables

List of Figures

Chapter I
Introduction

1.1 Research Background

There are nearly a million different species of insects flying with flapping wings and 10,000 types of birds and bats flapping their wings for locomotion. Among them, insects have evolved over 270 million years and their elaborate flight mechanism has been a subject of great interest to scientists and engineers in various scientific fields, such as biology, ecology, morphology, engineering, and so on. In particular, insects' flapping flight has been regarded as one of the most fascinating research subjects in the field of unsteady aeronautics because of its potential applicability to various propulsive devices or next-generation flying vehicles [1]. Many researchers have conducted experimental and/or numerical studies to uncover the curious unsteady characteristics of insects' flapping flight.

Experimental works on insect's wing motions have been carried out, among others, by Ellington *et al*. [2], Ward-smith [3], Dickinson *et al*. [4, 5], Singh and Chopra [6], Nagai and Isogai [7], Okamoto and Azuma [8]. Ellington *et al*. [2] observed the leading edge vortex (LEV) using smoke visualization around both a real moth and a 3-D model at the Reynolds number of $O(10^3)$. They observed a strong vortex attached at leading-edge during downstroke motion. As another lift generation mechanism, vortical pattern produced by the 'clap-fling' motion [3] was studied. Dickinson *et al*. [4, 5] measured unsteady aerodynamic forces, and visualized flow patterns in an oil tank using a dynamically scaled mechanical model. They observed

two important lift enhancement mechanisms. The first one, called ‘rotational circulation,’ is analogous to the *Magnus effect* observed in a rotating circular cylinder. The second one, called ‘wake capture,’ comes from the interaction between wing and shedding vortex by wing rotation. Singh and Chopra [6] devised an insect-based hover-capable experimental apparatus, and measured the thrust generated by a number of wing designs at different pitch angles. Nagai and Isogai [7] measured time-varying aerodynamic forces on the flapping wing in hovering and forward flight using a dynamically scaled mechanical model in a water tunnel, and examined the effects of wing kinematics on the aerodynamic characteristics of a flapping insects’ wing. Also, Okamoto and Azuma [8] conducted wind tunnel tests to examine the unsteady aerodynamic characteristics of various wing planforms such as elliptic, rectangular, and triangular with various aspect ratios at low Reynolds numbers. Though experimental works help to understand global flow phenomena, it often fails to describe the detailed flow fields due to difficulties in modeling insect's wing motion and visualizing three-dimensional vortex structures.

Computational studies have thus been performed in parallel by several researchers. Sun and Yu [9] numerically simulated a two-dimensional 'clap-fling' motion of a tiny insect using a Navier-Stokes solver, and showed that a sufficiently large amount of lift could be generated. Liu and Kawachi [10] verified the LEV of a moth (Manduca sexta) wing under hovering flight by three-dimensional computations. Ramamurti [11] also performed three-dimensional computational study on the flapping wing of the modeled fruit fly. Lee *et al*. [12] designed an optimal flapping airfoil sustaining both high propulsive efficiency and thrust coefficient based on the understanding on the role of leading-edge and trailing-edge vortices. Furthermore, they explained the impulsive thrust generation mechanism of insects’ forward flight by examining a two-dimensional vortical flow field [13]. Some review study on

recent developments in flapping-wing aerodynamics has been carried out by Platzer *et al*. [14]. However, most of previous computational works have mainly focused on ‘two-dimensional motion’ and/or ‘hovering flight’. Recently, unsteady aerodynamics of insect’s forward flight have been studied by three-dimensional computational approaches, due to notable advances in modern CFD techniques and rapid growth of available computing power. Wang and Sun [15] conducted numerical simulations of the flapping wing of a dragonfly under forward flight. Unsteady aerodynamic features and forewing-hindwing interactions of a dragonfly were computed using a three-dimensional Navier-Stokes solver. Ramamurti and Sandberg [16] performed three-dimensional unsteady computations of a maneuvering fruit fly, and investigated the effect of kinematic difference between the right and left wings. Kim *et al*. [17] conducted three-dimensional unsteady simulation of a blowfly’s forward flight, and unveiled the role of three-dimensional vortical structure in unsteady aerodynamic force generation. Swanson and Isaac [18] investigated planform and camber effects on unsteady aerodynamics of three-dimensional wing in constant freestream at various angles of attack and low Reynolds number. Four types of wings were simulated to identify dominant flow features around each wing. Liu [19] developed a computational framework for modeling insect flapping flights by integrating body–wing morphology, kinematics, and unsteady aerodynamic Navier-Stokes solver. Yu and Sun [20] simulated the flows of a model fruit fly under typical hovering and forward flight conditions, and reported that the interaction between the contra-lateral wings and the interaction between the body and wings were very weak. Aono *et al*. [21] compared the results of the wing-body system with those of the wing only case, and showed that the effects of the body on the aerodynamic forces of the wings were rather small.

Previous studies have explained many interesting aspects of flapping motions, but unsteady flow fields characteristics of three-dimensional flapping motions under forward flight condition, such as wing-vortex, vortex-vortex, and wing-body interaction phenomena, have not been clearly examined yet. Due to demanding computational cost for three-dimensional unsteady simulation, most researchers have focused on global physical phenomena involving wing-body configuration with a relatively small number of grid points. For this reason, some preliminary researchers might rush to a conclusion that the interactions between wing and body were very weak. This makes explicit the necessity of high-fidelity flow simulations to capture detailed flow physics caused by wing-body-vortex interactions. Also, some researchers have conducted experiments and numerical simulations to investigate the effects of wing geometry on unsteady aerodynamic characteristics. They considered a simple geometry of wing such as an ellipse, rectangular, and triangular shape and only covered a fixed wing motion, not a flapping wing motion. From this perspective, further study is necessary to understand the aerodynamic force generation in flapping flight caused by geometric factors such as realistic wing planform and sectional shape.

Meanwhile, only a few studies have been attempted on realistic flexible flapping motion. Experimental studies on flexible flapping airfoils were carried out by Heathcote and Gursul [22]. They visualized flow fields around a chordwise flexible 2-D airfoil oscillating in heave at low Reynolds numbers, and measured thrust and propulsive efficiency. In addition, they observed an optimal thickness of the airfoil and the plunging frequency that produced the highest thrust and propulsive efficiency. Aside from experimental studies, some researchers have conducted computational works around flexible flapping airfoils. Pederzani and Haj-Hariri [23] investigated the effect of chordwise flexibility on heaving airfoils using a FSI numerical model for 2-D unsteady viscous flows around a flexible body. They observed that the change of

the flow fields by the flexible airfoil altered the forces acting on the airfoil in a way that the flexible airfoil was more efficient than the rigid one for different plunging frequency. Olivier *et al*. [24] carried out some test simulations using a vortex-excited elastic plate behind a bluff body, and presented preliminary results on flexible flapping wings. Chandar and Damodaran [25] performed FSI simulations for predicting the deformation of a flapping wing due to aerodynamic forces. Shyy *et al*. [26] conducted numerical simulation to examine the flow field around a flexible plunging airfoil under incoming flow and to observe the dynamic fluid characteristics and the mechanism of thrust generation. Effect of airfoil flexibility has been considered by coupling a finite element structural solver using beam elements with a fluid solver using Navier-Stokes equations.

Earlier works for flexible flapping motion have made meaningful progresses in understanding the unsteady flow characteristics of flexible flapping airfoils. However, further study is essential especially in addressing the aerodynamic force generation caused by structural flexibility which will definitely change local behaviors in thrust and propulsive efficiency. In addition, compared with studies of flexible airfoils under sinusoidal flapping motion (or combined pitching and heaving) [22-26], there are few results dealing with motions of flexible insect wings under realistic flight conditions such as forward flight and/or rapid maneuvering.

1.2 Research Strategy

In the authors' preliminary research efforts [12, 13, 17, 27-30], two- and three-dimensional rigid wing motions were simulated, and uncommon tendencies of vortex interactions and resulting flow patterns were observed, which provide a decisive clue for impulsive aerodynamic force generation of insects' flapping motion. Sufficient lift

generation is caused by a leading-edge vortex (LEV) due to a high effective angle of attack and a vortex staying phenomena. Impulsive thrust generation is closely related by vortex pairing in velocity field and vortex staying in pressure field, which is caused by the rotational component of 'figure-of-eight' motion. In the line with the same efforts, the present dissertation focuses on the investigation of more realistic and detailed flow physics in insects' flapping flight. Research strategy is established as depicted in Fig. 1.1. Based on the fundamental flow features, two kinds of research strategies are considered as an advanced and extended stage of the preliminary research.

The first one is to investigate realistic flow features of insects' flapping motion owing to structural flexibility. Detailed two-dimensional FSI simulations are conducted by using the loosely coupling approach. Based on elaborate structural modeling and realistic shape of insect wing, three types of airfoils are considered to reflect structural deformation. In addition, numerical simulations are performed to inspect the effects of aerodynamic parameters, such as the Reynolds number and reduced frequency.

Secondly, detailed three-dimensional numerical simulations of a blowfly's wing-body configuration are conducted to investigate unsteady flow physics and the effects of geometric factors, such as wing shape and body angle, in insects' flapping motions under forward flight condition. Five types of wings based on a real blowfly's wing and body shape are carried out under various body angles of attack (AOA) to examine unsteady flow characteristics resulting from the complicated wing-body-vortex interactions, and the results are compared with those of the wing only case.

1.3 Outline of Thesis

The present thesis is organized as follows.

The governing equations and numerical approaches for the simulation of an insects' flapping flight will be presented in chapter 2. In this chapter, accurate and efficient numerical techniques, including kinematic and geometric modeling for blowfly's flapping wing motion, will be introduced.

In chapter 3, the aerodynamic effects of structural flexibility in two-dimensional insects' flapping flight will be presented. This chapter includes a detailed investigation on the comparison of aerodynamic performance between rigid and flexible wing and on the aerodynamic effects by changing non-dimensional parameters, such as Reynolds number and reduced frequency.

After that, numerical analyses on three-dimensional wing-body configuration will be expressed in chapter 4. In this chapter, three-dimensional unsteady flow characteristics, such as wing-vortex, vortex-vortex, wing-body interactions, are investigated to identify the qualitative and quantitative difference between wing-body and wing only results and to examine the aerodynamic effects of geometric factors, such as wing shape and body angles.

Finally, this dissertation will be finished with a summary and discussion of future work based on the above mentioned studies.

Chapter II
Numerical Approach

2.1 Governing Equations

2.1.1 Fluid Part

The governing equations for compressible viscous fluid motion are given in a conservative form using Cartesian-tensor notation of

$$\frac{d\rho}{dt}+\frac{\partial}{\partial x_k}(\rho u_k)=0, \tag{2.1}$$

$$\frac{\partial(\rho u_i)}{\partial t}+\frac{\partial}{\partial x_j}(\rho u_i u_j)=-\frac{\partial p}{\partial x_i}+\frac{\partial}{\partial x_j}\left\{\mu\left(\frac{\partial u_i}{\partial x_j}+\frac{\partial u_j}{\partial x_i}-\frac{2}{3}\delta_{ij}\frac{\partial u_k}{\partial x_k}\right)\right\}. \tag{2.2}$$

where ρ is the density, u_i is the velocity component in x_i coordinate direction, p is the pressure, and μ is the absolute viscosity. Equations (2.1) and (2.2) are the equation of mass conservation and the equation of momentum conservation, respectively. It is necessary to include the equation of energy conservation along with the equation of state to give a complete description of the motion of a compressible fluid. But, the energy conservation equation does not need to be solved for incompressible flow problems unless the heat transfer on the boundaries and the temperature distribution in the flowfield are a matter of concern.

If the density of the flow is constant, Eq. (2.1) can be reduced to

$$\frac{\partial u_k}{\partial x_k} = 0, \tag{2.3}$$

and dividing Eq. (2.2) by density ρ result in

$$\frac{\partial u_i}{\partial t} + \frac{\partial}{\partial x_j}(u_i u_j) = -\frac{\partial p}{\partial x_i} + \frac{\partial}{\partial x_j}\left\{\nu\left(\frac{\partial u_i}{\partial x_j} + \frac{\partial u_j}{\partial x_i} - \frac{2}{3}\delta_{ij}\frac{\partial u_k}{\partial x_k}\right)\right\}, \tag{2.4}$$

where ν is the kinematic viscosity and the pressure *p* absorbs the density, i.e., $p = p/\rho$. The divergence of velocity is zero from Eq. (2.3), but it is left in Eq. (2.4) on purpose because the velocity field is not divergence free until the solution is converged. When the divergence free condition is applied and ν is assumed to be constant for laminar flow calculations, Eq. (2.4) is then reduced to

$$\frac{\partial u_i}{\partial t} + \frac{\partial}{\partial x_j}(u_i u_j) = -\frac{\partial p}{\partial x_i} + \nu\frac{\partial^2 u_i}{\partial x_j \partial x_j}. \tag{2.5}$$

It should be noted that Eqs. (2.3) and (2.5) give a complete description of the motion of an incompressible fluid. Thus, the equation of energy conversation will be solved only when necessary.

2.1.2 Solid Part

To obtain structural displacement in solid module, the dynamic finite element equations using a direct time-integration method are employed as the governing equations [31].

$$[M]\{\ddot{U}\}+[C]\{\dot{U}\}+[K]\{U\}=\{F\}. \tag{2.6}$$

In Eq. (2.6), [*M*], [*C*] and [*K*] represents the mass matrix, damping matrix, and stiffness matrix, respectively. {*U*} is the nodal displacement, and {*F*} denotes the external aerodynamic load applied to each node.

The direct time-integration method is to obtain the response history using step-by-step temporal integration without changing the form of the dynamic finite element equations. The temporal response is thus evaluated by marching the time increment of Δt.

With the time-step of Δt, velocity and acceleration at *n*-th time-step are replaced by conventional central differencing approximation, as follows.

$$\{\dot{U}\}_n=\frac{1}{2\Delta t}(\{U\}_{n+1}-\{U\}_{n-1}), \tag{2.7}$$

$$\{\ddot{U}\}_n=\frac{1}{\Delta t^2}(\{U\}_{n+1}-2\{U\}_n+\{U\}_{n-1}). \tag{2.8}$$

By inserting Eqs. (2.7) and (2.8) into Eq. (2.6), we have

$$\begin{aligned}&(\frac{1}{\Delta t^2}[M]+\frac{1}{2\Delta t}[C])\{U\}_{n+1}=\{F\}_n-[K]\{U\}_n\\&+\frac{1}{\Delta t^2}[M](2\{U\}_n-\{U\}_{n-1})+\frac{1}{2\Delta t}[C]\{U\}_{n-1}\end{aligned}. \tag{2.9}$$

The proper range of the allowable Δt is determined from the stability analysis, as follows.

$$\Delta t \le \frac{\Delta L}{\sqrt{E/\rho}}. \tag{2.10}$$

In Eq. (2.10), ΔL is the characteristic length of finite element, E is the Young's modulus, and ρ is the density of material.

2.2 Pseudo-Compressibility Method

One of the methods proposed for solving the incompressible Navier-Stokes equations in primitive variable form was the artificial compressibility method by Chorin [32, 33]. In this method, the continuity equation is modified to include an artificial compressibility term which vanishes when the steady-state solution is reached. With the addition of this term to the continuity equation, the resulting Navier-Stokes equations are mixed set of hyperbolic-parabolic equations, which can be solved using a standard time-dependent approach. The continuity equation is replaced by

$$\frac{\partial \rho^*}{\partial \tau} + \frac{\partial u_k}{\partial x_k} = 0, \tag{2.11}$$

where ρ^* is an artificial density and τ is a fictitious time that is analogous to real time in a compressible flow. The artificial density is replaced to the pressure by the artificial equation of state

$$p^* = \beta \rho^* , \tag{2.12}$$

where β is the artificial compressibility factor.

To relate the pressure fields with the velocity fields, the artificial compressibility relation is introduced by adding a pseudo-time derivative of pressure to the continuity equation as

$$\frac{\partial p}{\partial \tau} = -\beta \nabla \cdot u . \tag{2.13}$$

The time derivation term in Eq. (2.5) is differenced using a backward second-order three–point implicit formula and moved to the right-hand side of the equation:

$$0 = -\frac{1.5u_i^{n+1} - 2u_i^n + 0.5u_i^{n-1}}{\Delta t} - \hat{r}^{n+1} , \tag{2.14}$$

where Δt is the physical time step and the superscript n denotes the time level. To get the solution of Eq. (2.14) which satisfies Eq. (2.3) at the physical time level $n+1$, the iterations will be performed until u_i^{n+1} is divergence free. The velocity field and pressure field will be modified during the iteration procedure to satisfy both Eqs. (2.3) and (2.14). But, as the time-derivative term is absent from Eq. (2.3), it is not possible to update the pressure field. To relate the pressure field with the velocity field, the following pseudo-compressibility relation is introduced:

$$\frac{\partial \hat{p}^{n+1}}{\partial \tau} = -\beta \left[\frac{\partial}{\partial x} u + \frac{\partial}{\partial y} v + \frac{\partial}{\partial z} w \right]^{n+1}. \tag{2.15}$$

Iteration will be performed on Eq. (2.15) as a pseudo-time increases. Also a pseudo-time derivative of velocity is added to the left-hand side of Eq. (2.14):

$$\frac{\partial u_i^{n+1}}{\partial \tau} = -\frac{1.5u_i^{n+1} - 2u_i^n + 0.5u_i^{n-1}}{\Delta t} - \hat{r}^{n+1}. \tag{2.16}$$

Then, Eqs. (2.15) and (2.16) can be combined into one equation and it is written in a vector form as follows:

$$\frac{\partial Q^{n+1}}{\partial \tau} = -R^{n+1} - S^{n+1}, \tag{2.17}$$

where

$$R^{n+1} = \left(\frac{\partial}{\partial x}\left(E^{n+1} - E_v^{n+1}\right) + \frac{\partial}{\partial y}\left(F^{n+1} - F_v^{n+1}\right) + \frac{\partial}{\partial z}\left(G^{n+1} - G_v^{n+1}\right) \right),$$

$$S^{n+1} = \frac{I_m}{\Delta t}\left(1.5Q^{n+1} - 2Q^n + 0.5Q^{n-1}\right),$$

$$I_m = diag[0,1,1,1],$$

$$Q = \begin{bmatrix} p \\ u \\ v \\ w \end{bmatrix}, \quad E = \begin{bmatrix} \beta u \\ u^2 + p \\ uv \\ uw \end{bmatrix}, \quad F = \begin{bmatrix} \beta v \\ vu \\ v^2 + p \\ vw \end{bmatrix}, \quad G = \begin{bmatrix} \beta w \\ wu \\ wv \\ w^2 + p \end{bmatrix}$$

$$E_v = \frac{1}{\mathrm{Re}}\begin{bmatrix} 0 \\ \hat{\tau}_{xx} \\ \hat{\tau}_{xy} \\ \hat{\tau}_{xz} \end{bmatrix}, \quad F_v = \frac{1}{\mathrm{Re}}\begin{bmatrix} 0 \\ \hat{\tau}_{yx} \\ \hat{\tau}_{yy} \\ \hat{\tau}_{yz} \end{bmatrix}, \quad G_v = \frac{1}{\mathrm{Re}}\begin{bmatrix} 0 \\ \hat{\tau}_{zx} \\ \hat{\tau}_{zy} \\ \hat{\tau}_{zz} \end{bmatrix}$$

As additional time scale is introduced to make use of the pseudo-compressibility method for unsteady problems, this procedure is called the method of dual-time stepping. At each physical time level $n+1$, Eq. (2.17) will be solved as pseudo-time goes on until convergence is obtained.

The flux Jacobian matrices have three different eigenvalues as will be shown in next part. For higher Reynolds number, the flow is predominated by convection. Equation (2.17) is hyperbolic in space and pseudo-time in the limit of $\mathrm{Re} \to \infty$. The physical-time step term behaves like a source term to the hyperbolic equation. Thus, the upwind differencing methods developed for the hyperbolic system of equations of the compressible flow problems can be used to discretize the inviscid flux terms.

For the steady-state calculation, Δt is set to infinity and the quantities at physical time levels n-1 and n can be set to the freestream condition. If the steady-state solution at physical time level $n+1$ is different from the freestream condition, which is the condition for all calculations, the source-like term in Eq. (2.17) will vanish. Then Eq. (2.17) is simplified for the steady-state calculation by dropping the superscript $n+1$ as:

$$\frac{\partial \hat{Q}}{\partial \tau} = -\hat{R}, \tag{2.18}$$

The governing equation for the steady-state calculation is very easily derived from the time-accurate formulation by dropping the source-like term, and the resulting equation is exactly the same with the equation derived for the steady-state calculation only by others. The steady-state solution is calculated with the unsteady solver by neglecting one term and proceeding in one physical time step with the time step Δt of infinity.

2.3 Spatial Discretization

Then, the three-dimensional incompressible Navier-Stokes equations are implemented on the flow solver by the non-dimensionalization and coordinate transformation. Flow variables are non-dimensionalized as follows:

$$u_i^* = \frac{u_i}{u_\infty}, \quad x_i^* = \frac{x_i}{L}, \quad p_i^* = \frac{\hat{p}}{\rho_\infty u_\infty^2}, \quad t^* = \frac{t u_\infty}{L}, \quad \mathrm{Re} = \frac{\rho_\infty u_\infty L}{\mu_\infty} \tag{2.19}$$

With the non-dimensionalization and coordinate transformation, the governing equation can be expressed in a general curvilinear coordinates of (ξ, η, ζ) as follows:

$$\frac{1}{J}\frac{\partial Q}{\partial \tau} = -\left[\frac{\partial}{\partial \xi}\left(\hat{E} - \hat{E}_v\right) + \frac{\partial}{\partial \eta}\left(\hat{F} - \hat{F}_v\right) + \frac{\partial}{\partial \zeta}\left(\hat{G} - \hat{G}_v\right)\right] - \hat{S} \tag{2.20}$$

where

$$\hat{E}=\frac{1}{J}\left(\xi_x E+\xi_y F+\xi_z G\right)=\frac{1}{J}\begin{bmatrix}\beta U\\ uU+\xi_x p\\ vU+\xi_y p\\ wU+\xi_z p\end{bmatrix},$$

$$\hat{F}=\frac{1}{J}\left(\eta_x E+\eta_y F+\eta_z G\right)=\frac{1}{J}\begin{bmatrix}\beta V\\ uV+\eta_x p\\ vV+\eta_y p\\ wV+\eta_z p\end{bmatrix},$$

$$\hat{G}=\frac{1}{J}\left(\zeta_x E+\zeta_y F+\zeta_z G\right)=\frac{1}{J}\begin{bmatrix}\beta W\\ uW+\zeta_x p\\ vW+\zeta_y p\\ wW+\zeta_z p\end{bmatrix},$$

$$\hat{E}_v=\frac{1}{J}\left(\xi_x E_v+\xi_y F_v+\xi_z G_v\right)=\frac{1}{J}\frac{1}{\mathrm{Re}}\begin{bmatrix}0\\ \xi_x\hat{\tau}_{xx}+\xi_y\hat{\tau}_{xy}+\xi_z\hat{\tau}_{xz}\\ \xi_x\hat{\tau}_{yx}+\xi_y\hat{\tau}_{yy}+\xi_z\hat{\tau}_{yz}\\ \xi_x\hat{\tau}_{zx}+\xi_y\hat{\tau}_{zy}+\xi_z\hat{\tau}_{zz}\end{bmatrix},$$

$$\hat{F}_v=\frac{1}{J}\left(\eta_x E_v+\eta_y F_v+\eta_z G_v\right)=\frac{1}{J}\frac{1}{\mathrm{Re}}\begin{bmatrix}0\\ \eta_x\hat{\tau}_{xx}+\eta_y\hat{\tau}_{xy}+\eta_z\hat{\tau}_{xz}\\ \eta_x\hat{\tau}_{yx}+\eta_y\hat{\tau}_{yy}+\eta_z\hat{\tau}_{yz}\\ \eta_x\hat{\tau}_{zx}+\eta_y\hat{\tau}_{zy}+\eta_z\hat{\tau}_{zz}\end{bmatrix},$$

$$\hat{G}_v=\frac{1}{J}\left(\zeta_x E_v+\zeta_y F_v+\zeta_z G_v\right)=\frac{1}{J}\frac{1}{\mathrm{Re}}\begin{bmatrix}0\\ \zeta_x\hat{\tau}_{xx}+\zeta_y\hat{\tau}_{xy}+\zeta_z\hat{\tau}_{xz}\\ \zeta_x\hat{\tau}_{yx}+\zeta_y\hat{\tau}_{yy}+\zeta_z\hat{\tau}_{yz}\\ \zeta_x\hat{\tau}_{zx}+\zeta_y\hat{\tau}_{zy}+\zeta_z\hat{\tau}_{zz}\end{bmatrix}$$

$$\hat{S} = \frac{1}{J}\frac{1}{\Delta t}\begin{bmatrix} 0 \\ 1.5u^{n+1} - 2u^{n} + 0.5u^{n-1} \\ 1.5v^{n+1} - 2v^{n} + 0.5v^{n-1} \\ 1.5w^{n+1} - 2w^{n} + 0.5w^{n-1} \end{bmatrix}$$

$$U = \xi_x u + \xi_y v + \xi_z w,\ V = \eta_x u + \eta_y v + \eta_z w,\ W = \zeta_x u + \zeta_y v + \zeta_z w$$

2.3.1 Differencing of Inviscid Flux Terms

The inviscid flux terms in the ξ, η, and ζ directions in Eq. (2.20) are discretized using a finite difference method as follows:

$$\left(\frac{\partial E}{\partial \xi} + \frac{\partial F}{\partial \eta} + \frac{\partial G}{\partial \zeta}\right)_{i,j,k} = \tilde{E}_{i+\frac{1}{2},j,k} - \tilde{E}_{i-\frac{1}{2},j,k} + \tilde{F}_{i,j+\frac{1}{2},k} - \tilde{F}_{i,j-\frac{1}{2},k} + \tilde{G}_{i,j,+\frac{1}{2}} - \tilde{G}_{i,j,k-\frac{1}{2}}, \qquad (2.21)$$

where $\tilde{E}$, $\tilde{F}$, and $\tilde{G}$ are the modified fluxes, and *i*, *j*, and *k* are spatial indices. The finite difference method is very similar to a semi-discrete finite volume method which is based on the local flux balance of each cell. But in a finite difference method, the metrics of the transformation and the dependent variables are defined at mesh points instead of at cell face.

As the discretized equation, Eq. (2.21), is in a central differencing form which is non-dissipative by itself, the modified fluxes should include numerical dissipation models which are explicitly added to the physical flux terms:

$$\begin{aligned} \tilde{E}_{i+\frac{1}{2},j,k} &= \frac{1}{2}\left(\hat{E}_{i+1,j,k} + \hat{E}_{i,j,k}\right) - \hat{D}_{i+\frac{1}{2},j,k}, \\ \tilde{F}_{i,j+\frac{1}{2},k} &= \frac{1}{2}\left(\hat{F}_{i,j+1,k} + \hat{F}_{i,j,k}\right) - \hat{D}_{i,j+\frac{1}{2},k}, \end{aligned} \qquad (2.22)$$

$$\tilde{G}_{i,j,k+\frac{1}{2}} = \frac{1}{2}\left(\tilde{G}_{i,j,k+1} + \tilde{G}_{i,j,k}\right) - \hat{D}_{i,j,k+\frac{1}{2}}.$$

The dissipation models are often called filters, since they work like low pass filters which damp out high frequency modes and suppress the tendency for odd and even point decoupling.

Spatial differencing can be either central or upwind differencing, depending on the numerical dissipation model in Eq. (2.22). The dissipation coefficient for a system of equations must be a matrix to meet the requirement of upwinding, and a scalar coefficient can be used for central differencing. The order of accuracy of the dissipation model will approach first order if discontinuities are present. However, since there is no discontinuity for incompressible flows, such as shock waves, the accuracy should be higher than first order.

2.3.2 Upwind Differencing Method

Upwind differencing simulates the wave propagation properties of hyperbolic equations and automatically suppresses unnecessary oscillations. For incompressible flows, the inviscid fluxes are not homogeneous of degree one in the state vector *Q*, that is, the following relations do not hold as for compressible flows:

$$\hat{E} = \hat{A}Q, \quad \hat{F} = \hat{B}Q, \quad \hat{G} = \hat{C}Q \tag{2.23}$$

Hence, the usual flux vector splitting methods does not work here. Therefore, the inviscid fluxes are upwind-differenced using a flux-difference splitting based on Osher's upwind differencing scheme [34].

First-order accuracy in space can be obtained by defining the numerical dissipation model in equation (2.22) as

$$\hat{D}_{i+1/2} = \frac{1}{2}\left(\Delta\hat{E}^{+}_{i+1/2} - \Delta\hat{E}^{-}_{i+1/2}\right), \tag{2.24}$$

where $\Delta\hat{E}^{\pm}$ is the flux across positive or negative traveling waves and the subscript *j* and *k* are dropped for simplicity. The same method can be applied to the η and ζ direction terms. The flux difference is taken as

$$\Delta\hat{E}^{\pm}_{i+1/2} = \hat{A}^{\pm}\left(\overline{Q}\right)\Delta Q_{i+1/2}, \tag{2.25}$$

where the flux difference is evaluated at the midpoint by using the arithmetic average of *Q*:

$$\overline{Q} = \frac{Q_{i+1} - Q_i}{2}, \tag{2.26}$$

and the ΔQ term is given by

$$\Delta Q_{i+1/2} = Q_{i+1} - Q_i \tag{2.27}$$

For three-dimensional problems, a similarity transformation for the Jacobian matrix given in Eq. (2.25) is introduced as

$$\hat{A}_i = X_i \Lambda_i X_i^{-1} \tag{2.28}$$

Where

$$\Lambda = diag\left[\lambda_1, \lambda_2, \lambda_3, \lambda_4\right]$$

$$\lambda_{1,2} = \theta + k_t \tag{2.29}$$

$$\lambda_{3,4} = \theta + \frac{1}{2} k_t \pm c$$

and c is the scaled artificial speed of sound given by

$$c = \sqrt{\left(\theta + \frac{1}{2} k_t\right)^2 + \beta\left(k_x^2 + k_y^2 + k_z^2\right)},$$

$$\theta = k_x u + k_y v + k_z w, \tag{2.30}$$

$$k_x = \frac{1}{J}\frac{\partial \xi_i}{\partial x} \;,\; k_y = \frac{1}{J}\frac{\partial \xi_i}{\partial y},\; k_z = \frac{1}{J}\frac{\partial \xi_i}{\partial z},\; k_t = \frac{1}{J}\frac{\partial \xi_i}{\partial t} \;,$$

$$\xi_i = \xi, \eta, \zeta \text{ for } i = 1, 2, 3.$$

It should be noted that the subscript i here represents the coordinate direction. The matrix of the right eigenvectors is given by

$$X_i = \begin{bmatrix} 0 & 0 & \beta(c-k_t/2) & -\beta(c+k_t/2) \\ x_k & x_{kk} & u\lambda_3+\beta k_x & u\lambda_4+\beta k_x \\ y_k & y_{kk} & v\lambda_3+\beta k_y & u\lambda_4+\beta k_y \\ z_k & z_{kk} & w\lambda_3+\beta k_z & u\lambda_4+\beta k_z \end{bmatrix} \quad 0$$

$$x_k = \frac{\partial x}{\partial \xi_{i+1}}, \quad x_{kk} = \frac{\partial x}{\partial \xi_{i+2}} \tag{2.31}$$

$$\xi_{i+1} = \eta, \zeta, \xi \quad \text{for} \quad i = 1,2,3,$$

$$\xi_{i+2} = \zeta, \xi, \eta \quad \text{for} \quad i = 1,2,3,$$

and its inverse is given by

$$X_i^{-1} = \frac{1}{c^2 - k_t^2/4}$$

$$\begin{bmatrix} x_{kk}(k_z v - k_y w) + y_{kk}(k_x w - k_z u) + z_{kk}(k_y u - k_x v) \\ x_k(k_y w - k_z v) + y_k(k_z u - k_x w) + z_k(k_x v - k_y u) \\ -\lambda_4(c+k_t/2)/(2\beta c) \\ -\lambda_3(c-k_t/2)/(2\beta c) \end{bmatrix}$$

$$\begin{matrix} y_{kk}(\lambda_1 w + \beta k_z) - z_{kk}(\lambda_1 v + \beta k_y) \\ -y_k(\lambda_1 w + \beta k_z) + z_k(\lambda_1 v + \beta k_y) \\ k_x(c+k_t/2)/(2c) \\ k_x(c-k_t/2)/(2c) \end{matrix} \tag{2.32}$$

$$\begin{matrix} z_{kk}(\lambda_1 u + \beta k_x) - x_{kk}(\lambda_1 w + \beta k_z) \\ -z_k(\lambda_1 u + \beta k_x) + x_k(\lambda_1 w + \beta k_z) \\ k_y(c+k_t/2)/(2c) \\ k_y(c-k_t/2)/(2c) \end{matrix}$$

$$\begin{matrix} x_{kk}(\lambda_1 v + \beta k_y) - y_{kk}(\lambda_1 u + \beta k_x) \\ -x_k(\lambda_1 v + \beta k_y) + y_k(\lambda_1 u + \beta k_x) \\ k_z(c+k_t/2)/(2c) \\ k_z(c-k_t/2)/(2c) \end{matrix}$$

The diagonal matrix Λ_i can be split into positive and negative running characteristics which have only positive and negative diagonal entries, respectively.

$$\begin{aligned} |\Lambda_i| &= diag\left[|\lambda_1|,|\lambda_2|,|\lambda_3|,|\lambda_4|\right] \\ \Lambda_i &= \Lambda_i^+ + \Lambda_i^- \\ \Lambda_i^+ &= \frac{\Lambda_i + |\Lambda_i|}{2} \\ \Lambda_i^- &= \frac{\Lambda_i - |\Lambda_i|}{2} \end{aligned} \tag{2.33}$$

The A^+ and A^- matrices are computed by decomposing the diagonal matrix in Eq. (2.28) using the relations in Eq. (2.33):

$$\hat{A}_i = X_i\left(\Lambda_i^+ + \Lambda_i^-\right)X_i^{-1} = X_i\Lambda_i^+X_i^{-1} + X_i\Lambda_i^-X_i^{-1} \tag{2.34}$$

Thus we get

$$\begin{aligned} \hat{A}_i^+ &= X_i\Lambda_i^+X_i^{-1} \\ \hat{A}_i^- &= X_i\Lambda_i^-X_i^{-1} \end{aligned} \tag{2.35}$$

If we define an absolute Jacobian matrix as

$$\left|\hat{A}_i\right| = X_i|\Lambda_i|X_i^{-1} \tag{2.36}$$

then we get

$$\left|\hat{A}_i\right| = \hat{A}_i^+ - \hat{A}_i^- \tag{2.37}$$

with Eq. (2.37), Eq. (2.24) can now be rewritten as

$$\hat{D}_{i+1/2} = \frac{1}{2}\left|\hat{A}_{i+1/2}\right|\left(Q_{i+1} - Q_i\right) \tag{2.38}$$

2.3.3 Higher order spatial accuracy

In order to obtain higher order spatial accuracy, a Monotone Upstream-centered Schemes for Conservation Laws (MUSCL [35]) interpolation is adopted as:

$$\begin{aligned} q_{i+1/2}^- &= q_i + \frac{1}{4}\left[(1-\kappa)(q_i - q_{i-1}) + (1+\kappa)(q_{i+1} - q_i)\right] \\ q_{i+1/2}^+ &= q_i - \frac{1}{4}\left[(1+\kappa)(q_{i+1} - q_i) + (1-\kappa)(q_{i+2} - q_{i+1})\right] \end{aligned} \tag{2.39}$$

where q denotes the primitive variables. For constant k=1/3, the order of spatial accuracy is third, and the second order accuracy for k=-1, 0, 1. Especially for k=1, it becomes a central-difference scheme of second order [36].

2.4 Time Integration Method

In this chapter, the implicit methods to solve the pseudo-time equation, Eq.

(2.17), is presented. A first-order Euler implicit formula is used for pseudo-time derivative to form the matrix equation. The next consideration is the formation of the Jacobian matrix of the residual vector of the flux terms required for the implicit side of the resulting equation. However, the exact Jacobian of the flux vectors is very costly to form. Instead, an approximate Jacobian of the residual vector can be used with different levels of approximation. Then, the matrix equation is solved using Lower-Upper Symmetric-Gauss-Seidel (SGS) relaxation scheme.

2.4.1 Dual Time Stepping and Pseudo-Time Discretization

For time-accurate unsteady problems, pseudo-time sub-iteration strategy is adopted to solve the unsteady, incompressible systems given by:

$$\frac{1}{J}\frac{\partial Q}{\partial t} = -\hat{R} \quad . \tag{2.40}$$

The time derivative term is differenced using a backward second-order three-point implicit formula and moved to the right-hand side of the equation:

$$0 = -\frac{1.5\mathrm{Q}^{\mathrm{n+1}} - 2Q^{n} + 0.5Q^{n-1}}{J\Delta t} - \hat{R}^{n+1} \quad . \tag{2.41}$$

where a superscript *n* denotes the physical time iteration level.

A pseudo-time derivative of *Q* is added on the left-hand side of Eq. (2.41):

$$\frac{1}{J}\frac{\partial Q^{n+1}}{\partial \tau} = -\hat{R}^{n+1} - \frac{1.5\mathrm{Q}^{\mathrm{n+1}} - 2Q^{n} + 0.5Q^{n-1}}{J\Delta t} = -\hat{R}^{n+1} - \hat{S}^{n+1} \quad . \tag{2.42}$$

Since the first-order discretization has better convergence properties than higher-order in general, the pseudo-time derivative term is discretized using the first-order Euler implicit formula [35, 37, 38]:

$$\frac{1}{J}\frac{Q^{n+1,m+1}-Q^{n+1,m}}{\Delta\tau}=-\hat{R}^{n+1,m+1}-\hat{S}^{n+1,m+1} \quad (2.43)$$

where a superscript *m* denotes the pseudo-time iteration level. The time accuracy of the solution is necessary in terms of the physical time, but not in terms of the pseudo-time. Therefore, the dual time stepping method adopted here has second-order time accuracy. Now, Eq. (2.43) can be rewritten as by using a simple Taylor series expansion:

$$\left[\frac{1}{J\Delta\tau}+\left(\frac{\partial\hat{R}}{\partial Q}+\frac{\partial\hat{S}}{\partial Q}\right)^{n+1,m}\right]\Delta Q^{n+1,m}=-\hat{R}^{n+1,m}-\hat{S}^{n+1,m} \quad (2.44)$$

For steady-state calculations, the source-like term *S* dropped from the equation because Δt is set to infinity. Then Eq. (2.44) is simplified for the steady-state calculation as:

$$\frac{1}{J\Delta\tau}+\left[\frac{\partial\hat{R}}{\partial Q}\right]^{m}\Delta Q^{m}=-\hat{R}^{m}. \quad (2.45)$$

The system of governing equations, Eq. (2.43), can be rewritten as:

$$\frac{1}{J}\frac{\partial Q^{m+1}}{\partial \tau}+\left[\frac{\partial}{\partial \xi}\left(\hat{E}-\hat{E}_v\right)+\frac{\partial}{\partial \eta}\left(\hat{F}-\hat{F}_v\right)+\frac{\partial}{\partial \zeta}\left(\hat{G}-\hat{G}_v\right)\right]^{m+1}+\hat{S}^{m+1}=0 \tag{2.46}$$

where the superscript n+1 is dropped for simplicity.

Consider a Taylor series expansion about pseudo-time level m as follows:

$$\hat{E}^{m+1}=\hat{E}^{m}+\left[\frac{\partial \hat{E}}{\partial Q}\right]^{m}\Delta Q^{m}+O(\Delta\tau^{2})\cong\hat{E}^{m}+\hat{A}\Delta Q^{m} \tag{2.47}$$

In a similar fashion the other flux vectors can be linearized as:

$$\begin{aligned}\hat{F}^{m+1}&\cong\hat{F}^{m}+\hat{B}\Delta Q^{m}\\ \hat{G}^{m+1}&\cong\hat{G}^{m}+\hat{C}\Delta Q^{m}\end{aligned} \tag{2.48}$$

The viscous flux Jacobian in the implicit part is neglected since it does not influence the solution's accuracy. Thus, the viscous flux vectors are approximated as follows:

$$\begin{aligned}\hat{E}_v^{m+1}&\cong\hat{E}_v^{m}\\ \hat{F}_v^{m+1}&\cong\hat{F}_v^{m}\\ \hat{G}_v^{m+1}&\cong\hat{G}_v^{m}\end{aligned} \tag{2.49}$$

Substituting the above linearizations in Eq. (2.46) to obtain

$$\frac{1}{J}\frac{\Delta Q^m}{\Delta \tau}+\left[\frac{\partial}{\partial \xi}\left(\hat{E}^m+\hat{A}\Delta Q^m\right)+\frac{\partial}{\partial \eta}\left(\hat{F}^m+\hat{B}\Delta Q^m\right)+\frac{\partial}{\partial \zeta}\left(\hat{G}^m+\hat{C}\Delta Q^m\right)\right] \\ -\left(\frac{\partial \hat{E}_v^m}{\partial \xi}+\frac{\partial \hat{F}_v^m}{\partial \eta}+\frac{\partial \hat{G}_v^m}{\partial \zeta}\right)+\hat{S}^{m+1}=0 \tag{2.50}$$

where

$$\Delta Q^m = Q^{m+1}-Q^m$$

$$\hat{S}^{m+1} \cong \hat{S}^m+\left[\frac{\partial \hat{S}}{\partial Q}\right]^m \Delta Q^m$$

Rewriting the Eq. (2.50)

$$\frac{I}{J}\frac{\Delta Q^m}{\Delta \tau}+\frac{\partial}{\partial \xi}\left(\hat{A}\Delta Q^m\right)+\frac{\partial}{\partial \eta}\left(\hat{B}\Delta Q^m\right)+\frac{\partial}{\partial \zeta}\left(\hat{C}\Delta Q^m\right)+\left[\frac{\partial \hat{S}}{\partial Q}\right]^m \Delta Q^m \\ =-\left(\frac{\partial}{\partial \xi}\left(\hat{E}-\hat{E}_v\right)+\frac{\partial}{\partial \eta}\left(\hat{F}-\hat{F}_v\right)+\frac{\partial}{\partial \zeta}\left(\hat{G}-\hat{G}_v\right)\right)^m-\hat{S}^m \tag{2.51}$$

and is factored as

$$\left(\frac{I}{J\Delta\tau}+\frac{\partial\hat{S}}{\partial Q}+\frac{\partial\hat{A}}{\partial\xi}+\frac{\partial\hat{B}}{\partial\eta}+\frac{\partial\hat{C}}{\partial\zeta}\right)\Delta Q^m$$
$$=-\left(\frac{\partial}{\partial\xi}\left(\hat{E}-\hat{E}_v\right)+\frac{\partial}{\partial\eta}\left(\hat{F}-\hat{F}_v\right)+\frac{\partial}{\partial\zeta}\left(\hat{G}-\hat{G}_v\right)\right)^m-\hat{S}^m=-\hat{R}^m \tag{2.52}$$

where I is the identity matrix and R stands for the residual vector including viscous terms. The flux Jacobian matrices are split according to the signs of the eigenvalues of the flux Jacobian matrices as:

$$\left(\frac{I_{tr}}{J}+\delta_\xi^+\hat{A}^+ +\delta_\xi^-\hat{A}^- +\delta_\eta^+\hat{B}^+ +\delta_\eta^-\hat{B}^- +\delta_\zeta^+\hat{C}^+ +\delta_\zeta^-\hat{C}^-\right)\Delta Q^m=-\hat{R}^m \tag{2.53}$$

where

$$I_{tr}=\frac{I}{\Delta\tau}+\frac{\partial S}{\partial Q}.$$

and δ denotes a finite difference operator in each direction.

2.4.2 LU-SGS Scheme

Yoon et al. [39] introduced an implicit algorithm based on a Lower-Upper factorization and Gauss-Seidel relaxation. Rewriting Eq. (2.53) in detail yields

$$\left[\frac{I_{tr}}{J}+\hat{A}_i^+-\hat{A}_{i-1}^+ +\hat{A}_{i+1}^- -\hat{A}_i^- +\hat{B}_j^+ -\hat{B}_{j-1}^+ +\hat{B}_{j+1}^- -\hat{B}_j^-\right.$$
$$\left.+\hat{C}_k^+ -\hat{C}_{k-1}^+ +\hat{C}_{k+1}^- -\hat{C}_k^-\right]\Delta Q^m=-\hat{R}_{i,j,k}^m \tag{2.54}$$

and Eq. (2.54) can be rewritten in a compact form as:

$$\left[\left(\frac{I_{tr}}{J}+\rho(\hat{A})+\rho(\hat{B})+\rho(\hat{C})\right)I-\hat{A}_{i-1}^{+}+\hat{A}_{i+1}^{-}-\hat{B}_{j-1}^{+}+\hat{B}_{j+1}^{-}-\hat{C}_{k-1}^{+}+\hat{C}_{k+1}^{-}\right]\Delta Q^{m} = -\hat{R}_{i,j,k}^{m} \tag{2.55}$$

and the flux Jacobian matrices are split approximately to yield diagonal dominance as

$$\begin{aligned}&\hat{A}^{\pm}=\frac{1}{2}\left(\hat{A}\pm\rho(\hat{A})\right),\hat{B}^{\pm}=\frac{1}{2}\left(\hat{B}\pm\rho(\hat{B})\right),\hat{C}^{\pm}=\frac{1}{2}\left(\hat{C}\pm\rho(\hat{C})\right)\\&\rho(\hat{A})=\hat{A}_{i}^{+}-\hat{A}_{i}^{-},\rho(\hat{B})=\hat{B}_{i}^{+}-\hat{B}_{i}^{-},\rho(\hat{C})=\hat{C}_{i}^{+}-\hat{C}_{i}^{-}\end{aligned} \tag{2.56}$$

where $\rho(A)=\kappa\left|\lambda(A)\right|$ and κ denotes a constant that is between 1.01 and 1.5. In the present work, κ is given 1.1 for incompressible problems. Rewriting Eq. (2.55) yields

$$\begin{aligned}&r_{i,j,k}I\Delta Q^{m}-\hat{A}_{i-1}^{+}\Delta Q^{m}+\hat{A}_{i+1}^{-}\Delta Q^{m}-\hat{B}_{j-1}^{+}\Delta Q^{m}+\hat{B}_{j+1}^{-}\Delta Q^{m}\\&-\hat{C}_{k-1}^{+}\Delta Q^{m}+\hat{C}_{k+1}^{-}\Delta Q^{m}=-\hat{R}_{i,j,k}^{m}\end{aligned} \tag{2.57}$$

where

$$r_{i,j,k}=\frac{1}{J\Delta\tau}+\rho(\hat{A})+\rho(\hat{B})+\rho(\hat{C}) \tag{2.58}$$

The above factored equation is solved as a series of following lower and upper sweeps.

Lower Sweep:

$$\begin{aligned} r_{i,j,k} I \Delta Q^{*}_{i,j,k} &= -\hat{R}^{m}_{i,j,k} + \hat{A}^{+}_{i-1,j,k}\Delta\hat{Q}^{*}_{i-1,j,k} + \hat{B}^{+}_{i,j-1,k}\Delta\hat{Q}^{*}_{i,j-1,k} + \hat{C}^{+}_{i,j,k-1}\Delta\hat{Q}^{*}_{i,j,k-1} \\ &\quad - \hat{A}^{-}_{i+1,j,k}\Delta\hat{Q}^{*}_{i+1,j,k} - \hat{B}^{-}_{i,j+1,k}\Delta\hat{Q}^{*}_{i,j+1,k} - \hat{C}^{-}_{i,j,k+1}\Delta\hat{Q}^{*}_{i,j,k+1} \\ &\approx -\hat{R}^{m}_{i,j,k} + \hat{A}^{+}_{i-1,j,k}\Delta\hat{Q}^{*}_{i-1,j,k} + \hat{B}^{+}_{i,j-1,k}\Delta\hat{Q}^{*}_{i,j-1,k} + \hat{C}^{+}_{i,j,k-1}\Delta\hat{Q}^{*}_{i,j,k-1} \\ &= DCV_{i,j,k} \end{aligned} \tag{2.59}$$

Upper Sweep:

$$\begin{aligned} r_{i,j,k} I \Delta\hat{Q}^{m}_{i,j,k} &= -\hat{R}^{m}_{i,j,k} + \hat{A}^{+}_{i-1,j,k}\Delta\hat{Q}^{m}_{i-1,j,k} + \hat{B}^{+}_{i,j-1,k}\Delta\hat{Q}^{m}_{i,j-1,k} + \hat{C}^{+}_{i,j,k-1}\Delta\hat{Q}^{m}_{i,j,k-1} \\ &\quad - \hat{A}^{-}_{i+1,j,k}\Delta\hat{Q}^{m}_{i+1,j,k} - \hat{B}^{-}_{i,j+1,k}\Delta\hat{Q}^{m}_{i,j+1,k} - \hat{C}^{-}_{i,j,k+1}\Delta\hat{Q}^{m}_{i,j,k+1} \\ &\approx -\hat{R}^{m}_{i,j,k} + \hat{A}^{+}_{i-1,j,k}\Delta\hat{Q}^{*}_{i-1,j,k} + \hat{B}^{+}_{i,j-1,k}\Delta\hat{Q}^{*}_{i,j-1,k} + \hat{C}^{+}_{i,j,k-1}\Delta\hat{Q}^{*}_{i,j,k-1} \\ &\quad - \hat{A}^{-}_{i+1,j,k}\Delta\hat{Q}^{m}_{i+1,j,k} - \hat{B}^{-}_{i,j+1,k}\Delta\hat{Q}^{m}_{i,j+1,k} - \hat{C}^{-}_{i,j,k+1}\Delta\hat{Q}^{m}_{i,j,k+1} \\ &= DCV_{i,j,k} - \hat{A}^{-}_{i+1,j,k}\Delta\hat{Q}^{m}_{i+1,j,k} - \hat{B}^{-}_{i,j+1,k}\Delta\hat{Q}^{m}_{i,j+1,k} - \hat{C}^{-}_{i,j,k+1}\Delta\hat{Q}^{m}_{i,j,k+1} \end{aligned} \tag{2.60}$$

Consequently, the LU-SGS scheme can be written in the following form:

$$LD^{-1}U\Delta Q^{m} = -R^{m} \tag{2.61}$$

2.5 FSI Coupling Methodology

In FSI simulations, there are two kinds of strategies to couple fluid and solid modules: the tightly coupled method and the loosely coupled method [40, 41]. In the first method, the fluid and solid modules are simultaneously marched by coupled systems of equations, while in the second method, the fluid and solid modules are independently marched before they exchange the data necessary for boundary conditions. The drawbacks of the tightly coupled method are the ill-conditioned nature of the coupled system matrices, and the rewriting of the fluid and solid modules, which seriously limits the applicability of the method. Consequently, the loosely coupled method has been adopted in the present work.

2.5.1 Data Transfer on Fluid-Solid Boundary

The fluid and solid modules are solved by the loosely coupling method with different mesh densities. Along non-matching fluid-solid interface, an interpolation technique is thus necessary to properly transfer the pressure and displacement into solid and fluid module, respectively.

A method based on a common-refinement is implemented as a data transfer technique between non-matching meshes [42]. This method utilizes so called a common refinement, which is composed of the intersection of the fluid and solid sub-elements along the common interface. Firstly, the fluid interface nodes are projected onto the solid interface, where the normal vector at each fluid node is obtained by averaging the neighboring element normal vectors. Then, the union of the original solid interface nodes and the projected nodes from the fluid interface are combined to create sub-elements on the solid interface. A similar inverse projection of the solid interface nodes onto the fluid interface is carried out to create the sub-elements on the

fluid interface. The final sub-elements (or the common refinement mesh) are then obtained from a convex combination of fluid and solid sub-elements. Along the common refinement, an integration of physical variables is carried out. For example, the load vector, R_s^j, over the common refinement nodes can be computed as follows.

$$R_s^j = \sum_{i=1}^{e_c} \int_{\sigma_c^i} N_s^j \tilde{t}_f \, d\Gamma \,. \tag{2.62}$$

In Eq. (2.62), R_s^j denotes the concentrated force vector at node j on the solid interface, N_s^j is the shape function associated with the node j, and e_c indicates the number of sub-elements sharing the node j. σ_c^i denotes the i^{th} sub-element sharing the node j, $\tilde{t}_f$ is the force at fluid interface nodes, and Γ is the common interface boundary. A similar integration can be carried out to obtain displacement.

This method can accurately minimize the L_2 interpolation error, and it is conservative without producing numerical oscillations. Overall discretization error is $O(h_f^2 + h_s^2)$, where h_f and h_s are the resolutions of the fluid and solid meshes, respectively. Further details can be found in Ref. [42].

2.5.2 Dynamic Grid Deformation Technique

Due to geometric deformation occurring at each time-step, a dynamic grid deformation technique must be employed. A simple, efficient, and non-iterative grid deformation technique based on the creation of a Delaunay graph of the original mesh is adopted in this work [43]. In order to create the triangular Delaunay graph, all of the geometric boundary points are connected to some reference points on the outer boundary (or outside) of computational domain. The area coefficients are then

computed and stored as follows to locate the mesh points in the Delaunay graph after grid movement.

$$e_i = \frac{S_i}{S}, \quad 1 \le i \le 3,. \tag{2.63}$$

where S is the area of the Delaunay graph, and S_i is the area of sub-triangles defined by the grid point *i* within the Delaunay graph. After moving the geometric boundary points according to a prescribed motion or structural deformation, a new set of coordinates is generated for the nodal points of the Delaunay graph. The mesh points within the Delaunay graph are then relocated such that the area coefficients of each mesh point are conserved after grid movement.

$$x_P^{'} = \sum_{i=1}^{3} e_i x_i^{'}, \quad y_P^{'} = \sum_{i=1}^{3} e_i y_i^{'}.. \tag{2.64}$$

Here $(x_P^{'}, y_P^{'})$ or $(x_i^{'}, y_i^{'})$ are the new coordinates of the mesh point and the nodal points of the Delaunay graph. Further details can be found in Ref. [32]. Figure 2.1 shows an example of the dynamic grid deformation for a flapping airfoil and histories of the cell aspect ratio distribution. It is seen that the cell aspect ratio of the original mesh is almost maintained, and the mesh quality is preserved during the dynamic grid deformation process.

2.6 Grid Motion

In order to simulate insects' flapping wing motion, the moving grid technique is adapted to incompressible Navier-Stokes solver. The grid velocity would be written by following equations.

$$x_t = \frac{x^{n+1} - x^n}{\Delta t}, \quad y_t = \frac{y^{n+1} - y^n}{\Delta t}, z_t = \frac{z^{n+1} - z^n}{\Delta t}, \tag{2.65}$$

where superscript $n+1$ denotes next time step grid position and grid velocity transform to general curvilinear coordinates of (ξ, η, ζ). A dynamic grid system is under assumption of rigid body motion since the inner grid points of computational domain do not experience a relative motion.

2.7 Kinematic Modeling

2.7.1 Insect's Tethered Flight

It is often quite difficult to accurately quantify the wing motion of a free flying insect because of its small size and high wing beat frequency [44]. For example, an average insect size, such as the common fruit fly, is approximately 2~3mm in length, and it flaps its wings at a rate of 200 *Hz*. Just a mere quantification of motion for such a small and fast moving wing continues to pose significant challenge to current measuring technology.

Thus, instead of free flight wing motion, some researcher simply modelled the wing motion using a sinusoidal function [45], but modelling is insufficient to capture the key features of realistic wing motion. If it is extremely challenging to obtain the

real trajectory of free flight wing motion, tethered flight experiment may be the best alternative to study insect aerodynamics because it is the closest to the real flight. In addition, the purpose of the present numerical simulation is to understand the flow physics of more realistic flapping flight to apply its consequences in the design and analyses of small-sized flapping aerial vehicles.

2.7.2 Kinematic Modeling of Blowfly's Tethered Wing Motion

Several researchers have measured wing trajectories using wind tunnel and high-speed camera system. Nachtigall [46] suspended a blowfly in front of an open wind tunnel, and adjusted wind speed until the net horizontal force acting on the blowfly is zero to realize a forward flight condition.

From a two-dimensional side-view, the wing-tip trajectory of many insects resembles the figure, "eight", as shown in Fig. 2.2. The so-called figure-of-eight motion was first observed in 1869 by the French physiologist, Étienne-Jules Marey [47]. Nachtigall's experiment also exhibits the figure-of-eight motion of a blowfly wing whose trajectory can be expressed in terms of Fourier series.

$$F(t) = a_0 + \sum_{n=1}^{m} a_n \cos(2n\pi kt) + b_n \sin(2n\pi kt), \tag{2.66}$$

$$F(t) = [x(t), y(t), \alpha(t)]^T, \tag{2.67}$$

Here, a_0, a_n, and b_n are Fourier coefficients and k is the reduced frequency. The detailed coefficients can be found in Ref. [48]. Figure 2.2 shows the wing-tip trajectory obtained from Eq. (2.66). Free stream direction is the positive x-direction, and thus lift and thrust are the positive y- and negative x- directions. Downstroke and upstroke motion is indicated by red and green arrow, respectively. From the wing-tip

trajectory measured at equal time-interval, one can see that the interval between the wing positions is shorter during downstroke, indicating the wing motion during downstroke is relatively slow. The posture of the wing is almost horizontal, and the wing rotation is relatively mild. On the other hand, upstroke motion is fast and the leading edge is sharply pitched up. In particular, the rapid wing rotation is concentrated near the end of upstroke. In Fig. 2.2, the flapping wing motion consists of three components: translation ($y(t)$: vertical motion), lagging ($x(t)$: horizontal motion), and rotation ($\alpha(t)$).

Figure 2.3 depicts a measuring technique of three-dimensional wing kinematics. The trajectory of the wing-tip can be uniquely described by the three angles (β, γ, δ) projected onto three mutually perpendicular planes (yz, xy and zx planes). Figure 2.4 shows the trajectories of the three angles ($\beta(t)$, $\gamma(t)$, $\delta(t)$) during two and a half successive wing beats. They are measured clockwise from the positive x, z and negative y direction, respectively (see Figs. 2.3 and 2.4). The blowfly, steadily flying in front of the wind tunnel with an air speed of 2.75m/s, exhibits regular patterns of wing beat motion. In order to reproduce the blowfly's three-dimensional wing motion in computational coordinate, pitch angle ($\alpha(t)$, Ref. [46]) as well as ($\beta(t)$, $\gamma(t)$, $\delta(t)$, see Fig. 2.3) is introduced. The detailed implementation procedure can be found in Ref. [17].

2.8 Geometric Modeling and Boundary Condition

Since the vein system of a blowfly wing is complex, the precise cross-sectional shape (or airfoil shape) of the 3-D wing is complicated (see Fig. 2.5-(a)). For example, the thickness of vein is measured to be 3.63×10^{-2} mm and that of trailing membrane is 1.2×10^{-2} mm [49]. By simplifying the geometric details while maintaining the

main geometric characteristic, a tadpole type of airfoil for two-dimensional FSI simulation can be obtained, as shown in Fig. 2.5. The airfoil thickness is linearly decreased from the leading edge after the vein to the trailing edge. The material properties are as follows: the modulus of elasticity (E) of vein and membrane is 6.1×10^9 N/m^2 and 1.5×10^9 N/m^2, respectively, and the density is 1200 kg/m^3 [50]. To investigate the flexibility effects of insect wing, three types of airfoils (rigid airfoil, linear type of flexible airfoil, and homogeneous type of flexible airfoil) are considered, as shown in Fig. 2.6. The infinity value of E indicates a rigid body and thus FSI simulation is not applied. The modulus of elasticity of the linear type airfoil decreases linearly from 6.1×10^9 N/m^2 to 1.5×10^9 N/m^2 in the direction of the trailing edge, and that of the homogeneous type is the arithmetical mean of the two values. In both cases, 10% front part of airfoil is considered to be a rigid body because the stiffness in the vicinity of the leading edge is very high compared to other regions. An O-type grid of 289×113 with a wall spacing of 1×10^{-4} chord is used, and the outer boundary of the computational domain extends to 25 chords. An unstructured mesh of 244 cells is used for the solid domain.

For geometric modeling of three-dimensional wing-body shape, the picture of a blowfly's wing-body shape is scanned from Ref. [46], and realistic wing planform and sectional shape are modeled based on the scanned picture. As shown in Fig. 2.7, five types of wings are considered to examine aerodynamic effects of wing shape. The root region of a blowfly's wing is simplified, as shown in type-1 of Fig 2.7-(a). Since the wing root region exhibiting a little gap often appear in some species of fly [47] and the aerodynamic role of the gap is not clear, type-2 is considered to investigate the aerodynamic effect of the gap in a flapping flight, as in Fig. 2.7-(b). Wing sectional shape is assumed to be a thin flat plate with a 5% thickness of mean chord length ($\approx 1.9 \times 10^{-1}$ mm) in type-1 and -2. In order to analyze the effect of thickness on

aerodynamic characteristics, the average thickness of a real blowfly's wing [49] is considered as in type-3 of Fig. 2.7-(c). Here, the thickness is about 0.6% of mean chord length ($\approx 2.4\times10^{-2}$ mm). The vein system of a blowfly's wing is rather complex, because precise cross-sectional shape of a 3-D wing is corrugated and cambered by several nerves. By simplifying the geometric details while maintaining the main characteristics, type-4 can be obtained, as shown in Fig. 2.7-(d). The cross section of type-4 has some corrugation and camber with the same thickness of type-1 and -2. Finally, realistic wing planform, sectional shape, and thickness are all considered in type-5, as in Fig. 2.7-(e). A 225×97 grid for the sectional surface of type-1 is then generated (see Fig. 2.7-(a)) and a similar grid resolution is generated for type-2 to -5. Also, body shape is measured and tailored, as shown in Fig. 2.9-(a), and a 321×65 grid for half of the body surface is generated.

Generally, it is known that the body angle of attack (AOA) in blowfly's flapping flight, such as forward flight, banked turn, U-turn, reverse motion, and so on, is about 0 to 50 degrees [51]. Numerical simulations of a blowfly's 'wing-body' configuration are thus carried out for the body AOA ranging from 0 to 60 degrees, as shown in Fig. 2.8. For the blowfly's forward flight, seven cases of body AOA are investigated at 0, 15, 25, 30, 35, 45, and 60 deg., all with the same wing trajectory. Also, Fig. 2.8-(a) shows the directions of aerodynamic forces and freestream.

The overset mesh technique is then used to efficiently describe the flapping flight including three-dimensional wing-body geometry and flapping motion, as seen in Figs. 2.9-(b) to 2.9-(d). The overset grid system is composed of two blocks, and two sets of grid systems are considered: 5.58 and 8.39 million, respectively. The main grid zone including the insect body has about 3.1 million (321×65×149) or 4.83 million (353×85×161) points, and the sub grid zone containing insect wing has about 2.48 million (449×97×57) or 3.56 (465×105×73) points for type-1. Other types of

wings have a similar grid resolution. Wall spacing is 5×10^{-4} chord, and the outer boundary of the computational domain extends to 10 times the body length (30 chords), or equivalently, 12 times the wing span.

Boundary conditions for the inflow and outflow regions are based on the method of characteristics. The Jacobian matrix of the inviscid flux vector has at least one negative or one positive eigenvalues. At the inflow, there is one characteristic wave traveling out of the computational domain and two waves traveling into the domain. Thus, the velocity components are specified from freestream conditions and the pressure is extrapolated from the interior points. At the outflow, two waves are traveling out of and one is traveling into the domain. The pressure is specified and the velocity components are determined by extrapolation. It is noted that the velocity components are an approximation of the Riemann invariants corresponding to the characteristic waves [52]. In three-dimensional simulation, symmetric condition is imposed on the symmetry boundary (the plane of $y = 0$ in Fig. 2.9-(b)). The sub grid zone contains wing rotation according to the kinematic modeling data.

Since the Reynolds number of interest is relatively low ($\mathrm{Re} = O(10^2) \sim O(10^3)$), all computations have been conducted under laminar flow assumption with standard MPI parallel programming.

Chapter III
Two-dimensional Flexible Insects' Wing

3.1 Validation

3.1.1 Validation of Baseline Solver

As a validation case of the two-dimensional flow solver, a rigid NACA0012 airfoil oscillating with a constant amplitude of h_a = 0.175 is chosen. A water-tunnel experiment was performed by Heathcote and Gursul [22]. The experiments were conducted in a free-surface closed-loop water tunnel with a 381 mm wide × 508 mm deep test section to validate the force measurement system. Tests were carried out for Reynolds numbers of 10,000 and 20,000 and for a frequency range of $0 < Str < 0.72$ based on the chord length of NACA0012 airfoil. The airfoil was mounted vertically with one end attached to a horizontal shaker. A binocular strain gauge force balance was used to make direct force measurements in directions parallel and perpendicular to the freestream velocity. The forces applied to the wing in *x* and *y* directions, thrust and lift, were measured with the force balance.

The thrust coefficient is given by

$$C_t = \frac{T}{\frac{1}{2}\rho U_\infty^2 c}, \tag{3.1}$$

where T is the time-averaged thrust per unit span. The power input coefficient is given by

$$C_p = \frac{F_y v}{\frac{1}{2}\rho U_\infty^3 c}, \tag{3.2}$$

where $F_y v$ is the time-averaged instantaneous power input.

Computations are carried out for the Reynolds numbers of 10,000 and 20,000 and for the Strouhal number (Str) of $0 < Str < 0.6$.

$$\mathrm{Re} = \frac{U_\infty c}{\nu}, \ \ Str = \frac{fc}{U_\infty}, \tag{3.3}$$

Here, U_∞ is the incoming velocity, c is the chord length, ν is the kinematic viscosity, and f is the plunging frequency. The stroke of the plunging motion in each cycle is given by a sinusoidal function.

$$h(t) = h_a \cos(2\pi Strt), \tag{3.4}$$

In Eq. (3.4), h_a is the dimensionless plunging amplitude normalized by the chord length c, and t is the dimensionless time.

The computed thrust and power input coefficients are plotted as functions of the Strouhal number in Fig. 3.1. The computed results are compared to the solutions obtained by Young and Lai [53] and to the results of an experiment on sinusoidal

flapping airfoils conducted by Heathcote and Gursul [22]. Figure 3.1 shows that the present thrust and power input coefficients are in very close agreement with experimental and other numerical results.

As a case for validating the solid module, a thick cylinder which is subjected to an internal pressure load is computed. The detailed contents can be found in Ref. [54]. The dimensional parameters of the test case are

$$a = 0.2 \text{ m}, b = 0.1 \text{ m}, P = 1.0 \times 108 \text{ Pa},$$

$$E = 2.1 \times 1011 \text{ Pa}, \rho = 7850 \text{ kg/m3}, \text{ and } v = 0.3,$$

where a is the outer radius, b is the inner radius, P is the pressure load, E is the modulus of elasticity, ρ is the density, and v is the Poisson ratio. Computation is performed with a number of 7,288 triangular elements. Table III.1 shows a comparison of the present results with the analytic solutions and numerical results obtained by the commercial code, NISAⅡ. It is seen that the present inner and outer radial displacements are in very good agreement with other results within a relative error of 1%.

Table III.1 Comparison of radial displacement.

Unit: mm

	Theoretical	NISA II	Present
Inner radial displacement	0.079365	0.079299	0.079944
Outer radial displacement	0.063492	0.063459	0.063784

3.1.2 Validation of FSI Solver

The present FSI solver is validated with the case of a flexible airfoil oscillating with a constant amplitude of h_a=0.175. Experimental setup was the same as described in the previous sub-chapter.

The airfoil is a 90 mm chord of teardrop/plate design, as shown in Fig. 3.2. The plate is a sheet of uniform thickness with a modulus of elasticity 2.05×10^{11} N/m^2, Poisson ratio 0.3, density 7850 kg/m^3, and length 60 mm. The teardrop element is of chord length 30 mm and made of solid aluminum. Two plates are considered with $b/c = 0.56 \times 10^3$ and 4.23×10^3, where b is the plate thickness and c is the chord length. Simulations are carried out for the Reynolds numbers of 9,000 and 18,000 and for the Strouhal number of $0.2 < Str < 0.5$. The motion of the airfoil is the same as in Eq. (3.2).

For the given Reynolds and Strouhal numbers, the computed temporal trajectories of the leading edge, trailing edge (the end point of the plate) and their relative distances are compared with the corresponding experimental measurements as in Fig. 3.3. It is clear that the present computations agree very well with experiments. Plots of the thrust coefficient and the propulsive efficiency in terms of the Strouhal number are also shown in Fig. 3.4 for two plate thicknesses. To facilitate graphical comparisons with various cases over the range of the Strouhal number considered, the thrust coefficients shown are divided by the square of the corresponding Strouhal numbers. The propulsive efficiency is defined by

$$\eta = \frac{TU_0}{F_y v} = \frac{C_t}{C_p}, \tag{3.5}$$

From Fig. 3.4, close agreements are observed between the present computed results and the experimental measurements both for the thrust coefficient and the propulsive efficiency. Computations and experiments indicates that the thrust coefficient for $b/c = 4.23 \times 10^3$ increases more rapidly than for $b/c = 0.56 \times 10^3$ as the

Strouhal number increases. On the other hand, the propulsive efficiency for $b/c = 0.56 \times 10^3$ is higher than for $b/c = 4.23 \times 10^3$ for all Strouhal numbers.

3.2 FSI Simulation of Blowfly's Tethered Wing Motion

Qualitative comparisons of aerodynamic characteristics are firstly presented between rigid and flexible airfoils. Furthermore, three airfoils reflecting structural flexibility of a blowfly are used and their results are compared quantitatively. FSI flow fields are then examined by changing aerodynamic parameters, such as the Reynolds number and reduced frequency, to confirm that key physical phenomena can be observed in other flow conditions.

There are several ways to define the Reynolds number of an insect's flapping motion. Sometimes, the conventional way of defining the Reynolds number for fixed-wing aircraft may not be appropriate. For example, the Reynolds number based on the freestream velocity cannot be defined in the case of hovering because the conditions of airflow around the wings rapidly change throughout the whole wing beat cycle [47]. The Reynolds number in the present work is defined by using the maximum relative velocity of wing motion. All of the computed aerodynamic coefficients are also normalized by the maximum relative speed. Here, the maximum relative speed is the sum of the freestream velocity and the maximum wing velocity during the flapping motion.

$$\mathrm{Re} = \frac{U_{\max} c_m}{\upsilon}, \tag{3.6}$$

Here, U_{max} is the maximum relative speed defined at the aerodynamic mean chord, and c_m is the mean chord length. The flow conditions including non-dimensional numbers are obtained from Nachtigall's [46] experimental data, as shown in Table III.2.

Table III.2 Flapping motion data (Ref. [46]) and non-dimensional parameters.

Parameter		Value
Airspeed,	U_∞	2.75 m/s
Maximum relative velocity,	U_{max}	9.96 m/s
Mean chord length,	c_m	3.8 mm
Reynolds number,	Re	2523.92
Flapping frequency,	f	130.6Hz
Reduced frequency,	k	0.0498
Stroke plane angle,	β	45°

All computations are carried out for 10 cycles to obtain sufficiently periodic behavior of the aerodynamic coefficients. The fluid-structure coupling procedure at each time step proceeds as follows.

- Receive the new airfoil shape from the solid module using the grid deformation method (The initial airfoil shape is used in the first iteration.)
- Obtain the flow field information based on the updated airfoil shape.
- Transfer the aerodynamic load to the solid module using the data transfer method.
- Obtain the airfoil deformation from the solid module, and transfer the displacement to the fluid module

In this case, the physical time-step of the fluid module is much larger than that of the solid module because the solid module is explicit, and the allowable time-step

is directly proportional to the element size. The physical time-steps between the two modules are synchronized with the loosely coupled FSI approach. For the given fluid time-step, the solid module is advanced in multiple steps by the time-step determined by Eq. (2.10). A time-step sensitivity analysis is carried out with three different levels of the fluid time-step (1/500*T*, 1/1000*T*, and 1/1500*T*, *T* is the non-dimensional flapping period). For each fluid time-step, the solid time-step is fixed and the behavior of aerodynamic force generation is examined. As shown in Fig. 3.5, each result is almost the same. Based on this result, the physical time-step of 1/1000*T* is chosen for the present computations.

3.2.1 Qualitative Comparison of Aerodynamic Characteristics

Figures 3.6 and 3.7 show histories of the instantaneous lift and thrust coefficients. Downstroke and upstroke are indicated by white and blue regions, respectively. Plots are shown for the rigid airfoil and for linear and homogeneous types of flexible airfoils. In all three cases, Lift is mainly generated during downstroke motion, while thrust is impulsively produced at the end of upstroke. These results are similar to earlier findings from simulations of two-dimensional rigid elliptic airfoils [13].

Since the computed results of the two flexible airfoils are very similar, only the linear flexible airfoil is compared with the rigid airfoil. Figure 3.8 shows snapshots of the flow patterns around the two airfoils illustrating the formation and shedding of vortices at leading and trailing edges during downstroke. Figure 3.9 shows the sequential vorticity contours at the end of upstroke. Key physical phenomena and flow patterns such as the LEV, vortex pairing, and vortex staying are still observed in the flexible airfoil. Figure 3.10 depicts a comparison of pressure and velocity fields between the two airfoils at the beginning of downstroke. The center of the leading-

edge vortex (LEV) and pressure suction is almost the same with each other. As a close-up view of Fig. 3.8-(a), Fig. 3.11 shows velocity and vorticity fields around the two airfoils in the wake region. A pair of vortices and a subsequent strong jet is clearly observed in both cases. Figure 3.12 shows the pressure and velocity distributions over the airfoils around t = 180.254 when thrust becomes maximal. The vortex staying mechanism observed in both airfoils is almost the same.

At the same time, some differences are also observed as shown in Fig. 3.6. Early in downstroke, the flexible airfoil generates more lift. This is because the structural deformation induces a camber effect to the airfoil, which increases an effective angle of attack, as shown in Fig. 3.13. As a result, the size and intensity of the LEV is increased [55]. It is well known that the lift enhancement arises from the development and shedding of the LEV. As shown in Fig. 3.14-(a), the low-pressure region at leading edge of the flexible airfoil is found to be wider and stronger than that of the rigid one. Figure 3.15 illustrates the magnitude and direction of the net force vector by integrating surface pressure (the effect of shear stress is negligible). In Fig. 3.15-(a) which corresponds to Fig. 3.14-(a), the magnitude of the net force vector is larger in the flexible airfoil owing to higher pressure difference, and it eventually brings the lift enhancement in the flexible airfoil.

On the contrary, at the middle of downstroke, the rigid airfoil produces more lift than the flexible one. The flexible airfoil creates a negative camber effect due to structural flexibility, and now the effective angle of attack decreases (see Fig. 3.13). As a result, the vortex intensity at the middle of the upper surface is considerably weakened. This is clearly seen from Fig. 3.14-(b). When airfoil experiences structural deformation as in Fig. 3.15-(b) which corresponds to Fig. 3.14-(b), the net force vector acting on the airfoil is tilted forward, and lift component decreases accordingly. The tilting of the net force vector acts negatively by creating a thrust component.

At the end of downstroke, airfoil rotates clockwise and a counterclockwise rotating vortex sheds from the shear layer at trailing edge (Fig. 3.14-(c)). In case of the rigid airfoil, the vortex sheds earlier and stays away from trailing edge, and its intensity is somewhat weak. From the net force vector force in Fig. 3.15-(c) (Fig. 3.14-(c)), negative lift is produced. On the other hand, the vortex shedding from the flexible airfoil is stronger and it stays near trailing edge due to structural deformation. The low-pressure region at trailing edge produces a substantial pressure reversal, and the net pressure difference is close to zero. Consequently, the flexible airfoil generates a close-to-zero lift.

At the end of upstroke, the flexible airfoil is deformed due to the impulsive rotation, which weakens the intensity of the small-size LEV at the lower surface of leading edge (Fig. 3.14-(g)). The intensity of the vortex is slightly stronger in the rigid airfoil, and a relatively lower pressure region is developed. In addition, the structural deformation changes the direction of the net force vector upward, as shown in Fig. 3.15-(d) (Fig. 3.14-(g)). Thus, the rigid airfoil produces a larger negative lift.

As shown in Fig. 3.7, the two airfoils also exhibit some differences in thrust generation. Early in downstroke, a higher negative thrust is observed in the flexile airfoil, which is caused by the camber effect (Fig. 3.14-(h)). The camber effect increases the effective angle of attack, as shown in Fig. 3.13. Stronger pressure suction on the upper surface and a weaker vortex on the lower surface increase the net pressure difference, which acts positively in lift generation but not in thrust generation.

At the middle of downstroke, the flexible airfoil produces a higher thrust by the tilting of the net force vector (Figs. 3.14-(b), 3.15-(b)). Geometric deformation induces a substantial tilting of the net force vector in the forward direction, and thrust component is more generated in the flexible airfoil. In Fig. 3.14-(c), when the airfoil

starts clockwise rotation at the end of downstroke, the flexible airfoil becomes a concave structure. As explained in lift generation, the rigid airfoil generates the downward net force but the net force in the flexible airfoil becomes close-to-zero (Fig. 3.15-(c)).

It is also noted that the direction of the net force vector is not perpendicular to the instantaneous total relative velocity, indicating that a simple Kutta-Joukowski theorem does not hold in this case due to the unsteady viscous effects at high effective angle of attack.

Early in upstroke, in Fig. 3.14-(d), a low-pressure region is widely developed at the lower surface of the flexible airfoil. This is due to the creation of the LEV, as shown in Fig. 3.16-(a). Unlike the rigid airfoil whose motion is almost parallel to the upstroke trajectory, the flexible airfoil has a non-zero angle of attack in the tangential direction of motion, and a small-size LEV is created. A region of relatively low-pressure is formed, especially at the lower leading edge of the flexible airfoil, which produces more thrust component.

At the middle of upstroke, a thrust reversal can be observed between the two airfoils. The location of the LEV generated during downstroke is different, as shown in Figs. 3.14-(e) and 3.16-(b): In the rigid airfoil, it is located at the middle of the upper surface while it stays near the lower surface of leading edge in the flexible airfoil. Thus, the net pressure difference is higher in the flexible airfoil, which results in a higher thrust. However, this situation is quickly reversed. From Figs. 3.14-(f), a new LEV is developed in the lower surface of the rigid airfoil but not in the flexible airfoil. This is because a negative camber effect produced by the flexible airfoil decreases an effective angle of attack (see Fig. 3.13). Consequently, the net pressure difference becomes higher in the rigid airfoil (Fig. 3.14-(f)), and thrust generation pattern is reversed.

The strong jet yielding the thrust peak at the end of upstroke arises from the interaction of two counter-rotating vortices, and this vortex pairing mechanism is impulsively developed [13]. Also, the vortex-staying mechanism caused by the impulsive rotation at the end of upstroke gives rise to the pressure difference across the airfoil. As a consequence, the maximum thrust peak is generated. As in Figs. 3.7, 3.11 and 3.12, these phenomena are observed in the flexible as well as rigid airfoils.

In summary, key physical phenomena and flow patterns such as the LEV, vortex pairing, and vortex staying are essentially the same even when structural flexibility is included. However, noticeable differences are also observed in lift and thrust generation, and they can be explained by the camber effect, vortex intensity and the tilting of the net force vector caused by structural deformation.

3.2.2 Quantitative Comparison on Aerodynamic Performance

Figures 3.6 and 3.7 show histories of the instantaneous lift and thrust coefficients of three airfoils. Overall characteristics are qualitatively similar but quantitative results are somewhat different. Table III.3 compares the time-averaged mean lift and thrust coefficients, and propulsive efficiency, which are evaluated by Eqs. (3.7) and (3.8).

$$\bar{C}_i = \frac{1}{T}\int_0^T C_i dt \,, \tag{3.7}$$

$$\eta = \frac{\bar{C}_t}{\bar{C}_p} \,, \tag{3.8}$$

c_i is the instantaneous aerodynamic coefficient, T is the period of one cycle, η is the propulsive efficiency, and the overbar denotes the mean value.

Table III.3 Comparison of aerodynamic coefficients.

	Rigid	Linear	Homogeneous
C_l	0.754	0.851	0.852
C_t	0.205	0.272	0.260
η	0.491	0.654	0.621

From Table III.3, it is clear that flexible airfoils perform better than the rigid one in every respect. Compared to the rigid airfoil, the net lift is increased by about 12.8% in the homogeneous type. The net thrust and propulsive efficiency are enhanced by about 32.7% and 33.2% in the linear type.

Judging from the overall comparison, the linear-type flexible airfoil exhibits a most improved aerodynamic performance.

3.2.3 Effects of Aerodynamic Parameters

From the prior analysis, physical phenomena such as the LEV, vortex pairing, and vortex staying play a key role in generating sufficient aerodynamic forces. This has been observed in both the rigid and flexible airfoils. In this section, it is examined whether similar phenomena could be observed in other flight conditions. Generally, the frequency range of insect flapping is about 5 ~ 300 Hz, and the range of Reynolds number is $O(10^2)$ - $O(10^4)$ [56, 57]. Parametric study has been carried out by changing the Reynolds number and reduced frequency in the range of the flight conditions.

Considering the blowfly's flight condition, FSI simulations are carried out for the Reynolds numbers ranging from 500 to 4,500 and the reduced frequency ranging from 0.04 to 0.09 (frequency range of about 20 ~ 235 Hz). In all simulations, the wing trajectory keeps the same and the linear-type airfoil is used.

Figures 3.17 and 3.18 show histories of the lift and thrust coefficients for various flight conditions. Each figure shows the behavior of force coefficients depending on the change of the Reynolds number at a given reduced frequency. When the reduced frequency is greater than 0.06, the range of the Reynolds number is limited up to 2523.92. This is because the Reynolds number and reduced frequency are both determined by the realizable flight condition, i.e., the maximum relative speed. If the Reynolds number exceeds 2523.92 with a given reduced frequency (0.06-0.09 in Figs. 3.17 and 3.18), the maximum relative speed yields too much deformation which cannot be observed in real flight condition. In low reduced frequency (0.04 and 0.049813 in Figs. 3.17 and 3.18), high Reynolds number condition is still realizable. From Figs. 3.17 and 3.18, overall pattern for lift and thrust generation is qualitatively quite similar, but at the same time, some quantitative differences are also visible. Figure 3.19 shows snap-shots of the vortex pairing at various conditions. Depending on the reduced frequency, the intensity of the two vortices (or the strength of the induced jet) is different, but all cases clearly show that the two counter-rotating vortices are vertically aligned to produce a strong jet. Also, the LEV and vortex staying can be observed in all cases, as shown in Figs. 3.20 and 3.21. As in Fig. 3.19, the vortex strength increases as the reduced frequency.

By changing aerodynamic parameters in other realizable flight conditions, it is confirmed that key physical phenomena such as the LEV, vortex pairing and vortex staying mechanism are observed in all cases. This indicates that key physical phenomena provide important clues to understand the rapid maneuverability of insect flight in other flight conditions.

Chapter IV
Three-dimensional Insects' Wing-body

4.1 Validation and Verification

As a validation case of the present numerical approach, computations of flapping flight at a low Reynolds number have been conducted for a fruit fly (*Drosophila melanogaster*) under hovering flight conditions described in [21, 58]. In the experiment by Fry *et al*. [58], a flapping robotic wing controlled by several servo motors was devised to measure the aerodynamic forces. The wings were immersed in a 1m × 2.4m × 1.2m towing tank filled with mineral oil. A force transducer attached to the proximal end of the wing measured forces normal and parallel to the wing surface. They designed the force transducer to be insensitive to the position of the force load on the wing.

Figure 4.1-(a) shows a two-block and 5.2 million grid point mesh system used for the geometric modeling of the wing and body. The wing sectional shape is assumed to be a flat plate with 1.2% of mean chord. Figure 4.1-(b) shows flapping wing trajectory of the fruit fly in [21, 58]. Reynolds number is estimated to be 134, and reduced frequency (k) is 0.212. More details of the parameters can be found in Ref. [21]. Figure 4.2 shows the time histories of vertical and horizontal forces. For the given Reynolds number and reduced frequency, the computed results are compared with other computations from Aono *et al*. [21] and experimental measurements of Fry

et al. [58]. From Fig. 4.2, the present computed aerodynamic forces are quite similar with other computations and show reasonable agreement with the experimental data. The vertical force peaks at the middle of down- and upstroke, and the drag force is mostly generated during downstroke while the thrust is produced during upstroke. On the other hand, there exists some phase difference between computational results and experimental data in the time histories of the forces. The difference seems to be caused by an imperfect match, such as a different axis of the wing rotation and a different shape of the wing planform in the computational modeling and the experimental setup. In the present computation, the wing's axis of rotation is assumed to lie at a quarter chord length from the leading edge and the wing planform shape is modeled by using the shape from Aono *et al*. [21].

Verification studies on grid refinement and time step sensitivity have been conducted for the blowfly's forward flight. Two sets of mesh systems are considered: 5.58 and 8.39 million grid points. Comparison between the two mesh systems shows that overall aerodynamic patterns are almost the same and only a slight difference is observed. Maximum difference for lift and thrust coefficients is less than 5% but in most regions it is less than 0.1%, as shown in Figs. 4.3-(a) and 4.3-(b). Time-step sensitivity analysis is carried out with three different levels of time step (1/500*T*, 1/1000*T*, and 1/1500*T*). As shown in Figs. 4.3-(c) and 4.3-(d), the results are quite similar each other. Based on the verification results, 5.58 million grid systems and the physical time step of 1/1000*T* are chosen for efficient and accurate computations.

4.2 Simulation of Blowfly's Tethered Wing Motion

Based on two-dimensional results [12, 13, 28], computations are carried out up to 6 cycles to obtain sufficiently periodic behavior of aerodynamic coefficients.

Physical time step is obtained by dividing one cycle into 1,000 sub-intervals (1/1000*T*). At each physical time step, pseudo-iteration is carried out until both the maximum divergence of velocity and the maximum residual are less than 1×10^{-4}. As in wind tunnel experiment, the direction of thrust and lift is defined with respect to the direction of insect's body. The flow conditions including non-dimensional parameters are obtained from Nachtigall's [46] experimental data, as shown in Table III.2.

4.2.1 Overall Flow Features

Figure 4.4 shows temporal histories of instantaneous lift and thrust coefficients for type-1 (wing only and wing-body) at different body AOA. As in the reported cases of hovering flight [9, 10], overall pattern of lift and thrust generation in wing-body cases is quite similar to that of wing only case. Lift is mainly generated during downstroke, while thrust is impulsively produced at some locations of upstroke.

Following the authors' previous researches [12, 13, 17, 27-30], similar analysis is carried out to examine the role of vortex structures, vortex interactions, and wing-body interactions in three-dimensional lift and thrust generation. Though the overall features are the same, as seen in Fig. 4.4, some differences between the two cases (wing only and wing-body) can be clearly observed. This is because the vortex shedding from the wing interacts with the body surface, as shown in Fig 4.5. It is seen that the body locally affects the shape of the wing vortex and disturbs the streamline in the downstream direction (see the blue dashed box in Fig. 4.5-(a)). This changes the pressure distribution, particularly on the lower wing surface (see Fig. 4.5-(b)), and the aerodynamic forces change accordingly. Likewise, the wing vortex generated by a flapping motion affects the flow field around the body, which again changes the aerodynamic forces on the body. Figure 4.6 and 4.7 respectively show snapshots of vorticity contours and pressure distributions during a flapping motion. As the wing

starts to rotate at the end of upstroke and downstroke, the vortex shedding from the wing sweeps around the body as in Figs. 4.6-(a) to 4.6-(c) and 4.6-(f) to 4.6-(h). At the same time, the wing vortex is closely located to the body surface, and it changes the pressure distribution on the front and/or back of body surface accordingly, as shown in Figs. 4.7-(a) to 4.7-(c) and 4.7-(f) to 4.7-(h). The pattern of aerodynamic coefficients clearly supports the phenomenon. Figure 4.8 shows histories of instantaneous lift and thrust coefficients on the body with and without wing. In the case of wing-body simulation, sudden force fluctuation is clearly observed at the early downstroke and gradual lift fluctuation is seen from the middle of downstroke to the early in upstroke.

As shown in Fig. 4.4, the effect of body AOA exerted a small amount of influence on aerodynamic force generation qualitatively. It can be explained by shed vortex from the body. Figures 4.9 and 4.10 show cross-sectional pressure distributions at the symmetric boundary at the middle of downstroke and upstroke respectively. It is seen that the intensity of the shed vortex is strengthened as the body AOA increases, which develops a low pressure region near the body head. Consequently, it causes small difference of lift and thrust generation.

On the other hand, the strong and noticeable 3-D vortex structure around an insect body is less developed in comparison with the wing vortex, even though the body AOA is 60 degrees. This is because the freestream velocity is relatively low (2.75 m/s) and the body consists of a streamlined shape. The body interferes with the wing vortex flow, and this phenomenon causes some differences between the wing only and wing-body results, as shown in Fig. 4.4. This means that the major effect on force generation is not the body AOA but the wing flapping motion. Nevertheless, the wing-body-vortex interactions according to the body AOA are still observable

quantitatively, which is important for understanding the realistic unsteady aerodynamic features in small-sized insect flight.

4.2.2 Definition of Vortex Structure

In order to explain the detailed three-dimensional flow physics around wing and body, several vortex structures are firstly defined. Vortex structure is classified into two groups. The first group is the vortex structure caused by translational motion normal to wing surface, which is designated translation motion vortex (TMV). A TMV structure is further subdivided into two types: perfect vortex tube (PVT) and perfect vortex ring (PVR). Here, ‘perfect’ means that the direction of vortex tube or ring is not reversed. When the leading edge vortex (LEV) or the trailing-edge vortex (TEV) is combined with the wing-tip vortex (WTV), the resulting vortex structure looks like a ‘tube’. Therefore, this vortex structure is called PVT. Likewise, when three vortices (LEV, WTV, and TEV) in the same direction are completely merged into a single ‘ring’, PVR is formed.

The other group is the vortex structure caused by rotational motion with respect to wing surface, which is designated rotation motion vortex (RMV). The only sub-type of an RMV structure is ‘imperfect’ vortex ring (IPVR). An IPVR is composed of the same three vortices (LEV, WTV, and TEV), but the direction of LEV is opposite to that of TEV. More details of vortex structures can be found in Ref. [17].

In the present research, additional sub-vortex structure is introduced, designated extended perfect vortex tube (EPVT). Here, ‘extended’ means that the wing-root vortex (WRV), which is strongly generated from the root regions during middle downstroke, is added to the PVT, as shown in Fig. 4.11. This vortex structure is developed in the wing only case as well, but does not influence the force generation

of the wing. On the other hand, EPVT affects the pressure distributions on the body by sweeping around the front of the body surface in wing-body simulations.

4.2.3 Wing-Vortex and Vortex-Vortex Interactions

The most conspicuous feature of wing-vortex interaction is the existence of spanwise flow and the delayed stall. Through experimental and computational studies, the existence of the spanwise vortex and its effects has already been reported [5, 16, 59]. The spanwise flow component delays the separation of the LEV, which makes the lift coefficient during downstroke fluctuate much less than in the two-dimensional case [13]. Figure 4.12 depicts the comparison of the vorticity and streamline between the wing only and wing-body case at the middle of downstroke when the wing shape is type-1 and body AOA is 30 deg. The structure of the LEV is almost the same, but the vortices shedding from the leading and trailing edges are somewhat different, which is due to wing-body interaction, as stated above.

The presence of a vortex pairing phenomenon is the most noticeable feature of vortex-vortex interaction in insects' flapping flight. In the two-dimensional study, a vortex pairing phenomenon at the end of upstroke was found to be a crucial factor for impulsive thrust generation [13]. A similar pattern of vortex pairing can be observed in three-dimensional motion. Figure 4.13 shows vorticity and streamline around the wing only and wing-body case when a vortex pairing phenomenon is developed. A pair of vortices behind the trailing edge is clearly observed in both cases. From Fig. 4.13, the clockwise TEV (red arrow) of the wing only case is slightly diffused in the downstream direction, while the shape of the wing-body case is still maintained due to the existence of the body.

4.2.4 Wing-Body Interactions according to the Body AOA

4.2.4.1 Body Effect on the Wing

As seen in Fig. 4.4, a wing without a body produces more lift than the wing-body cases at the middle of downstroke. Figure 4.14 shows the three-dimensional vorticity magnitude and surface pressure distribution of the wing only and wing-body cases around the middle of downstroke when the wing shape is type-1. Owing to the existence of the body, the vortex shedding at previous upstroke (the dashed box in Fig. 4.14) is clearly maintained during downstroke, which causes additional complexity in vortex structure (Fig. 4.14-(b) to 4.14-(f)). The retained vortex in the downstream interacts with the vortex shedding from the wing, and then interrupts a backward movement of the wing vortex. As a result, the shedding velocity from the trailing edge is slightly reduced relative to the wing only case. The surface pressure distribution in Fig. 4.14 clearly supports this observation. The high-pressure region, near the wing root, on the upper and lower surface of each wing-body case is found to be a little wider and stronger than that of the wing only case. Consequently, the change in pressure distribution due to wing-body interaction acts negatively by reducing lift.

This pattern continues as the body AOA increases, except for an AOA above 45 deg. For example, the intensity of the retained vortex at 45 and 60 deg. is much weaker, as shown in Fig. 4.14-(e) and 4.14-(f). At the same time, the pressure on the lower surface is slightly decreased near the root regions. Conversely, the high-pressure region is extended on the upper surface of the wing in the outer region for a 45 deg. AOA and the inner region for 60 deg. When the wing rotates rapidly at the end of upstroke, the rotational direction of the vortex shedding from the body head and the wing are opposite. In an AOA above 45 deg., wing velocity is more impeded by the strong wing-body interaction than in other cases, which produces relatively

high pressure on the upper surface. Nevertheless, the patterns of lift and thrust generation are quite similar in all body AOA, as shown in Fig. 4.4. This is because the pressure distributions on the upper and lower surfaces are roughly balanced, and thus produce comparable aerodynamic forces. This indicates that insects can produce similar flight performance under forward flight condition, even though the body AOA sharply changes.

4.2.4.2 Wing Effect on the Body

Figure 4.15 shows temporal histories of instantaneous lift and thrust coefficients on the body at different body AOA when the wing shape is type-1. From the results, aerodynamic force reversal can be observed at the early downstroke. Figures 4.16 to 4.18 show the vorticity magnitude, cross-sectional pressure and velocity field in the downstream direction at r/R = 0.45, and surface pressure distributions in 0 deg. AOA.

As the wing starts to rotate counterclockwise, a LEV (or part of an IPVR) is developed on the upper surface and interacts with the body, as shown in Fig. 4.16-(a). The LEV creates a low-pressure region on the upper half of the insect back, but does not affect the other portions of the body (Fig. 4.16-(d)). Thus, unbalanced pressure distribution is generated on the back of the body, which produces thrust and negative lift (t = 5.02T). On the other hand, when the wing translates downward, a counterclockwise TEV (or part of a PVR) is generated at the upper trailing edge (Fig. 4.17-(a)). At the same time, strong pressure suction (or velocity vector) between the wing and body increases the net pressure difference (Fig. 4.17-(b) to 4.17-(c)), which acts positively in lift generation but not in thrust generation (t = 5.06T). As the wing gradually moves to the end of downstroke, a strong vortex (or part of an EPVT) is developed from the root regions and sweeps around the body surface, as shown in Fig. 4.18-(a). The vortex normal to the wing surface creates a low-pressure region on the

front of the body (Fig. 4.18-(d)), which causes gradual force reversal from the middle of downstroke to early in the upstroke. A similar pattern is observed for all body AOA.

In conclusion, it is seen from Fig. 4.15 that wing-body interaction causes force fluctuation of the body during flapping motion. This is because the strong vortex shedding from the wing certainly affects the pressure distribution on the body. However, the wing effect on the body does not alter the overall pattern of aerodynamic coefficients, even though the body AOA changes, as shown in Fig. 4.4. This also indicates that flying insects can still maintain their agility regardless of the forward flight condition.

4.2.4.3 Quantitative Comparisons on Aerodynamic Forces

Table IV.1 and Fig. 4.19 show the time-averaged mean aerodynamic forces according to the body AOA on the wing and body respectively, when the wing shape is type-1.

Table IV.1 Comparison of time-averaged mean aerodynamic forces according to the body AOA.

	Wing only	0^o	15^o	25^o
Lift (*N*)	2.036×10^{-4}	1.905×10^{-4}	1.842×10^{-4}	1.839×10^{-4}
Thrust (*N*)	4.556×10^{-5}	3.734×10^{-5}	4.082×10^{-5}	4.523×10^{-5}
L/T	4.47	5.10	4.51	4.07
η	0.447	0.392	0.443	0.491

	30^o	35^o	45^o	60^o
Lift (*N*)	1.886×10^{-4}	1.882×10^{-4}	1.843×10^{-4}	1.805×10^{-4}

Thrust (N)	4.569 x 10^{-5}	3.781 x 10^{-5}	3.667 x 10^{-5}	3.518 x 10^{-5}
L/T	4.13	4.98	5.03	5.13
η	0.488	0.401	0.397	0.389

The aerodynamic forces are evaluated by Eq. (4.1).

$$F_i = \frac{1}{2}\rho_\infty U_m^2 S\bar{C}_i, \tag{4.1}$$

where F_i is the aerodynamic force, ρ_∞ is the air density, S is the planform area (the sum of a single wing and a half body), C_i is the instantaneous aerodynamic coefficient. The propulsive efficiency is given by Eq. (3.8).

It is seen from Fig. 4.19 that certain patterns can be observed as the body AOA increases. For example, a decreasing pattern of lift is shown for the wing and an increasing pattern of lift is seen for the body except at 30 deg., as shown in Fig. 4.19-(a). In addition, an increasing pattern of thrust is observed for the wing except at 25 and 30 deg., as in Fig. 4.19-(b). This means that wing-body interactions are clearly presented in the cases which have a peak value in the net force generation.

Table IV.1 compares the time-averaged mean lift, thrust, lift-to-thrust ratio, and propulsive efficiency between the wing only and wing-body cases. From Table IV.1, the minimum mean lift, supported by one wing and a half body, is 1.805×10^{-4} N at 60 deg. AOA. It follows that two wings and a full body can support at least 3.61×10^{-4} N, which is more than the weight of a typical blowfly of 2.5×10^{-4} N [60]. Conversely, thrust is much smaller than lift. It is known that the lift-to-thrust ratio is about 6 to 7 in hovering flight of insects [61]. For instance, lift may be more than two times the insects' weight, while thrust may be as low as 30% of the weight. In forward flight,

which requires rapid maneuvering, more thrust has to be generated than in hovering flight. Therefore, the lift-to-thrust ratios from the present works ranging from 4 to 5 are quite reasonable, as in Table IV.1.

It is clear from Table IV.1 that the wing only case performs better than wing-body cases in lift generation. However, the most thrust is generated at 30 deg. AOA. This can be explained by wing-body interactions due to the existence of the body, as explained in the above sub-chapters. Compared with 60 deg., net lift is increased by about 5% at 0 deg. and 4% at 30 deg. Net thrust is enhanced by about 30% in the 30 deg. AOA. As well as the aerodynamic forces, the lift-to-thrust ratio and propulsive efficiency is an important factor for maneuverability in a blowfly's forward flight. An advantageous case is shown at 30 deg. AOA which has a low lift-to-thrust ratio, a high propulsive efficiency, and enough aerodynamic forces to support the weight of a blowfly.

An overall comparison reveals that wing-body interactions certainly exist in a blowfly's figure-of-eight motion and 30 deg. AOA exhibits the most improved aerodynamic force generation. This implies that an optimal body AOA may exist in insects' forward flight.

4.2.5 Effects of Wing Shape

4.2.5.1 Effect of Wing Sectional Shape

In order to investigate the effect of wing shape, 30 deg. AOA is chosen because they generate better aerodynamic forces, lift-to-thrust ratio, and propulsive efficiency than the others. Figure 4.20 shows temporal histories of instantaneous lift and thrust coefficients according to the wing shape at the body AOA of 30 deg. The overall patterns of lift and thrust generation are similar in all cases, except for the middle of

downstroke and upstroke. At the middle of downstroke, type-4 and -5 generate more lift than the others, as shown in Fig. 4.20-(a). This is because these two wing types have a camber, which increases the effective angle of attack. As a result, the size and intensity of the LEV is increased. It is well known that this aerodynamic force enhancement arises from the development and the shedding of LEV and/or TEV [2, 5]. Figure 4.21 shows cross-sectional pressure contours in five types of wings at the middle of downstroke. As shown in Fig. 4.21, a low-pressure region at the leading edge of type-4 and -5 is found to be slightly wider and stronger than that of other wings. On the other hand, wing type-1 to -3, in which the sectional shape is a flat plate, generate more lift and thrust than type-4 and -5 at the middle of upstroke, as in Figs. 4.20-(a) and 4.20-(b). When type-4 or 5 moves in the upward direction during upstroke, a negative camber effect exists in the direction of movement, as shown in Fig. 4.22. The negative camber induces a decrease in the effective angle of attack of a blowfly's wing, which affects the size of the LEV negatively. As in Fig. 4.23, the low-pressure region at the leading edge of type-4 and -5 is found to be narrower than that of the others and the high-pressure region that develops at the trailing edge is of greater intensity than that of other wings. Thus, this eventually brings a decrease of lift and thrust in type-4 and -5.

To investigate the effect of thickness, a real thickness of blowfly's wing, such as type-3 and -5, is considered. As shown in Fig. 4.21, the intensity of the LEV in thinner wings (type-3 and -5) is slightly stronger than that of thicker wings (type-2 and -4) at the middle of downstroke. In addition, the shape of the LEV in thinner wings is sharper than that of thicker wings at the middle of upstroke, as in Fig. 4.23. It is also known that the thinner wing allows for a stronger vortex than the thicker one [12]. Thus, a high-pressure region at the trailing edge is extended in the thinner wings, which affects the aerodynamic force generation quantitatively.

4.2.5.2 Effect of Wing Planform

Figure 4.24 shows histories of lift and thrust coefficients on the body according to the wing shape at 30 deg. AOA. It is seen that lift on the body in type-2 to 5 is increased but thrust is decreased compared to type-1 at the early downstroke. This is because the surface pressure distribution on the body is somewhat different between type-1 and other wings. For example, Fig. 4.25 shows a comparison of the surface pressure on the back and front of the body between type-1 and 5. The pressure distribution on the back is similar in each case, while at the front it is quite different near the middle. Type-1 provides more momentum to the body due to the approximated shape of the wing root, and the direction of streamline on the body is tilted upward more than that of type-5, as shown in Fig. 4.26. It causes increase of velocity on the body in type-1, and a region of relatively low pressure forms at the middle part of the body (the dashed box). Consequently, the net pressure difference becomes lower in type-1, which acts negatively on lift generation and positively on thrust generation at the early downstroke.

4.2.5.3 Quantitative Comparisons on Aerodynamic Forces

Table IV.2 compares the time-averaged mean aerodynamic forces according to the wing shape at 30 deg. of body AOA.

Table IV.2 Comparison of time-averaged mean aerodynamic forces according to the wing shape.

	Type-1	Type-2	Type-3	Type-4	Type-5
Lift (*N*)	1.886×10^{-4}	1.813×10^{-4}	1.820×10^{-4}	1.805×10^{-4}	1.861×10^{-4}
Thrust (*N*)	4.569×10^{-5}	4.609×10^{-5}	4.654×10^{-5}	3.013×10^{-5}	3.166×10^{-5}

L/T	4.13	3.93	3.91	5.99	5.88
η	0.488	0.508	0.511	0.334	0.341

From Table IV.2, it is seen that the most thrust, the lowest lift-to-thrust ratio, and the highest propulsive efficiency is generated in type-3. Compared with type-1, net thrust is increased by about 2% in type-3. Although lift in type-3 is decreased compared to type-1, the lift-to-thrust ratio and propulsive efficiency are better than for other wings. This means that type-3 is the most appropriate wing type in a blowfly's forward flight. Therefore, the geometric considerations such as sectional shape and planform have a non-negligible effect on its quantitative aerodynamic characteristics.

Although type-4 and -5 are most similar to a blowfly's wing, the aerodynamic performance is not remarkable compared with other wings. As explained in the effect of wing sectional shape, type-4 and -5 induce a negative camber effect during upstroke, which affects force generation negatively. When a blowfly's wing experiences a figure-of-eight motion, a considerable deformation of wing is expected to be generated in both chordwise and spanwise directions. For example, from the authors' previous 2-D FSI (Fluid-Structure Interaction) research [28], noticeable difference exists in lift and thrust generation as a result of the structural flexibility. In this work, the 3-D wing is assumed to be a rigid, not flexible, body. From this perspective, the aerodynamic performance of a realistic flexible wing could be quite different if an FSI simulation is conducted in the future work.

Chapter V
Concluding Remarks

5.1 Summary

In this dissertation, two primary topics were discussed: the aerodynamic effect of structural flexibility in two-dimensional flapping wing motion and the three-dimensional unsteady aerodynamic features of wing-body-vortex interactions in insects' flapping flight. These two topics are briefly summarized here.

FSI simulations of unsteady viscous incompressible flows over an insect-like flexible airfoil are carried out to investigate the effects of wing flexibility under a forward flight condition. FSI simulations have been conducted using the loosely coupling method. The wing trajectory, geometric shape, and material properties are extracted from experimental data. Two flexible airfoils composed of the linear and homogeneous types are compared with the rigid airfoil under various flight conditions.

Through detailed comparisons of the rigid and flexible airfoils, it is seen that overall behavior of aerodynamic coefficients is qualitatively quite similar. However, structural deformation brings the changes of the effective angle of attack, the vortex intensity and the tilting of the net force vector. As a result, quantitative differences are clearly visible. Comparisons of the computed aerodynamic coefficients reveal that the flexible airfoil does generate a higher performance. The net lift is improved by about 13% in the homogeneous flexible airfoil, while the net thrust and propulsive efficiency are enhanced by about 33% in the linear type. This indicates that wing

flexibility is important in understanding or designing an insect-like flapping airfoil. From extensive FSI simulations, it is also confirmed that key flow characteristics such as the LEV, vortex pairing, and vortex staying can be observed in other forward flight conditions. Consequently, structural flexibility is essential in improving overall aerodynamic performance of flapping flight, and it can be beneficially exploited in the design of insect-aerial-vehicles.

Three-dimensional computations of unsteady, viscous, incompressible flows over a complete insect configuration are carried out to investigate unsteady flowfield characteristics of three-dimensional figure-of-eight motion under forward flight condition. Wing trajectory is extracted from data of the tethered flight experiment of a blowfly under freestream by Nachtigall.

Compared to the results of the wing only case, overall aerodynamic behavior is qualitatively similar to but quantitatively different. Lift is mainly generated during downstroke by leading-edge vortex, and thrust is generated during upstroke. It is observed that vortex structures and interactions are crucial factors in determining the unsteady aerodynamic characteristics of three-dimensional flapping motion. There are three kinds of interactions in three-dimensional full-body simulation: wing-vortex interaction, vortex-vortex interaction, and wing-body interaction.

The most conspicuous feature of wing-vortex interaction is the existence of spanwise flow and vortex ring. Spanwise flows prevents an early detachment of leading-edge vortex, and thus lift during downstroke fluctuates much less than in two-dimensional motion. A vortex pairing phenomenon is the most noticeable feature in vortex-vortex interaction. It comes from the interaction of vortex rings with opposite vortex directions at the end of upstroke.

Through comparisons of the wing only and wing-body simulations, it is seen that the vortex shedding at previous upstroke is strongly maintained during downstroke due to the existence of the body, which causes more complicated wing-body interaction. In addition, the strong vortex shedding from the wing measurably affects aerodynamic forces on the body. Nevertheless, it is seen that the overall pattern of aerodynamic forces is qualitatively similar according to the body AOA. This indicates that insects can produce stable forward flight performance even though the body AOA rapidly changes. On the other hand, quantitative differences are clearly visible. The body AOA of 30 deg. exhibits the most improved aerodynamic force generation in the present investigation. Comparisons of the wing sectional shape and planform reveal that geometric considerations have a substantial influence on the aerodynamic force generation. From the results, type-3 yields the best aerodynamic performance in forward flight, but the effect of structural flexibility should be taken into account as a future work. Consequently, complicated wing-body interactions and geometric factors, such as body angle and wing shape, should be considered for investigating the aerodynamic performance of flapping flight and this can be used in the design of small sized aerial vehicles.

5.2 Future Works

Based on the present research, efforts are in progress to investigate the effects of wing flexibility in unsteady aerodynamic characteristics. Several future works are summarized as follows.

- A three-dimensional flexible flapping wing and wing-body simulation: To find out the flexibility effects of the insects' wing motion.

- Design of a two- and three-dimensional flexible flapping wing trajectory with simple motion component: To design simple and efficient flapping wing trajectory application to small-sized flapping aerial vehicles development.
- Design and manufacture of flapping MAVs: To develop a flapping/control mechanism through the optimized design system.

References

[1] Ellington, C. P. "The novel aerodynamics of insect flight: applications to micro-air vehicles," *Journal of Experimental Biology* Vol. 202, No. 23, 1999, pp. 3439-3448.

[2] Ellington, C. P., Van Den Berg, C., Willmott, A. P., and Thomas, A. L. "Leading-edge vortices in insect flight," 1996.

[3] Ward-Smith, A. J. *Biophysical Aerodynamics and the Natural Environment*: John Willy & Sons, 1984.

[4] Dickinson, M. H., and Gotz, K. G. "Unsteady aerodynamic performance of model wings at low Reynolds numbers," *Journal of Experimental Biology* Vol. 174, No. 1, 1993, pp. 45-64.

[5] Dickinson, M. H., Lehmann, F.-O., and Sane, S. P. "Wing rotation and the aerodynamic basis of insect flight," *Science* Vol. 284, No. 5422, 1999, pp. 1954-1960.

[6] Singh, B., and Chopra, I. "Insect-based hover-capable flapping wings for micro air vehicles: experiments and analysis," *AIAA journal* Vol. 46, No. 9, 2008, pp. 2115-2135.

[7] Nagai, H., and Isogai, K. "Effects of Flapping Wing Kinematics on Hovering and Forward Flight Aerodynamics," *AIAA journal* Vol. 49, No. 8, 2011, pp. 1750-1762.

[8] Okamoto, M., and Azuma, A. "Aerodynamic Characteristics at Low Reynolds Number for Wings of Various Planforms," *AIAA journal* Vol. 49, No. 6, 2011, pp. 1135-1150.

[9] Sun, M., and Yu, X. "Aerodynamic force generation in hovering flight in a tiny insect," *AIAA journal* Vol. 44, No. 7, 2006, pp. 1532-1540.

[10] Liu, H., and Kawachi, K. "A numerical study of insect flight," *Journal of Computational Physics* Vol. 146, No. 1, 1998, pp. 124-156.

[11] Ramamurti, R., and Sandberg, W. C. "A three-dimensional computational study of the aerodynamic mechanisms of insect flight," *Journal of Experimental Biology*

Vol. 205, No. 10, 2002, pp. 1507-1518.

[12] Lee, J.-S., and Kim, C. "Design of flapping airfoil for optimal aerodynamic performance in low-reynolds number flows," *AIAA journal* Vol. 44, No. 9, 2006, pp. 1960-1972.

[13] Lee, J.-S., Kim, J.-H., and Kim, C. "Numerical study on the unsteady-force-generation mechanism of insect flapping motion," *AIAA journal* Vol. 46, No. 7, 2008, pp. 1835-1848.

[14] Platzer, M. F., Jones, K. D., Young, J., and S. Lai, J. "Flapping wing aerodynamics: progress and challenges," *AIAA journal* Vol. 46, No. 9, 2008, pp. 2136-2149.

[15] Wang, J. K., and Sun, M. "A computational study of the aerodynamics and forewing-hindwing interaction of a model dragonfly in forward flight," *Journal of experimental biology* Vol. 208, No. 19, 2005, pp. 3785-3804.

[16] Ramamurti, R., and Sandberg, W. C. "A computational investigation of the three-dimensional unsteady aerodynamics of Drosophila hovering and maneuvering," *Journal of Experimental Biology* Vol. 210, No. 5, 2007, pp. 881-896.

[17] Kim, J.-H., and Kim, C. "Computational investigation of three-dimensional unsteady flowfield characteristics around insects' flapping flight," *AIAA journal* Vol. 49, No. 5, 2011, pp. 953-968.

[18] Swanson, T. A., and Isaac, K. "Planform and Camber Effects on the Aerodynamics of Low-Reynolds-Number Wings," *Journal of Aircraft* Vol. 47, No. 2, 2010, pp. 613-621.

[19] Liu, H. "Integrated modeling of insect flight: from morphology, kinematics to aerodynamics," *Journal of Computational Physics* Vol. 228, No. 2, 2009, pp. 439-459.

[20] Yu, X., and Sun, M. "A computational study of the wing–wing and wing–body interactions of a model insect," *Acta mechanica sinica* Vol. 25, No. 4, 2009, pp. 421-431.

[21] Aono, H., Liang, F., and Liu, H. "Near-and far-field aerodynamics in insect hovering flight: an integrated computational study," *Journal of Experimental Biology* Vol. 211, No. 2, 2008, pp. 239-257.

[22] Heathcote, S., and Gursul, I. "Flexible flapping airfoil propulsion at low Reynolds numbers," *AIAA journal* Vol. 45, No. 5, 2007, pp. 1066-1079.

[23] Pederzani, J.-N., and Haj-Hariri, H. "Numerical analysis of heaving flexible airfoils in a viscous flow," *AIAA journal* Vol. 44, No. 11, 2006, pp. 2773-2779.

[24] Olivier, M., Dumas, G., and Morissette, J. "A fluid-structure interaction solver for nano-air-vehicle flapping wings," AIAA paper 2009-3676, 2009.

[25] Chandar, D. D., and Damodaran, M. "Computational fluid-structure interaction of a flapping wing in free flight using overlapping grids," AIAA paper 2009-3849, 2009.

[26] Shyy, W., Aono, H., Chimakurthi, S. K., Trizila, P., Kang, C.-K., Cesnik, C. E., and Liu, H. "Recent progress in flapping wing aerodynamics and aeroelasticity," *Progress in Aerospace Sciences* Vol. 46, No. 7, 2010, pp. 284-327.

[27] Kim, J.-H., and Kim, C. "Unsteady Flowfields Characteristics Around Two-and Three-dimensional Flapping Flight," AIAA paper 2008-6400, 2008.

[28] Lee, K.-B., Kim, J.-H., and Kim, C. "Aerodynamic Effects of Structural Flexibility in Two-Dimensional Insect Flapping Flight," *Journal of aircraft* Vol. 48, No. 3, 2011, pp. 894-909.

[29] Lee, K.-B., Kim, J.-H., Park, J. S., and Kim, C. "Unsteady Aerodynamic Effects of Wing-body Interactions in Three-dimensional Insects' Flapping Flight," AIAA paper 2012-419, 2012.

[30] Lee, K.-B., and Kim, C. "Three-dimensional Unsteady Aerodynamic Characteristics of Wing-body-vortex Interactions in Insects' Flapping Flight," AIAA paper 2013-2668, 2013.

[31] Cook, R. D., Malkus, D. S., Plesha, M. E., and Witt, R. J. *Concepts and Applications of Finite Element Analysis*: John Wiley & Sons, 2002.

[32] Chorin, A. J. "Numerical solution of the Navier-Stokes equations," *Mathematics of computation* Vol. 22, No. 104, 1968, pp. 745-762.

[33] Ok, H. "Development of an Incompressible Navier-Stokes Solver and Its Application to the Calculation of Separated Flows," Ph.D. Thesis, Univ. of Washington, Seattle, WA, 1993

[34] Rai, M. M., and Chakravarthy, S. R. "An implicit form for the Osher upwind

scheme," AIAA paper 1984.

[35] Hirsch, C. "Numerical computation of internal and external flows. Vol. 2-Computational methods for inviscid and viscous flows," *Chichester, England and New York, John Wiley & Sons, 1990, 708 p.* Vol. 1, 1990.

[36] Menter, F. R. "Assessment of higher order turbulence models for complex two- and three-dimensional flowfields," *NASA STI/Recon Technical Report N* Vol. 93, 1992, p. 20035.

[37] Rogers, S., and Kwak, D. "Upwind differencing scheme for the time-accurate incompressible Navier- Stokes equations," *AIAA journal* Vol. 28, No. 2, 1990, pp. 253-262.

[38] Tannehill, J. C., Anderson, D. A., and Pletcher, R. H. *Computational fluid mechanics and heat transfer*: Taylor & Francis Group, 1997.

[39] Yoon, S., and Kwak, D. "Three-dimensional incompressible Navier-Stokes solver using lower-upper symmetric-Gauss-Seidel algorithm," *AIAA journal* Vol. 29, 1991, p. 874.

[40] Guruswamy, G. "A new modular approach for tightly coupled fluid/structure analysis," *International Journal of Aerospace Innovations* Vol. 1, No. 1, 2009, pp. 1-10.

[41] Cebral, J. R., and Lohner, R. "Conservative load projection and tracking for fluid-structure problems," *AIAA journal* Vol. 35, No. 4, 1997, pp. 687-692.

[42] Jiao, X., and Heath, M. T. "Common-refinement-based data transfer between non-matching meshes in multiphysics simulations," *International Journal for Numerical Methods in Engineering* Vol. 61, No. 14, 2004, pp. 2402-2427.

[43] Liu, X., Qin, N., and Xia, H. "Fast dynamic grid deformation based on Delaunay graph mapping," *Journal of Computational Physics* Vol. 211, No. 2, 2006, pp. 405-423.

[44] Sane, S. "The aerodynamics of insect flight," *Journal of experimental biology* Vol. 206, No. 23, 2003, pp. 4191-4208.

[45] Wang, Z. "Dissecting Insect Flight," *Annu. Rev. Fluid Mech* Vol. 37, 2005, pp. 183-210.

[46] Nachtigall, W. *Insects in flight*: McGraw-Hill, 1974.

[47] Brodskiĭ, A. K. *The Evolution of Insect Flight*. Oxford: Oxford University Press, 1996.

[48] Lee, J. S. "Numerical Study on Flapping-Airfoil Design and Unsteady Mechanism of Two-Dimensional Insect Wing," Ph.D. Thesis, Seoul National Univ., Seoul, Republic of Korea, 2006

[49] Kesel, A. B., Philippi, U., and Nachtigall, W. "Biomechanical aspects of the insect wing: an analysis using the finite element method," *Computers in Biology and Medicine* Vol. 28, No. 4, 1998, pp. 423-437.

[50] Wainwright, S. A. *Mechanical Design in Organisms*: Princeton University Press, 1982.

[51] Schilstra, C., and Hateren, J. v. "Blowfly flight and optic flow. I. Thorax kinematics and flight dynamics," *Journal of Experimental Biology* Vol. 202, No. 11, 1999, pp. 1481-1490.

[52] Kim, C. S., Kim, C., and Rho, O. H. "Parallel computations of high-lift airfoil flows using two-equation turbulence models," *AIAA journal* Vol. 38, No. 8, 2000, pp. 1360-1368.

[53] Young, J., and Lai, J. "Oscillation frequency and amplitude effects on the wake of a plunging airfoil," *AIAA journal* Vol. 42, No. 10, 2004, pp. 2042-2052.

[54] Warren Young, R. B. *Roark's Formulas for Stress and Strain*: McGraw-Hill, 1989.

[55] Tuncer, I. H., and Platzer, M. F. "Computational study of flapping airfoil aerodynamics," *Journal of Aircraft* Vol. 37, No. 3, 2000, pp. 514-520.

[56] BYRNE, D. N., BUCHMANN, S. L., and SPANGLER, H. G. "Relationship between wing loading, wingbeat frequency and body mass in homopterous insects," *Journal of Experimental Biology* Vol. 135, No. 1, 1988, pp. 9-23.

[57] Dudley, R. *The Biomechanics of Insect Flight: Form, Function, Evolution*: Princeton University Press, 2000.

[58] Fry, S. N., Sayaman, R., and Dickinson, M. H. "The aerodynamics of hovering flight in Drosophila," *Journal of Experimental Biology* Vol. 208, No. 12, 2005, pp. 2303-2318.

[59] Birch, J. M., and Dickinson, M. H. "Spanwise flow and the attachment of the leading-edge vortex on insect wings," *Nature* Vol. 412, No. 6848, 2001, pp. 729-

733.

[60] Buckholz, R. H. "Measurements of unsteady periodic forces generated by the blowfly flying in a wind tunnel," *Journal of Experimental Biology* Vol. 90, No. 1, 1981, pp. 163-173.

[61] Wang, Z. J. "Dissecting insect flight," *Annu. Rev. Fluid Mech.* Vol. 37, 2005, pp. 183-210.

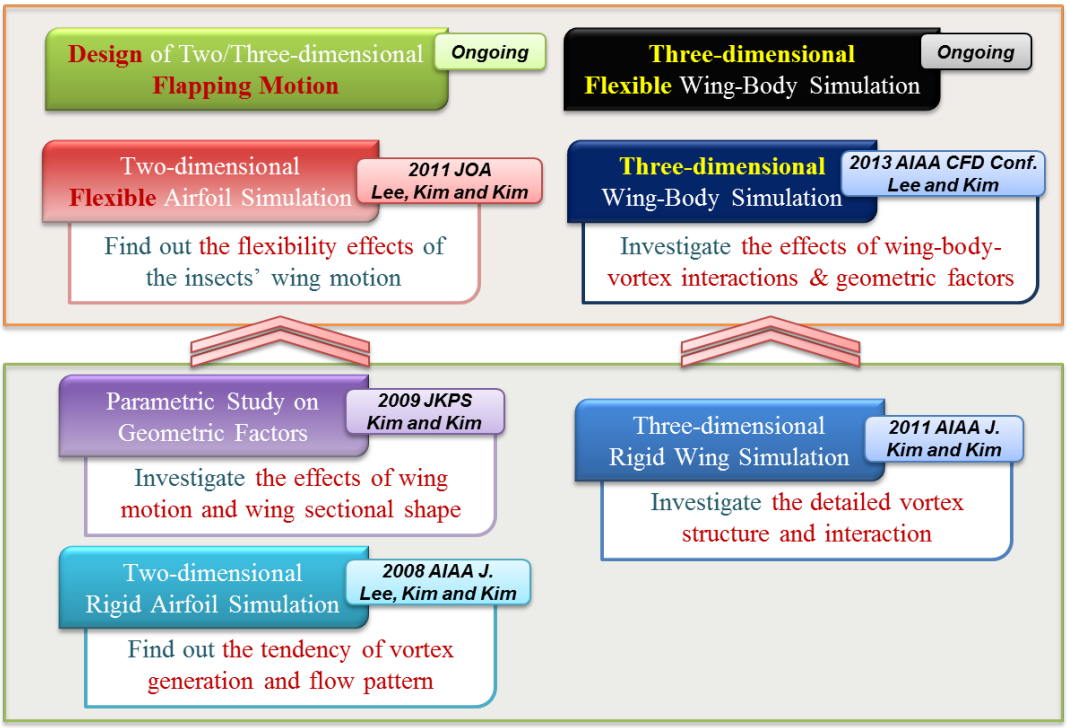

Figure 1.1 Strategic research roadmap for insects' flapping flight

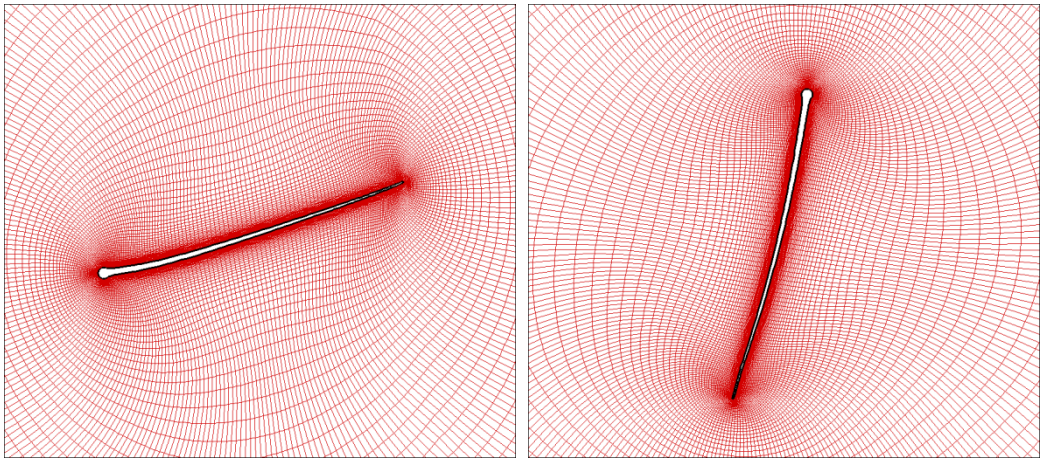

(i) mesh during downstroke **(ii) mesh during upstroke**

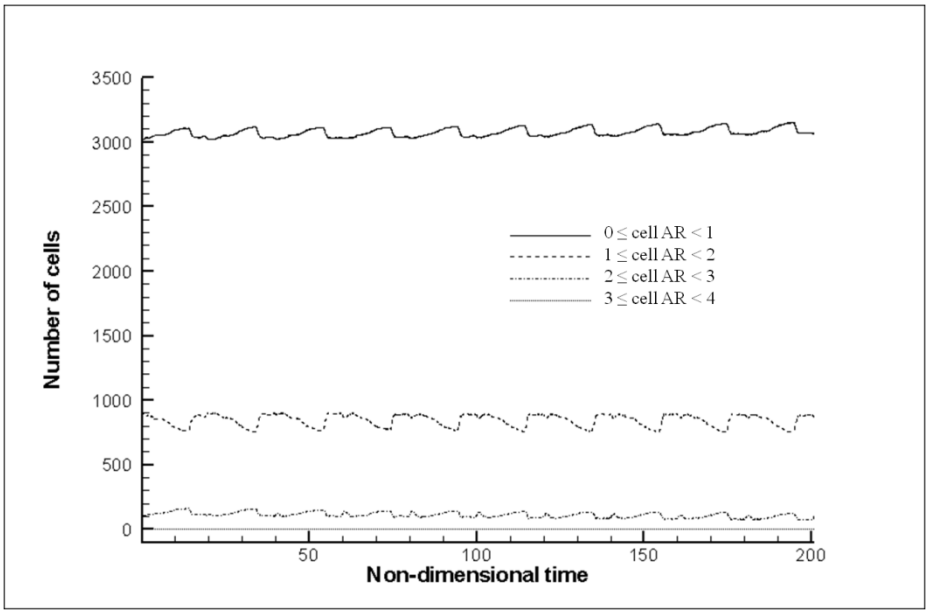

Figure 2.1 Mesh deformation for a flapping airfoil (up) and histories of the cell aspect ratio distribution (down)

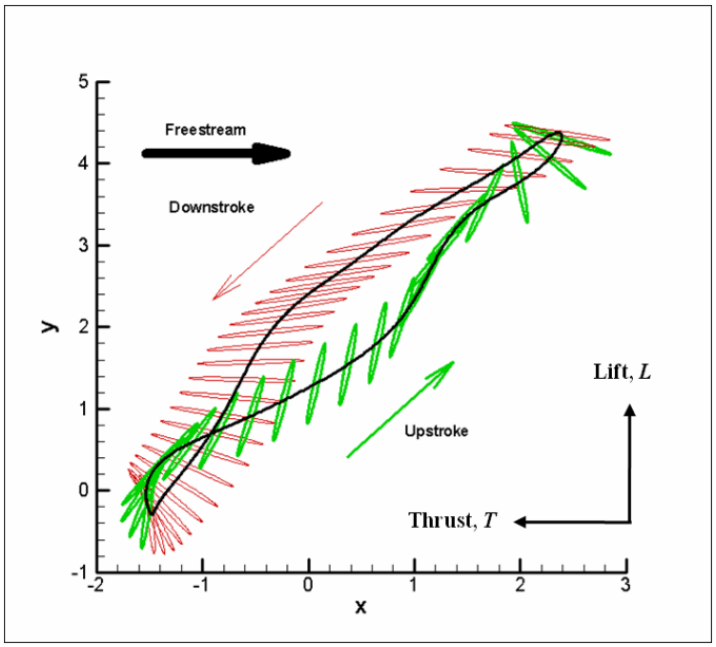

Figure 2.2 Non-dimensional position of a blowfly's wing element during tethered flight, Down-stroke phase (red solid), upstroke phase (green solid).

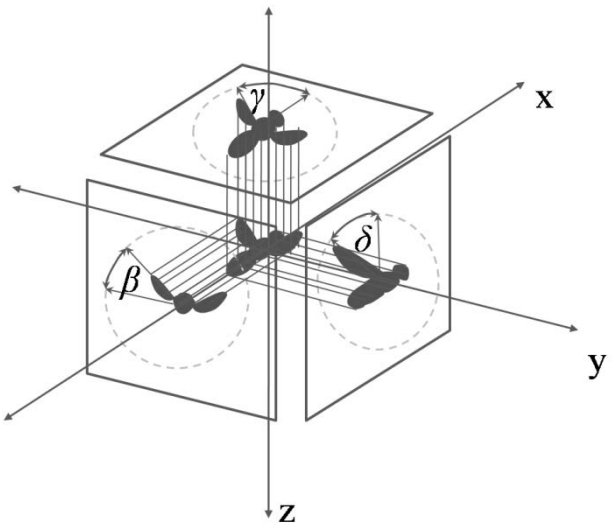

Figure 2.3 Projection of a flying insect onto three perpendicular planes (xy, yz, zx).

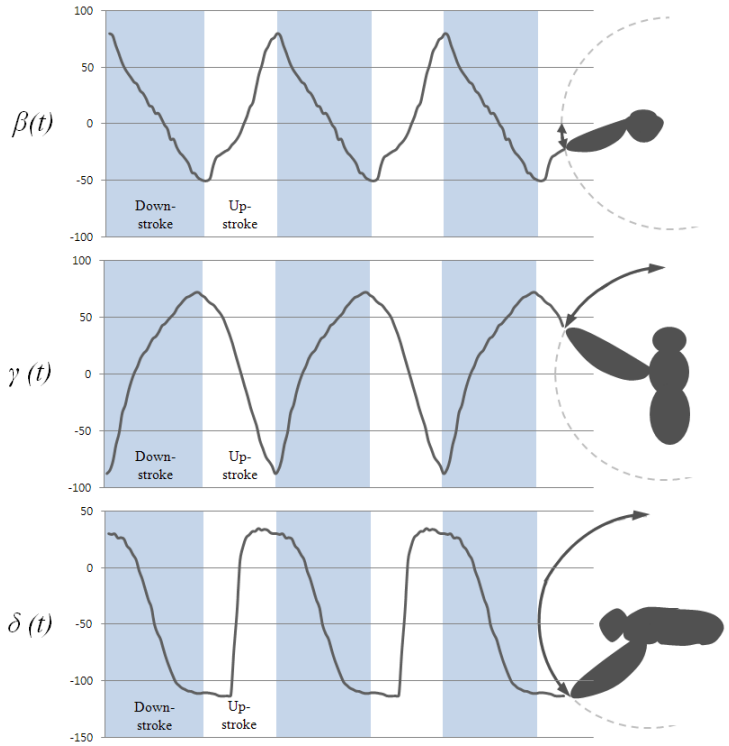

Figure 2.4 Time History of three angles (*β*, *γ*, *δ*) as a function of wing beat (Ref. [46]).

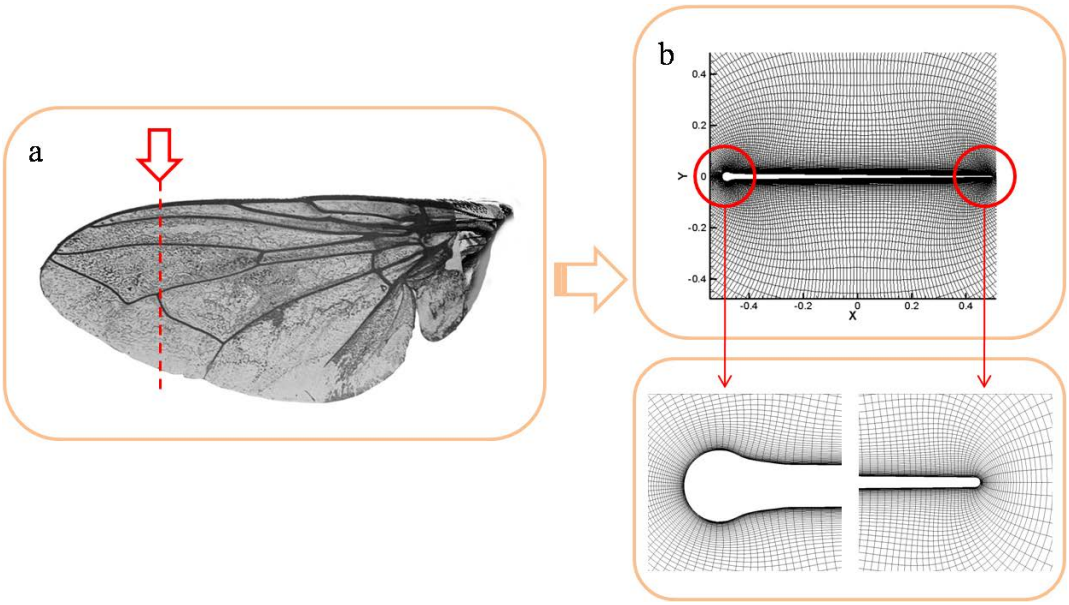

Figure 2.5 Geometric modeling (a) real insect wing and (b) tadpole-type wing.

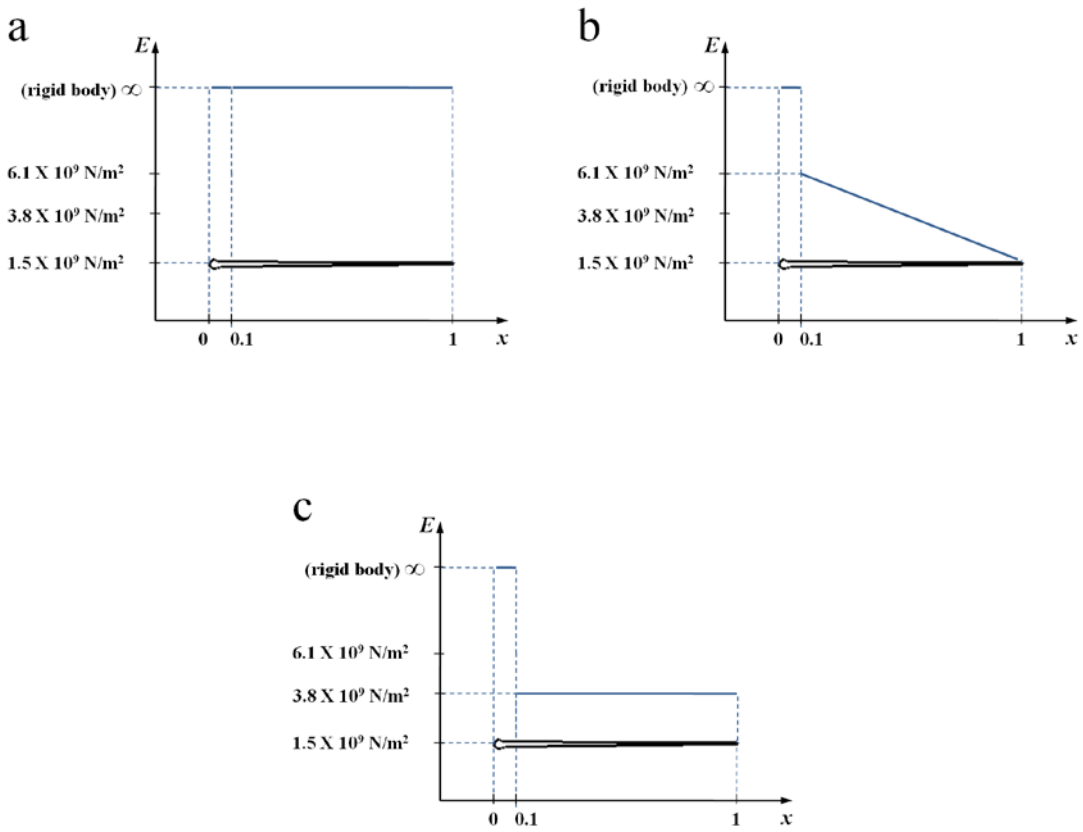

Figure 2.6 Structural modeling (a) rigid airfoil, (b) linear-type airfoil, and (c) homogeneous-type airfoil.

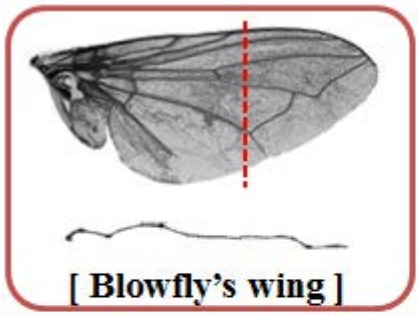

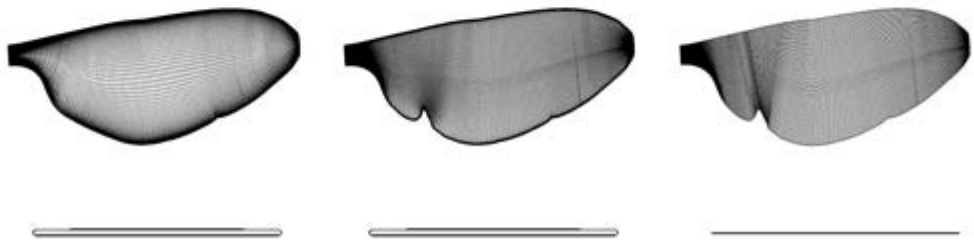

a) **b)** **c)**

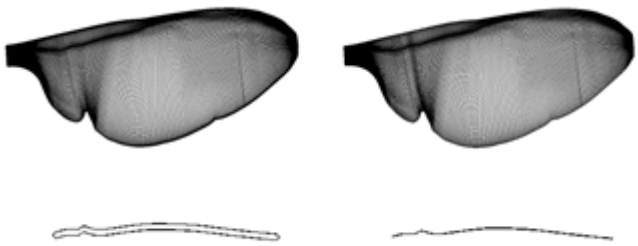

d) **e)**

Figure 2.7 Geometric modeling of a blowfly's wing planform and sectional shape: a) type-1, b) type-2, c) type-3, d) type-4, and e) type-5.

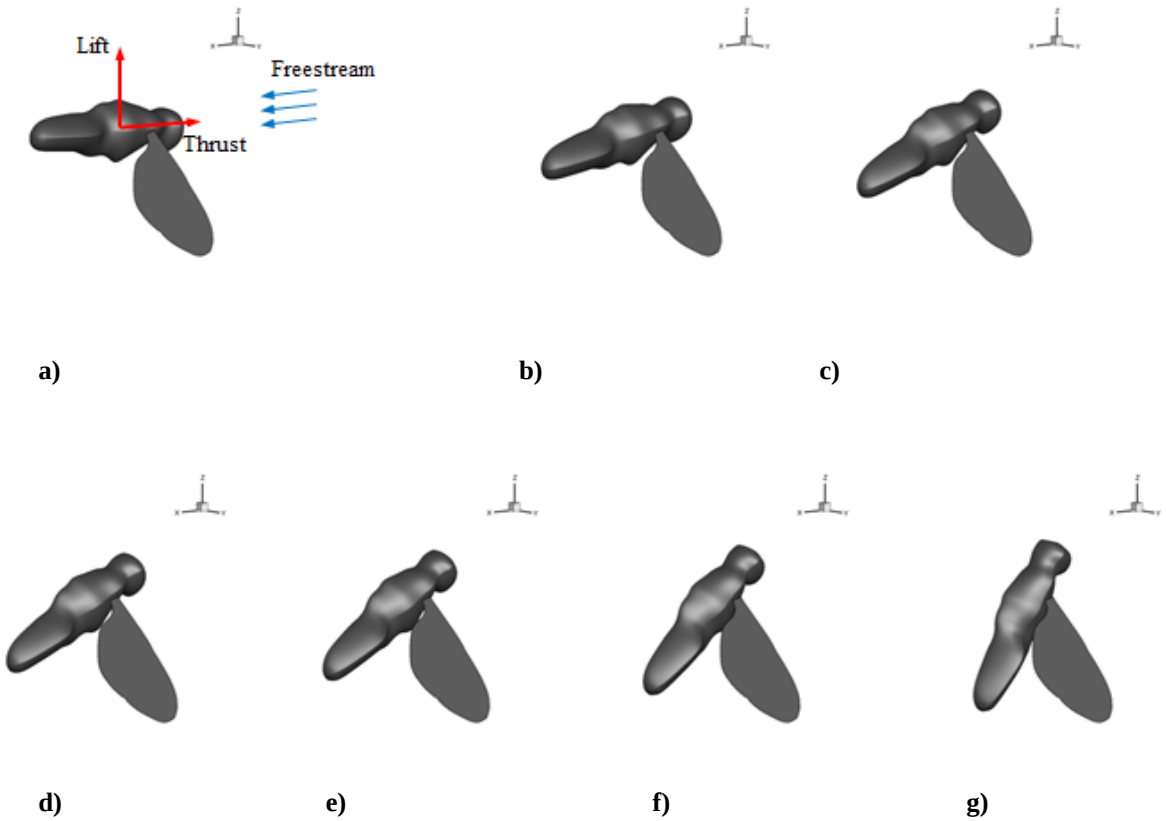

Figure 2.8 Body angle of attack of a blowfly: a) 0°, b) 15°, c) 25°, d) 30°, e) 35°, f) 45°, and g) 60°.

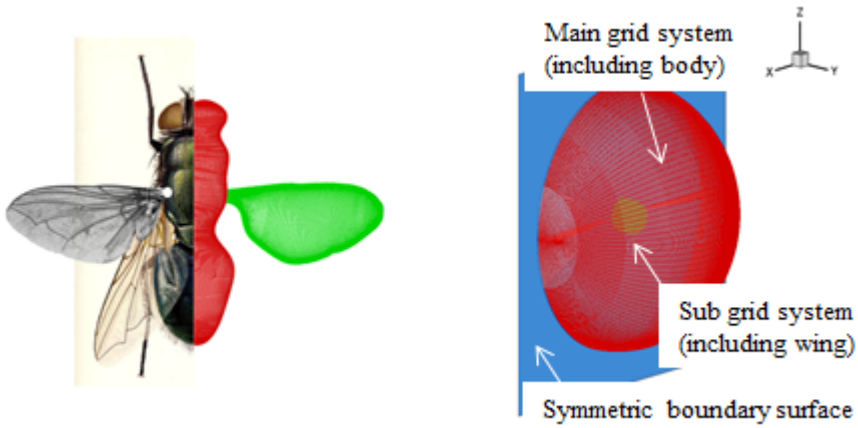

a) **b)**

c) **d)**

Figure 2.9 Geometric modeling of a blowfly's full-body: a) blowfly's surface grids, b) overlapped grid system, c) main grid system (including body), and d) sub grid system (including wing).

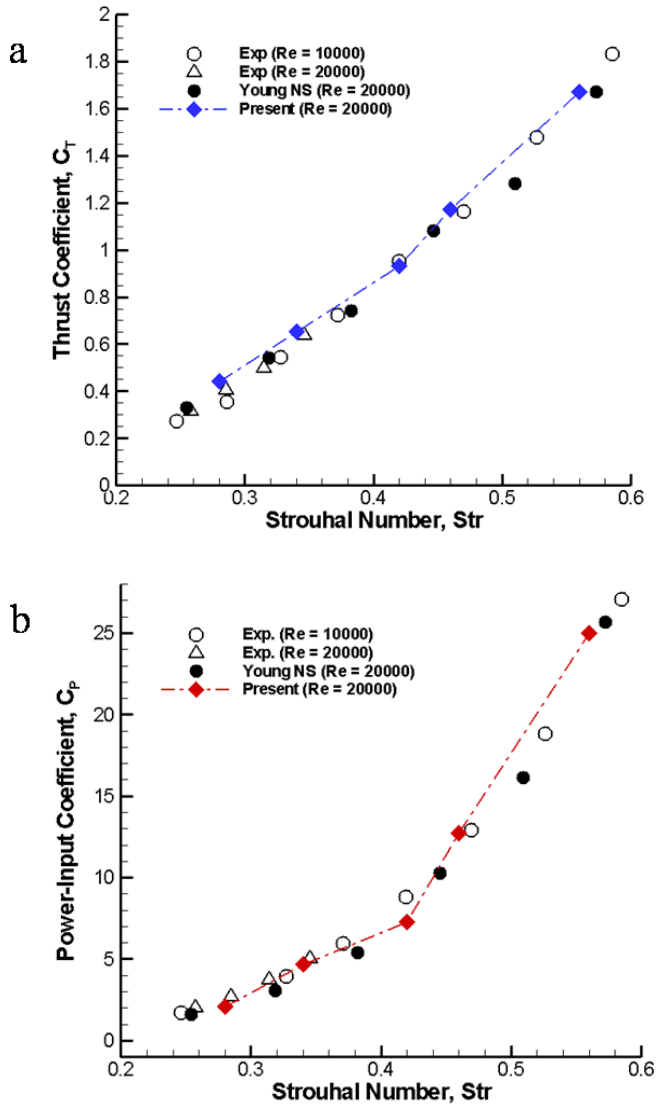

Figure 3.1 Comparison of numerical results with experimental data (a) thrust coefficient and (b) power-input coefficient.

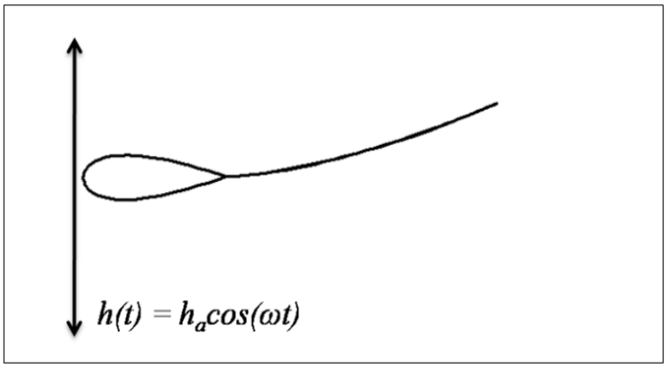

Figure 3.2 Flat plate with a teardrop element at leading edge.

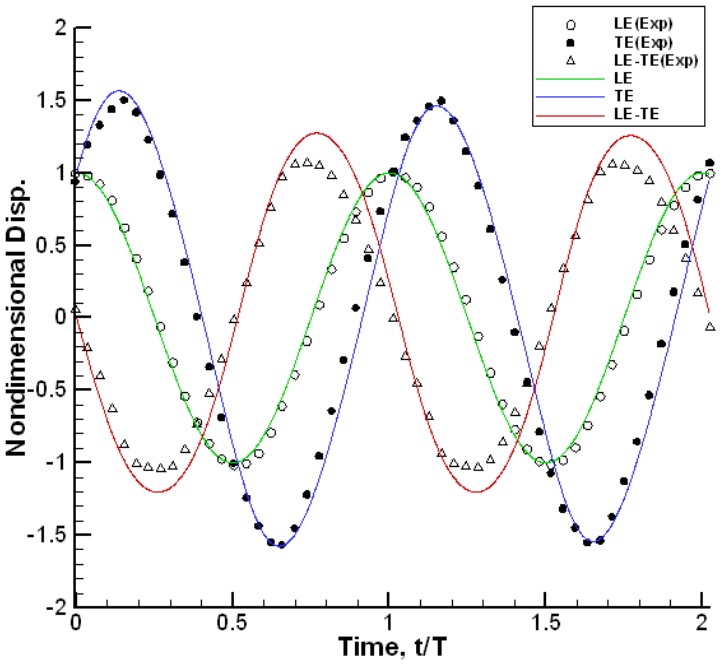

Figure 3.3 Histories of displacements at leading and trailing edges (*Re* = 9,000, *Str* = 0.34, *b/c* = 0.56×10^3).

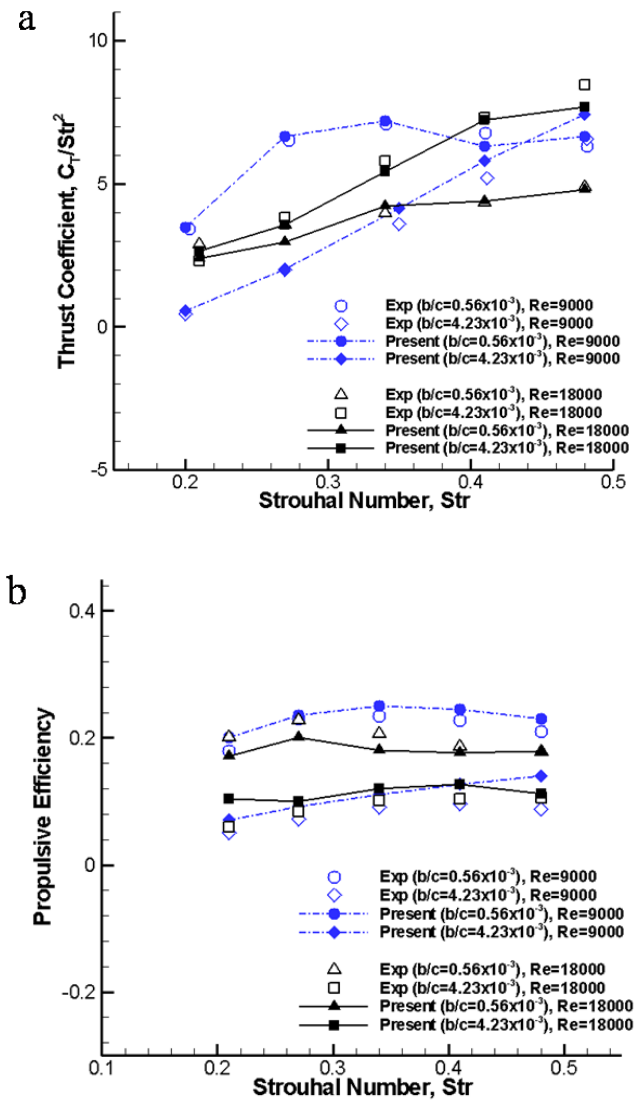

Figure 3.4 Comparison of numerical results with experimental data (a) thrust coefficient and (b) propulsive efficiency.

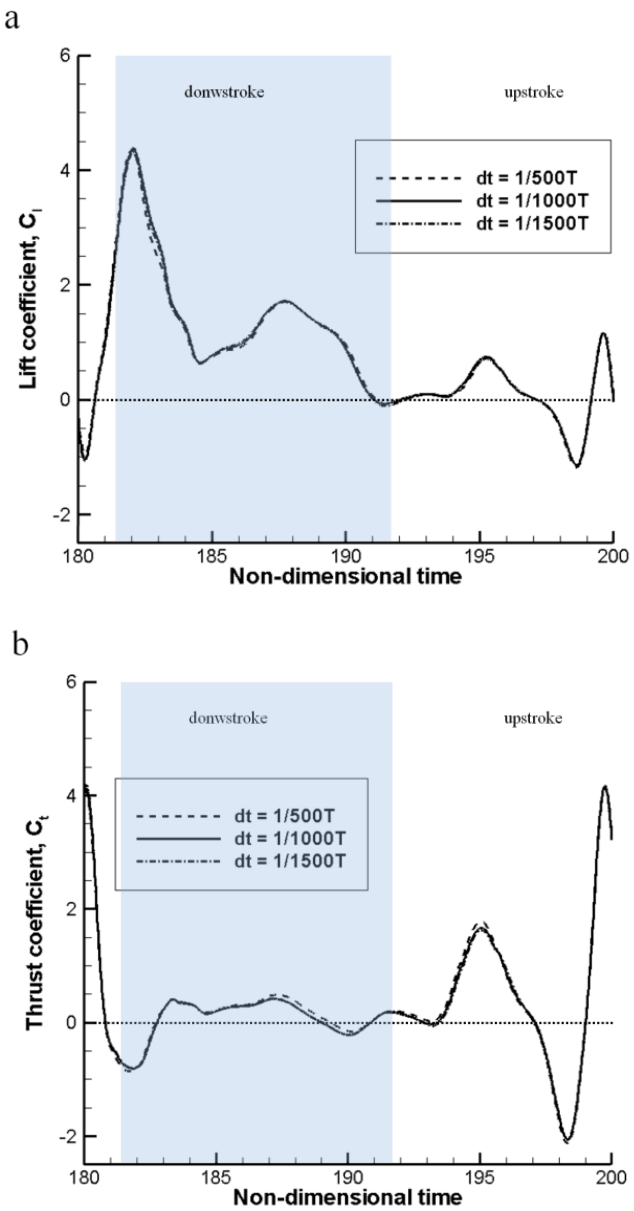

Figure 3.5 Effect of time-step sensitivity on aerodynamic force generation (a) lift coefficient and (b) thrust coefficient.

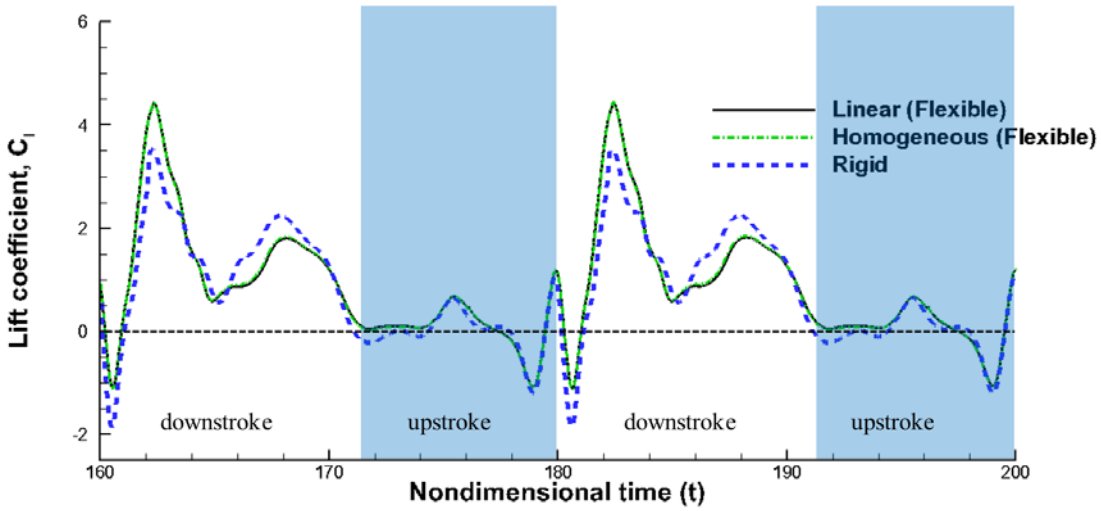

Figure 3.6 Histories of instantaneous lift coefficients.

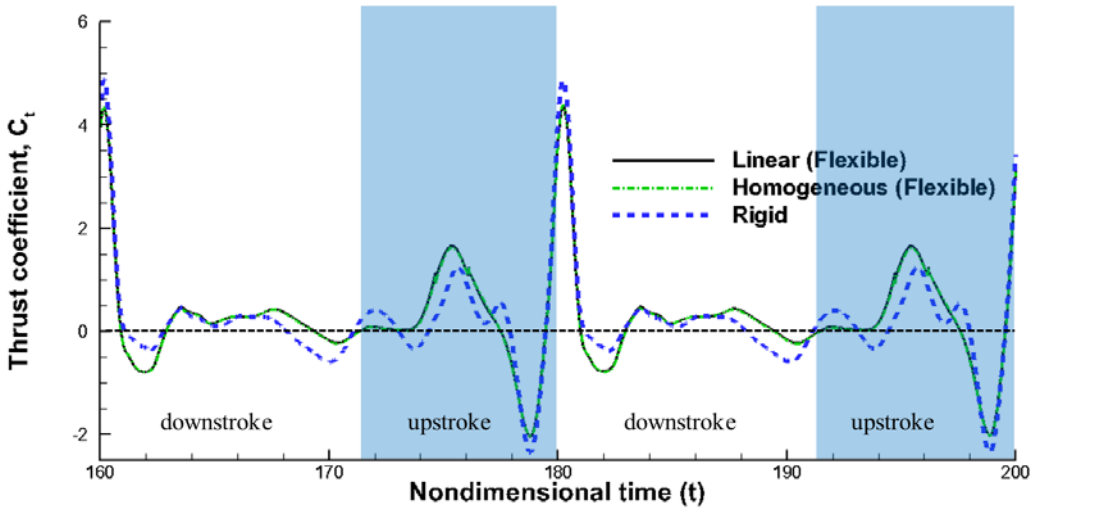

Figure 3.7 Histories of instantaneous thrust coefficients.

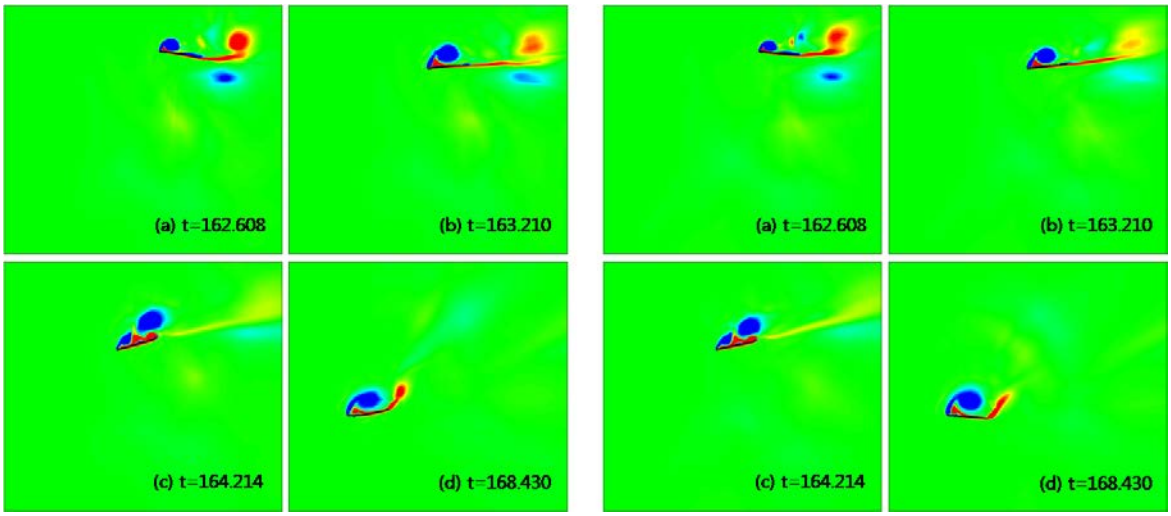

(i) flexible airfoil **(ii) rigid airfoil**

Figure 3.8 Vorticity contours during downstroke (a) t = 162.608, (b) t =163.210, (c) t = 164.214, and (d) t = 168.430.

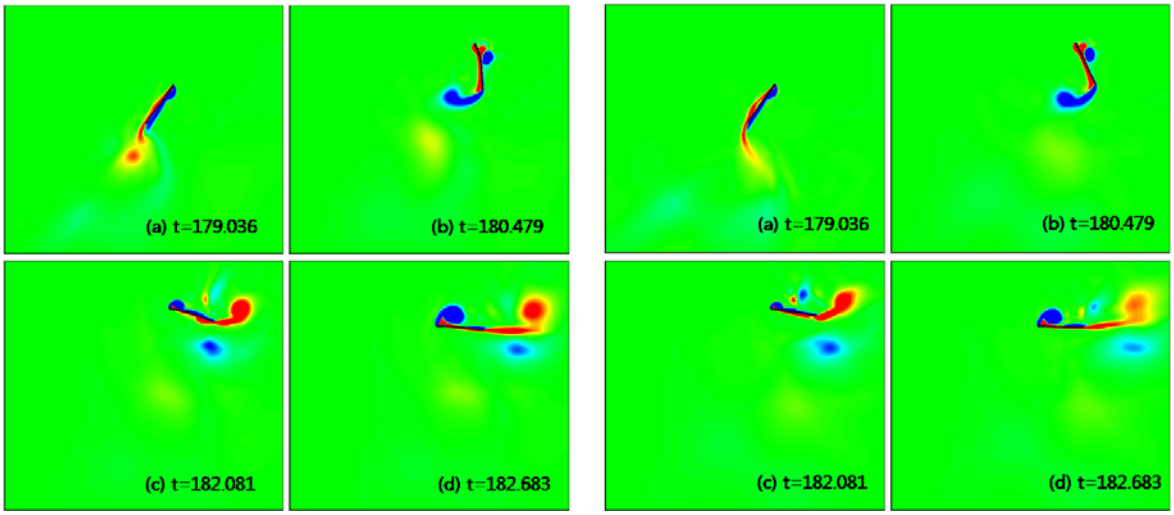

(i) flexible airfoil **(ii) rigid airfoil**

Figure 3.9 Vorticity contours during upstroke (a) t = 179.036, (b) t = 180.479, (c) t = 182.081, and (d) t = 182.683.

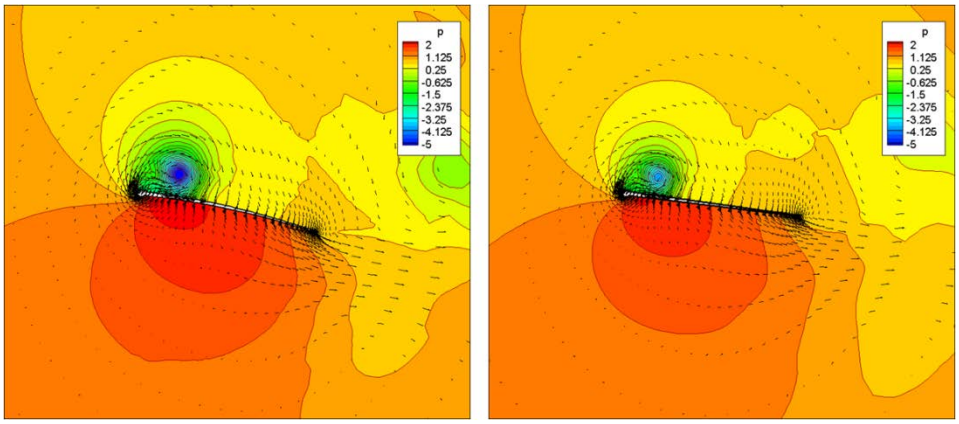

(i) flexible airfoil **(ii) rigid airfoil**

Figure 3.10 Leading-edge vortex at t = 162.608.

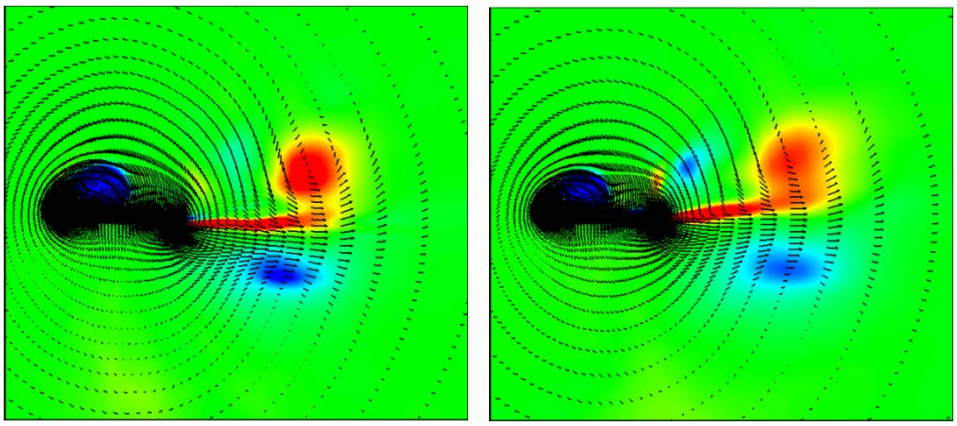

(i) flexible airfoil **(ii) rigid airfoil**

Figure 3.11 Vortex pairing and a jet flow in the wake at t = 162.608.

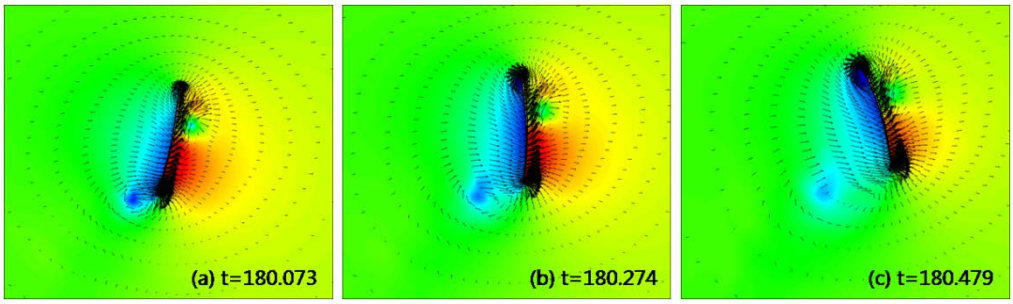

(i) flexible airfoil

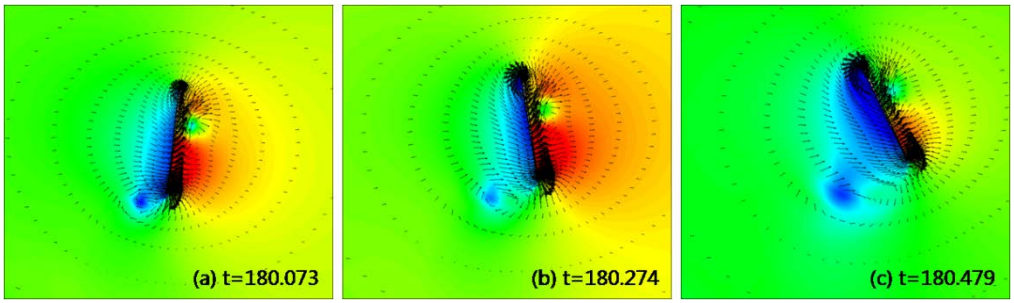

(ii) rigid airfoil

Figure 3.12 Vortex staying (a) t = 180.073, (b) t = 180.274, and (c) t = 180.479.

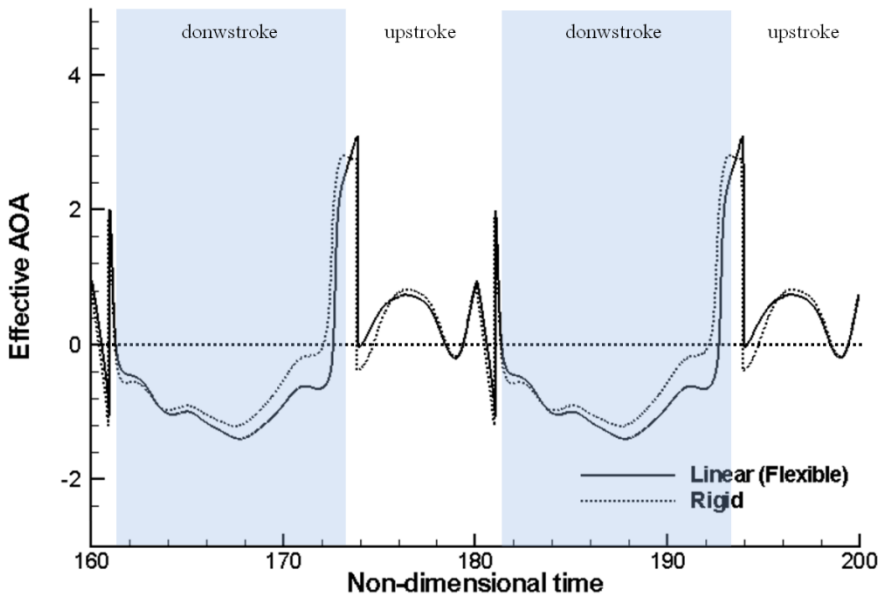

Figure 3.13 Histories of effective angle of attack.

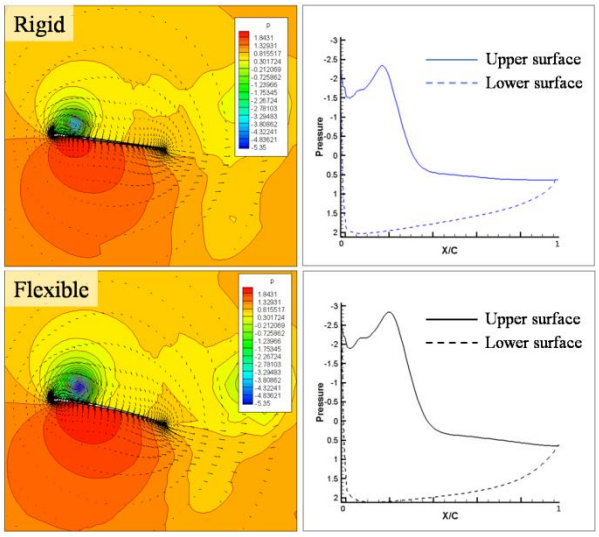
Rigid
Flexible
Upper surface
Lower surface
Pressure
X/C

(a)

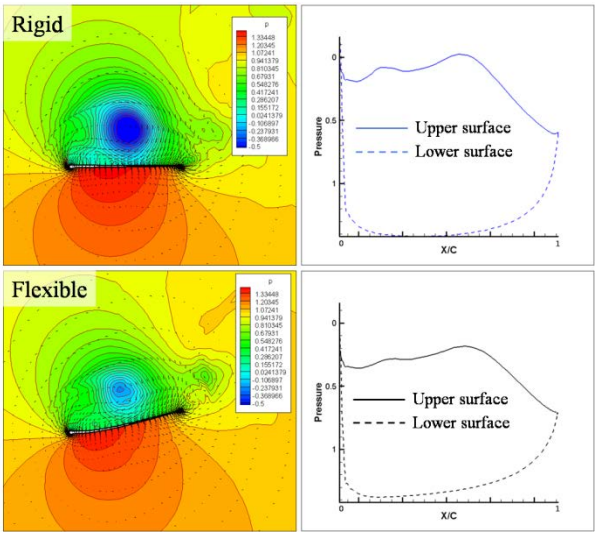
Rigid
Flexible
Upper surface
Lower surface
Pressure
X/C

(b)

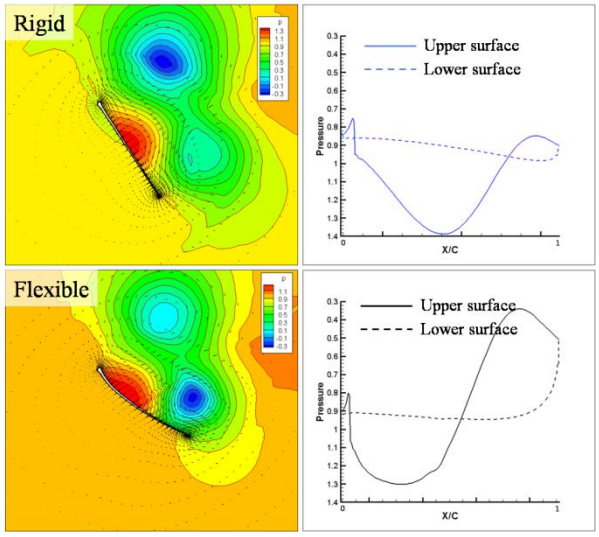
Rigid
Flexible
Upper surface
Lower surface
Pressure
X/C

(c)

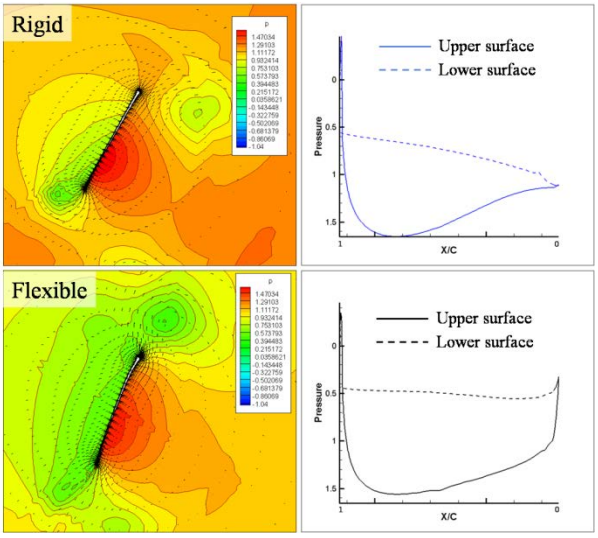
Rigid
Flexible
Upper surface
Lower surface
Pressure
X/C

(d)

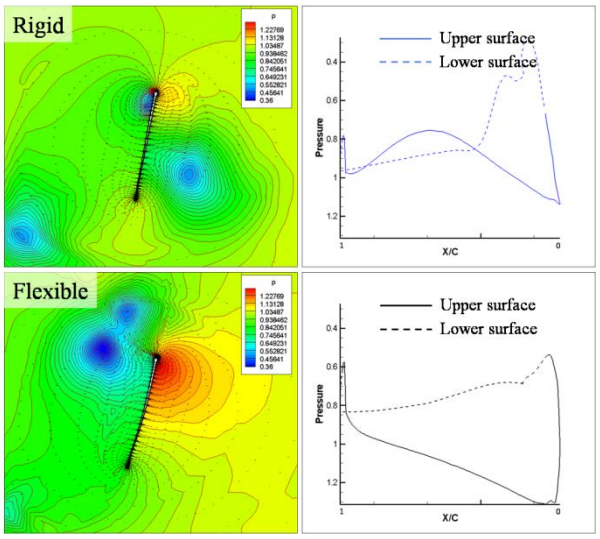

(e)

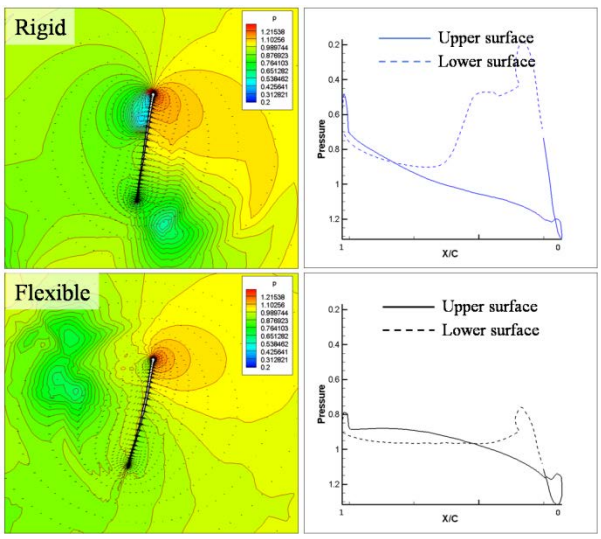

(f)

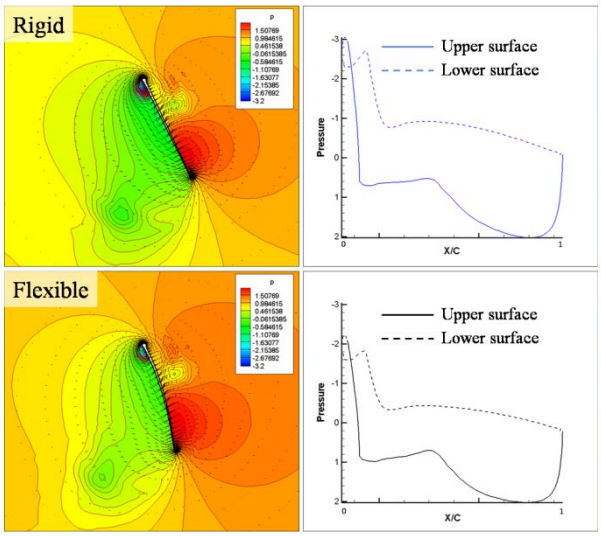

(g)

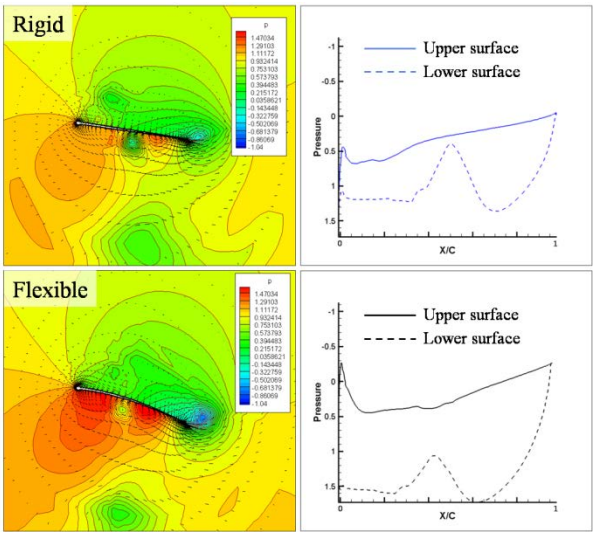

(h)

Figure 3.14 Pressure and velocity fields (left), pressure distribution on the wall (right) (a) t = 162.608, (b) t = 168.028, (c) t = 171.642, (d) t = 175.456, (e) t = 176.660, (f) t = 177.464, (g) t = 180.475, and (h) t = 181.604.

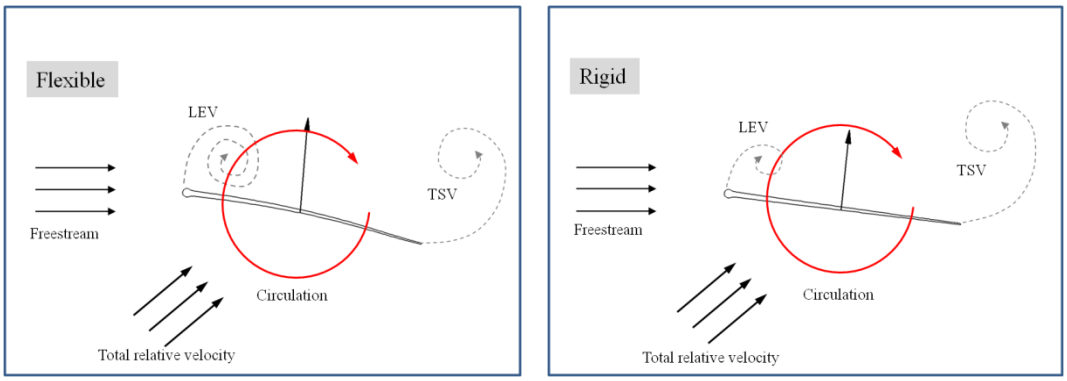
Flexible
LEV
TSV
Freestream
Circulation
Total relative velocity
Rigid
LEV
TSV
Freestream
Circulation
Total relative velocity

(a)

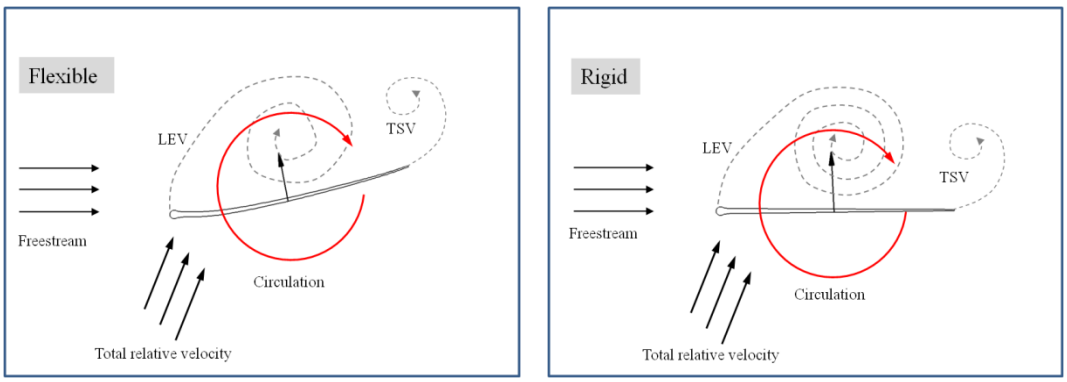
Flexible
LEV
TSV
Freestream
Circulation
Total relative velocity
Rigid
LEV
TSV
Freestream
Circulation
Total relative velocity

(b)

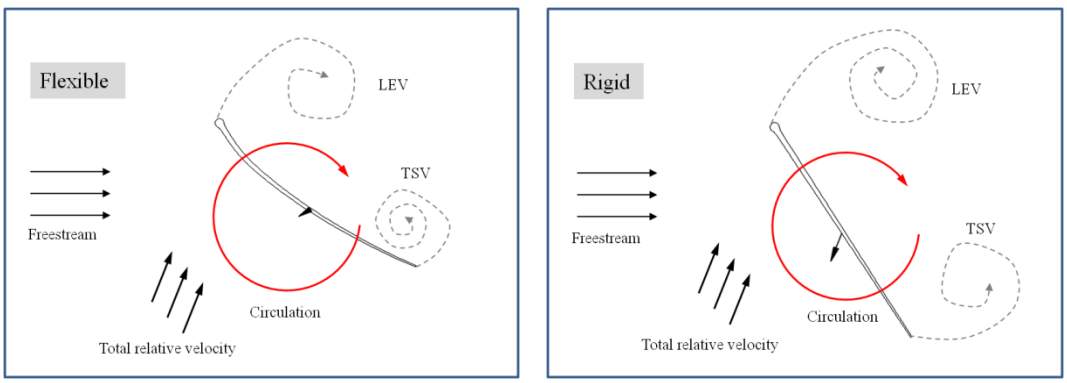
Flexible
LEV
TSV
Freestream
Circulation
Total relative velocity
Rigid
LEV
TSV
Freestream
Circulation
Total relative velocity

(c)

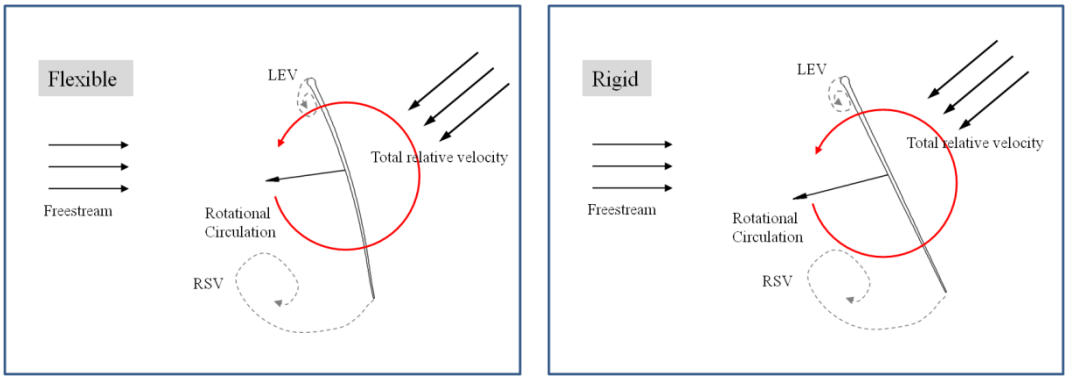

(d)

Figure 3.15 Schematic summary of net force generation (a) t = 162.608, (b) t = 168.028, (c) t = 171.642, and (d) t = 180.475.

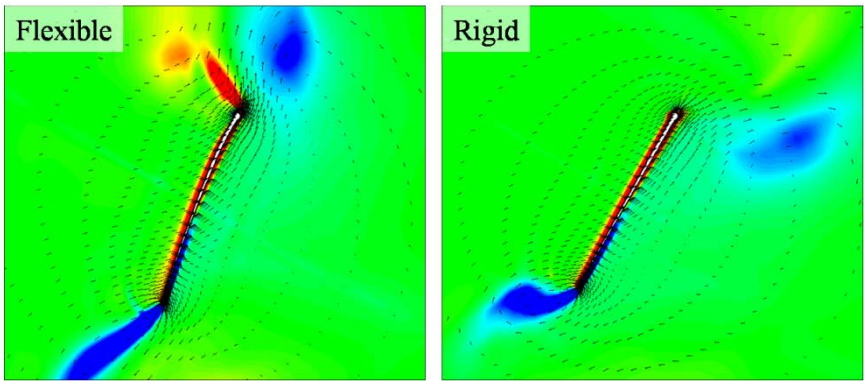

(a)

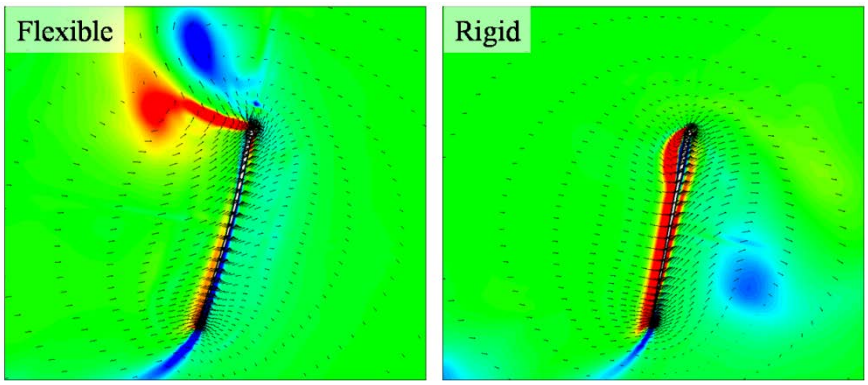

(b)

Figure 3.16 Vorticity contour and velocity fields (a) t = 175.456 and (b) t = 176.660.

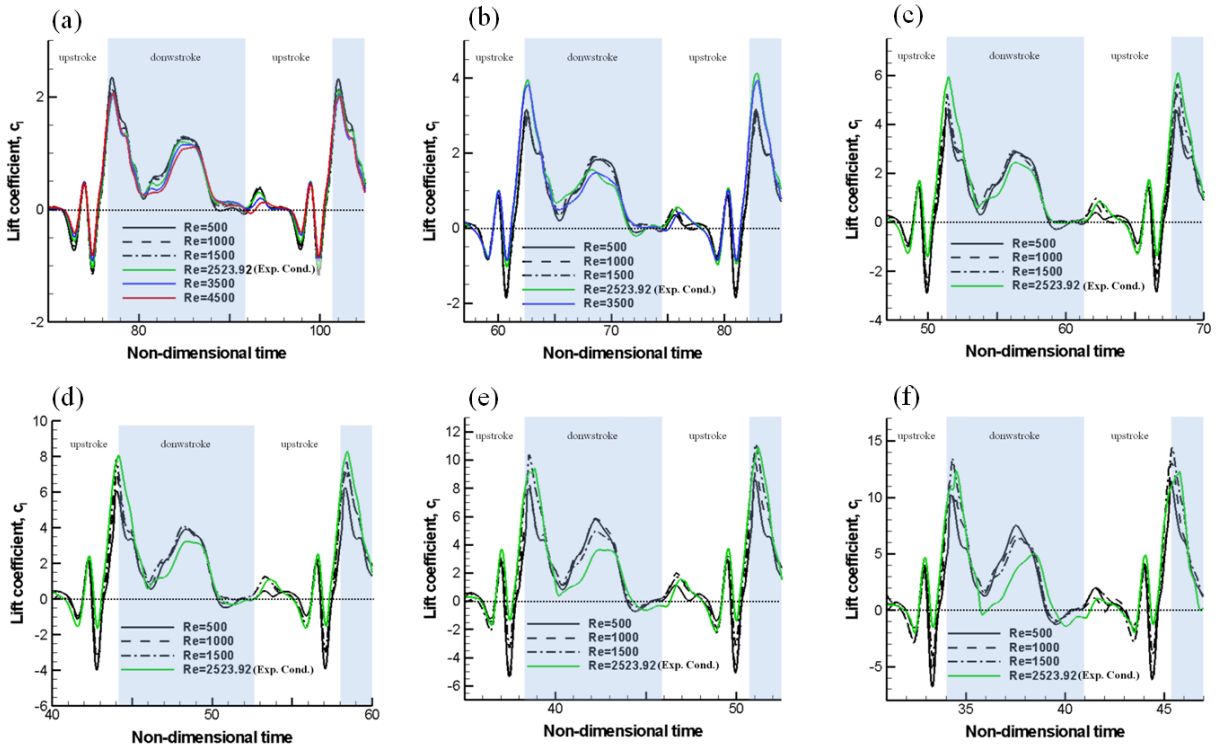

Figure 3.17 Histories of lift coefficients under various flight conditions (a) k = 0.04, (b) k = 0.049813(experimental condition), (c) k = 0.06, (d) k = 0.07, (e) k = 0.08, and (f) k = 0.09.

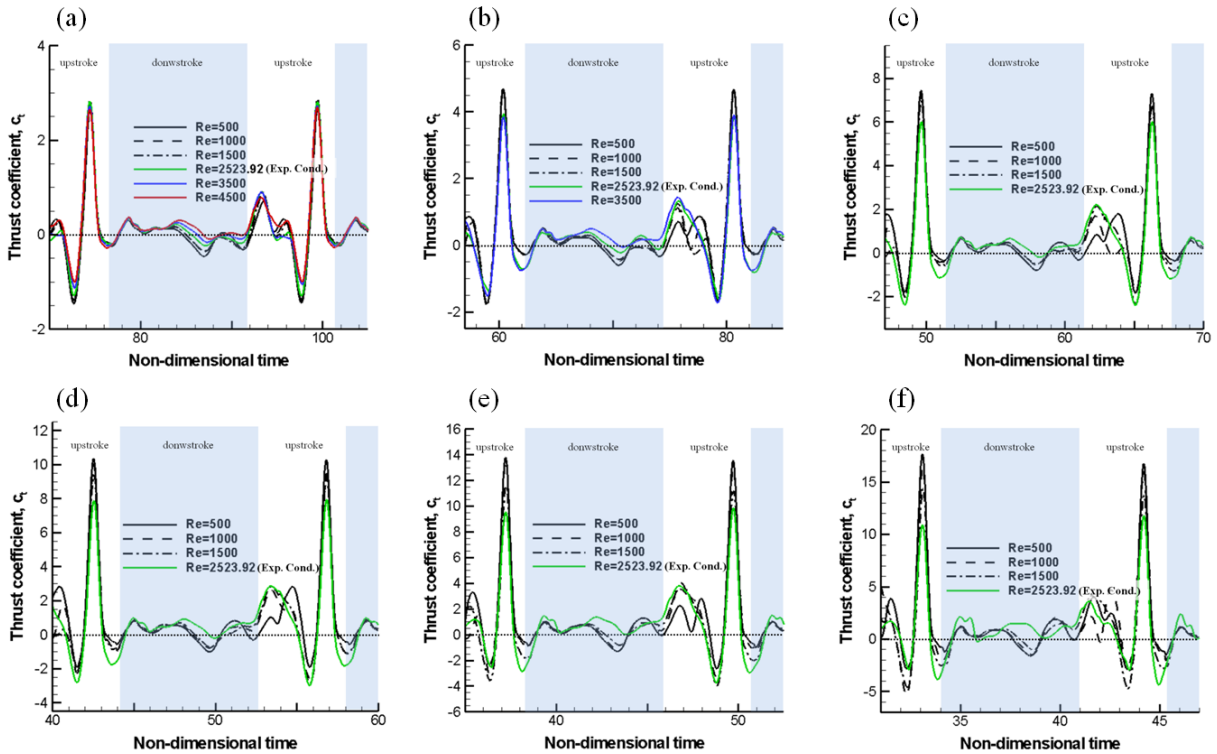

Figure 3.18 Histories of thrust coefficients under various flight conditions (a) k = 0.04, (b) k = 0.049813(experimental condition), (c) k = 0.06, (d) k = 0.07, (e) k = 0.08, and (f) k = 0.09.

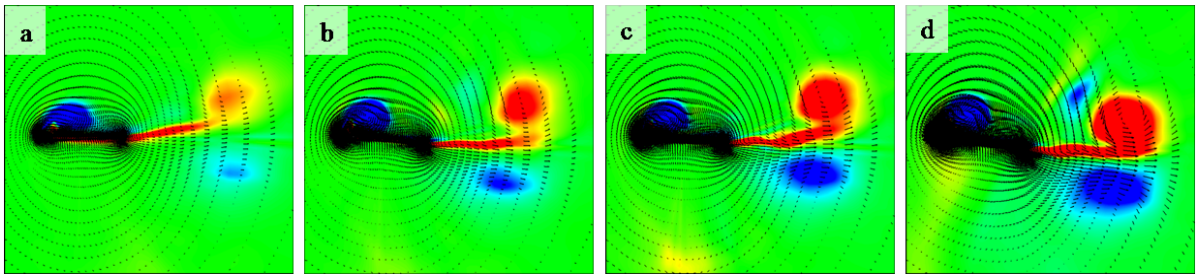

Figure 3.19 Vortex pairing (a) *Re* = 2523.92, *k* = 0.04, (b) *Re* = 2523.92, *k* = 0.049813 (experimental condition), (c) *Re* = 2523.92, *k* = 0.07, and (d) *Re* = 2523.92, *k* = 0.09.

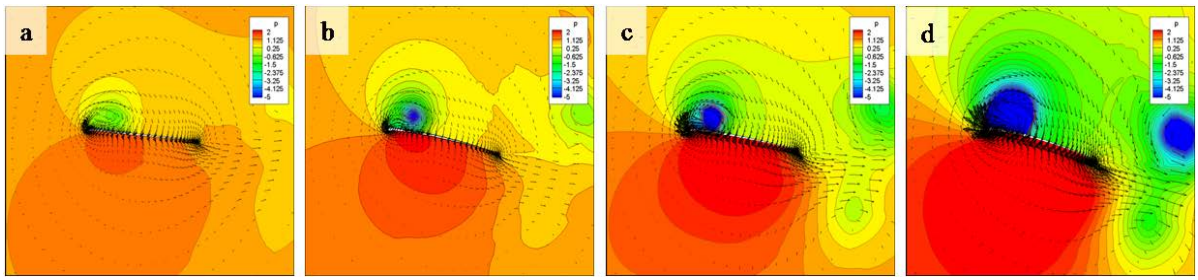

Figure 3.20 Leading-edge vortex (a) *Re* = 2523.92, *k* = 0.04, (b) *Re* = 2523.92, *k* = 0.049813 (experimental condition), (c) *Re* = 2523.92, *k* = 0.07, and (d) *Re* = 2523.92, *k* = 0.09.

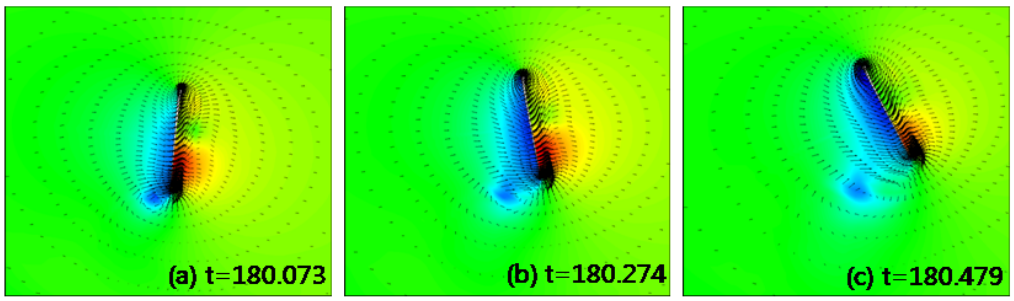

(i) *Re* = 2523.92, *k* = 0.04

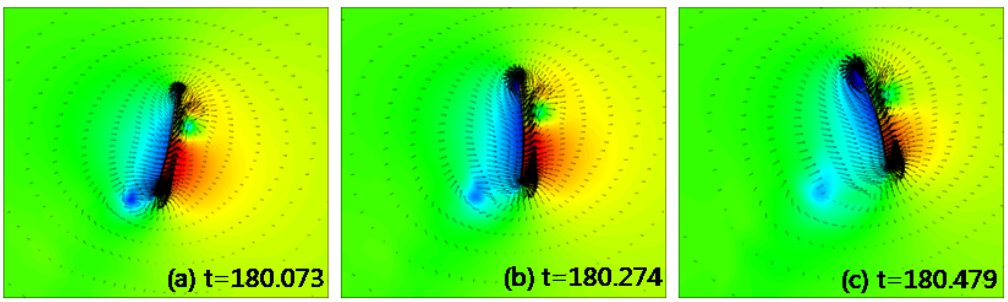

(ii) *Re* = 2523.92, *k* = 0.07

Figure 3.21 Vortex staying.

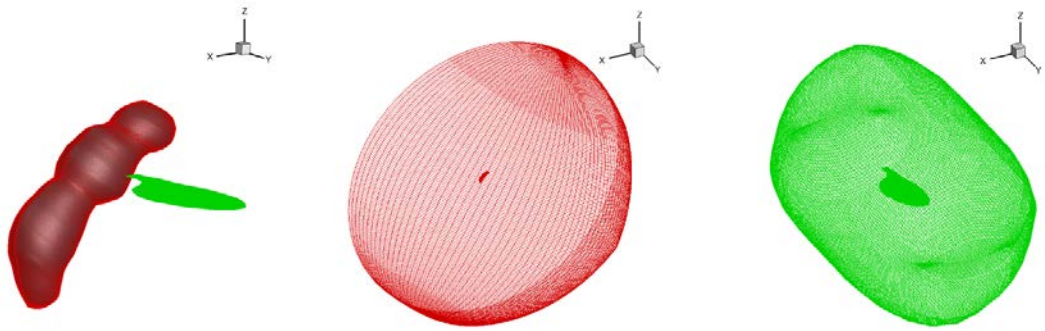

a)

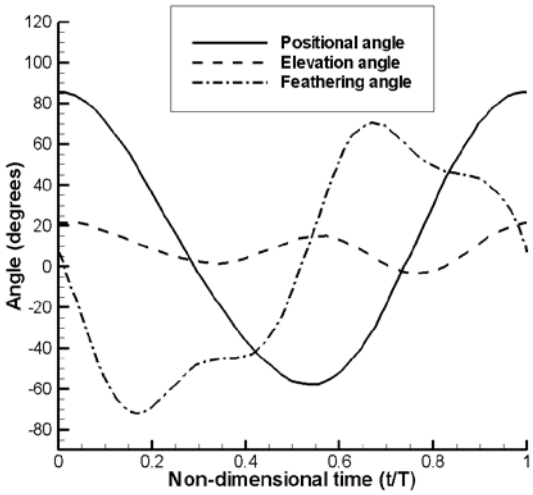

b)

Figure 4.1 Geometric and kinematic modeling of a fruit fly: a) two-block and 5.2 million grid points of mesh system and b) flapping wing trajectory obtained from [21, 58].

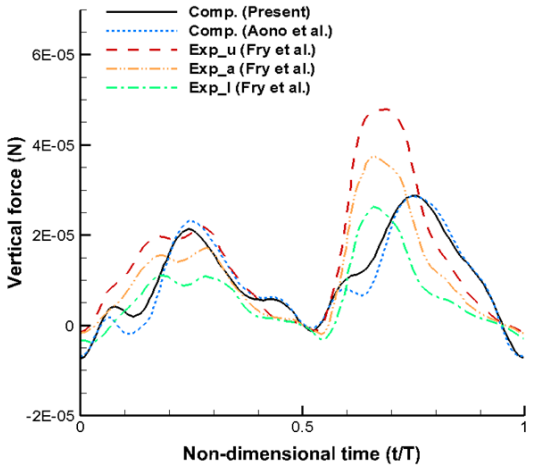

a)

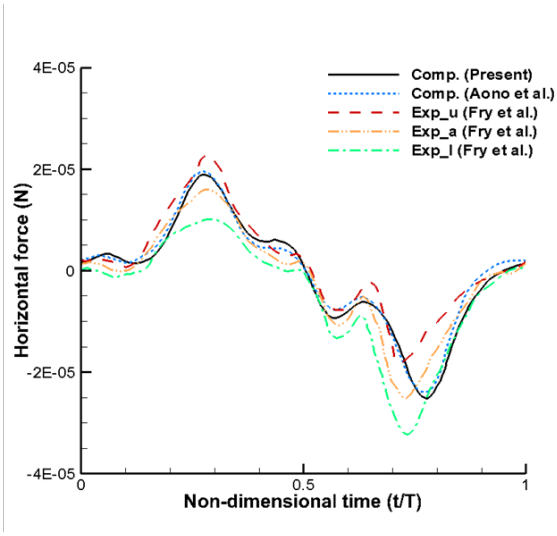

b)

Figure 4.2 Time histories of the a) vertical and b) horizontal forces: solid line, computed result (present); dotted line, computed result (Aono et al. [21]); dashed line, upper values of experiment (Exp_u, Fry et al. [31]); dash–dot–dot line, average values of experiment (Exp_a); and dash–dot line, lower values of experiment (Exp_l).

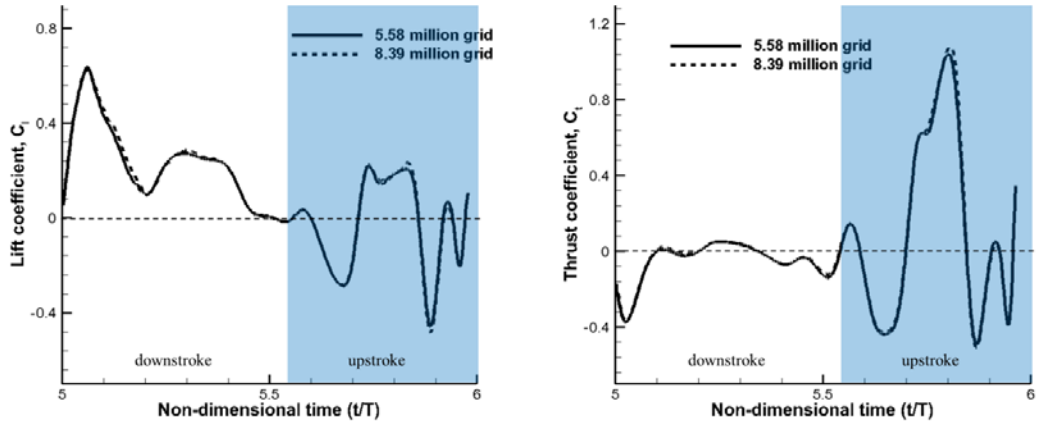

a) **b)**

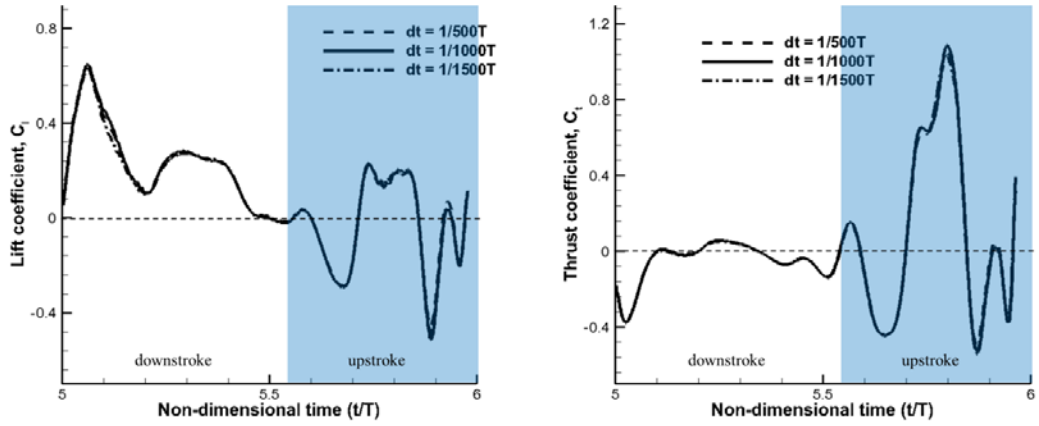

c) **d)**

Figure 4.3 Grid refinement and time step sensitivity: a-b) grid refinement test with two sets of mesh system and c-d) time sensitivity test using three time steps.

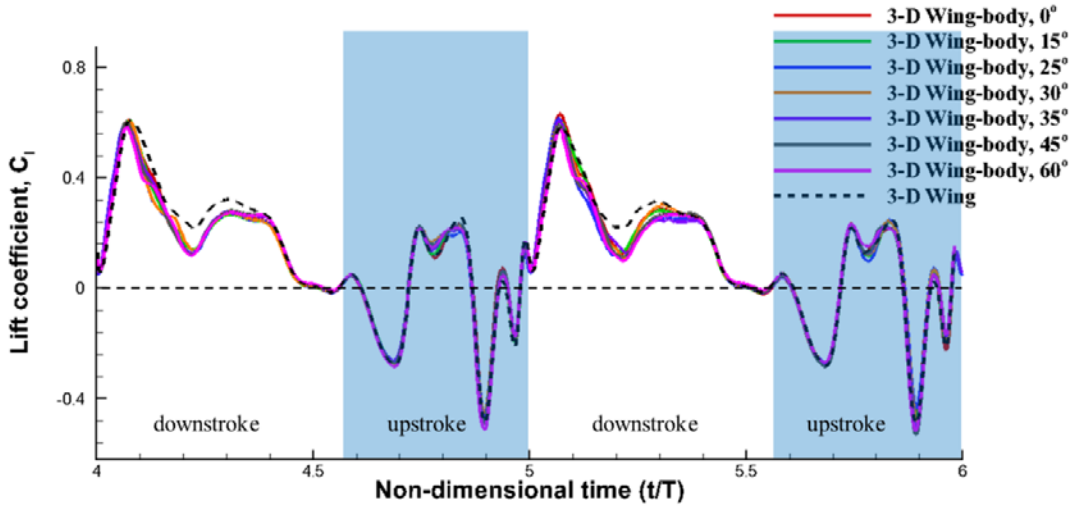

a)

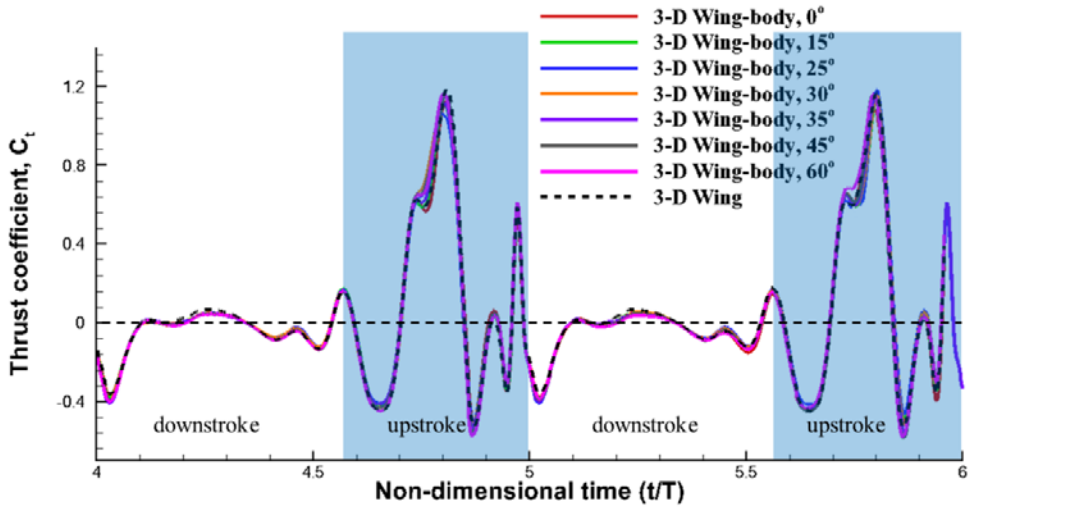

b)

Figure 4.4 Time histories of instantaneous a) lift and b) thrust coefficients in 3-D wing-body simulation at various body AOA.

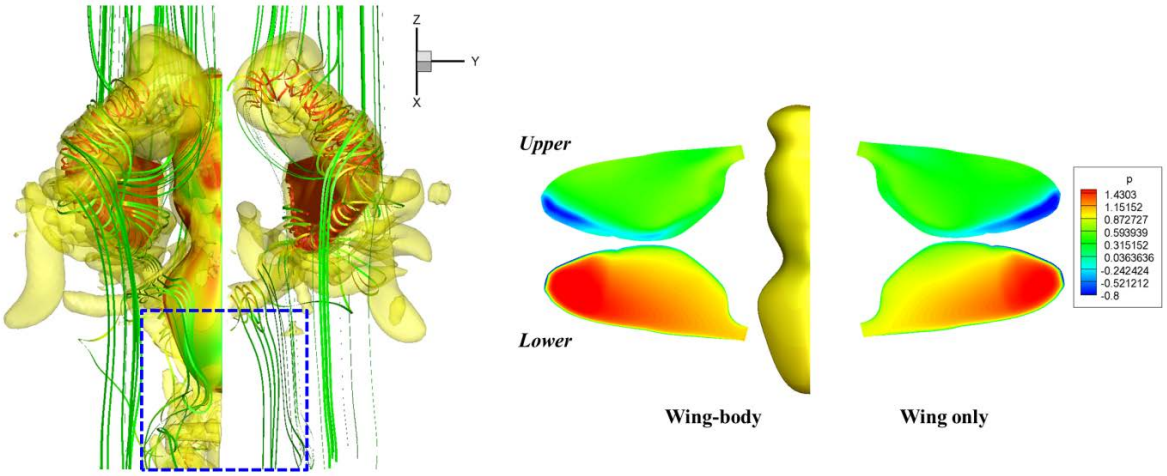

a) **b)**

Figure 4.5 Comparison of a) vorticity and b) surface pressure between wing-body and wing only case at the end of upstroke.

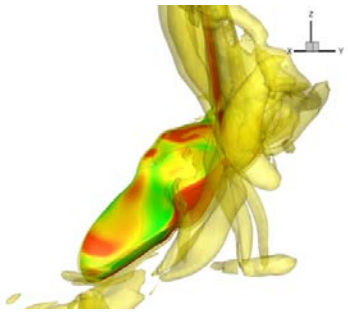

a)

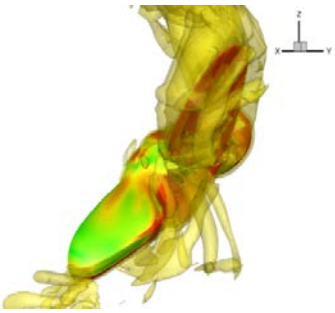

b)

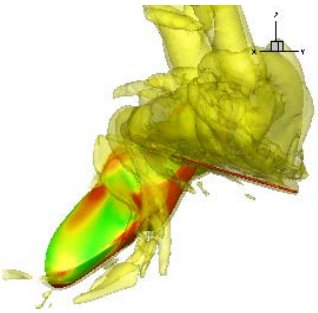

c)

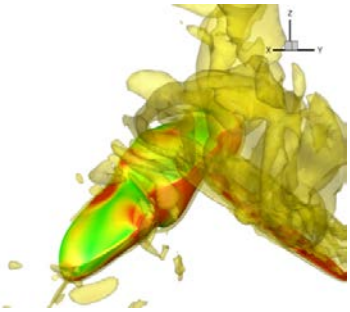

d)

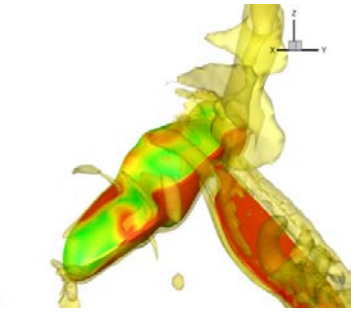

e)

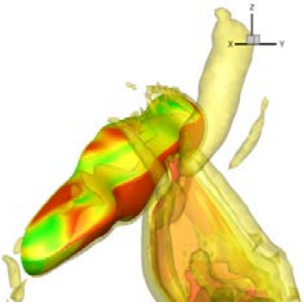

f)

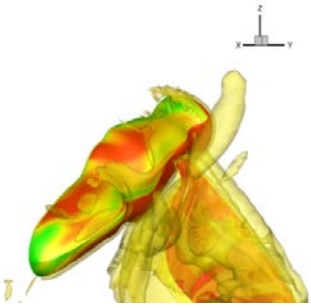

g)

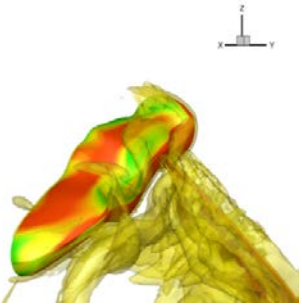

h)

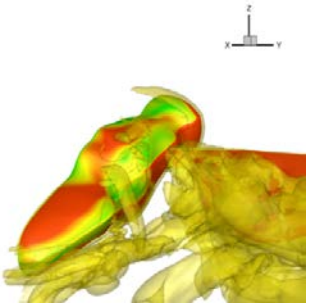

i)

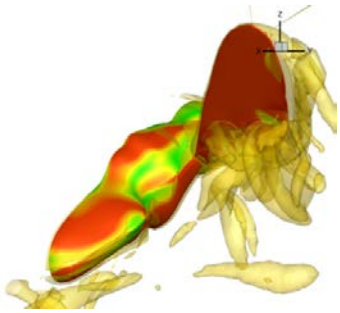

j)

Figure 4.6 Snapshots of vorticity contours during a flapping motion: a) $t = 5.0T$, b) $t = 5.1T$, c) $t = 5.2T$, d) $t = 5.3T$, e) $t = 5.4T$, f) $t = 5.5T$, g) $t = 5.6T$, h) $t = 5.7T$, i) $t = 5.8T$, and j) $t = 5.9T$.

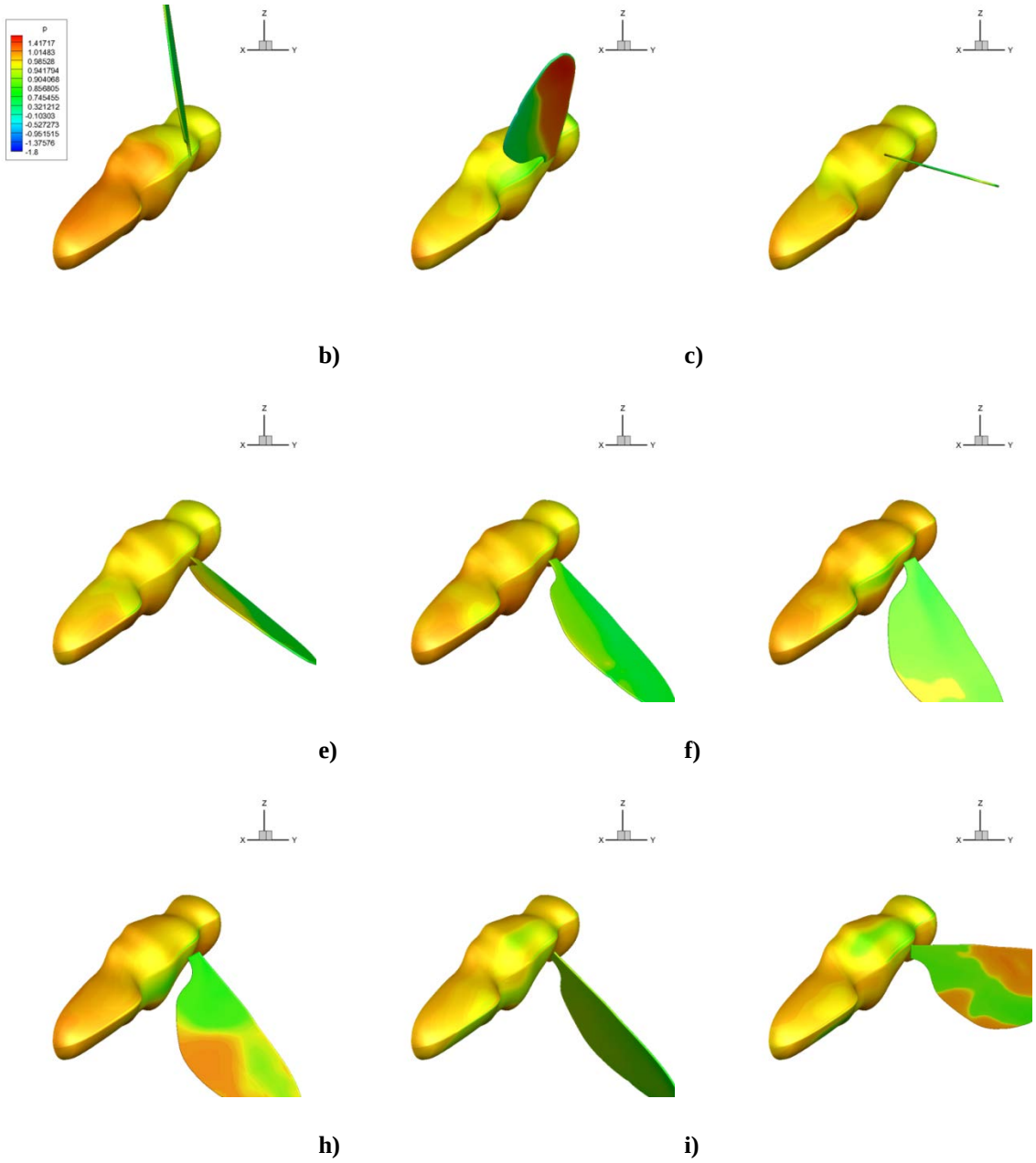
p
1.41717
1.01483
0.98528
0.941794
0.904068
0.856805
0.745455
0.321212
-0.10303
-0.527273
-0.561515
-1.37576
-1.8
Z
X
Y

a) **b)** **c)**

d) **e)** **f)**

g) **h)** **i)**

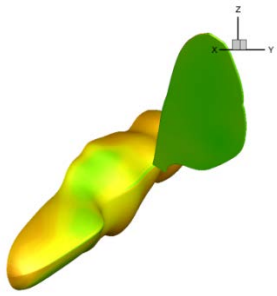

j)

Figure 4.7 Snapshots of pressure distributions during a flapping motion: a) $t = 5.0T$, b) $t = 5.1T$, c) $t = 5.2T$, d) $t = 5.3T$, e) $t = 5.4T$, f) $t = 5.5T$, g) $t = 5.6T$, h) $t = 5.7T$, i) $t = 5.8T$, and j) $t = 5.9T$.

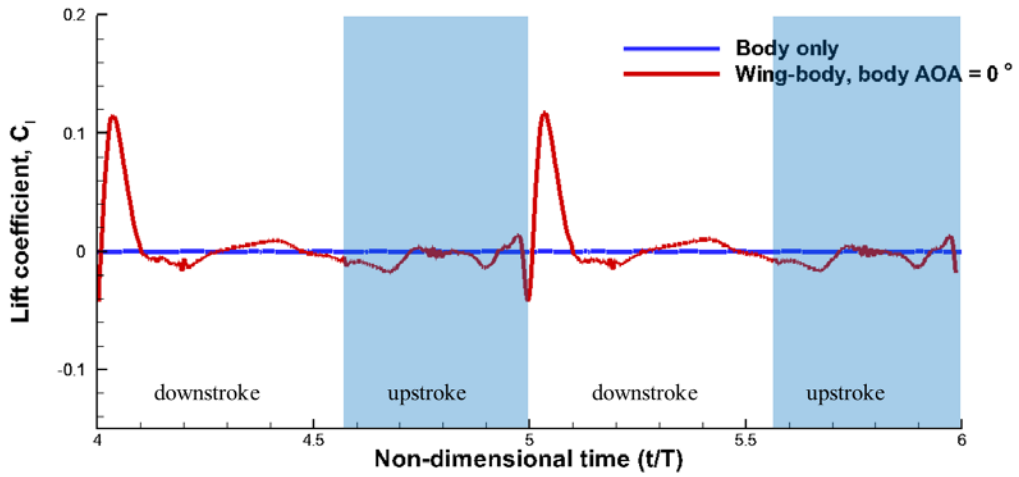

a)

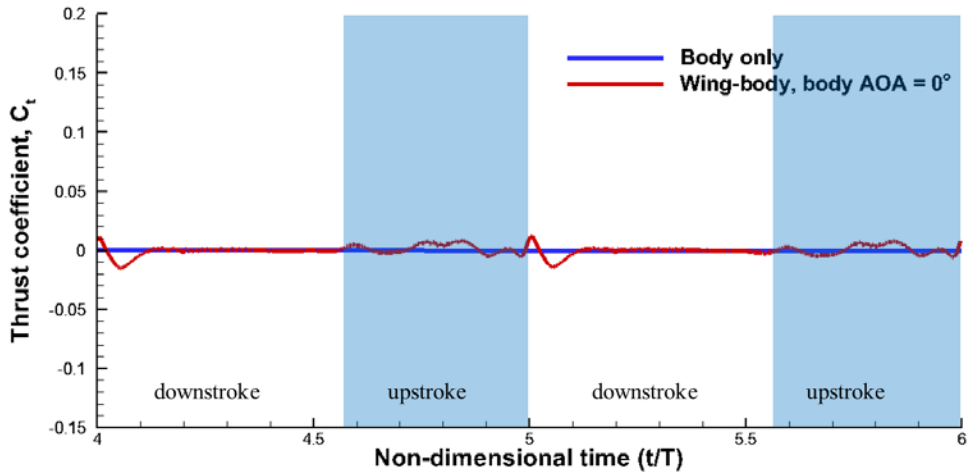

b)

Figure 4.8 Time histories of instantaneous a) lift and b) thrust coefficients on the body with and without wing.

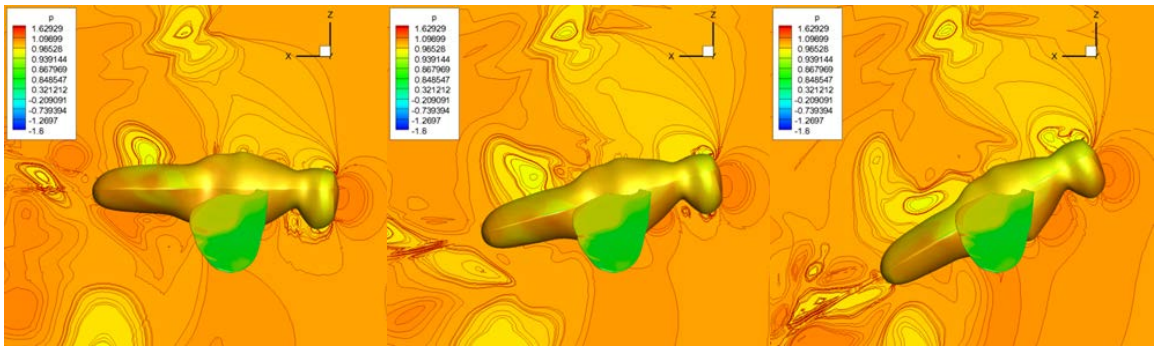

a) **b)** **c)**

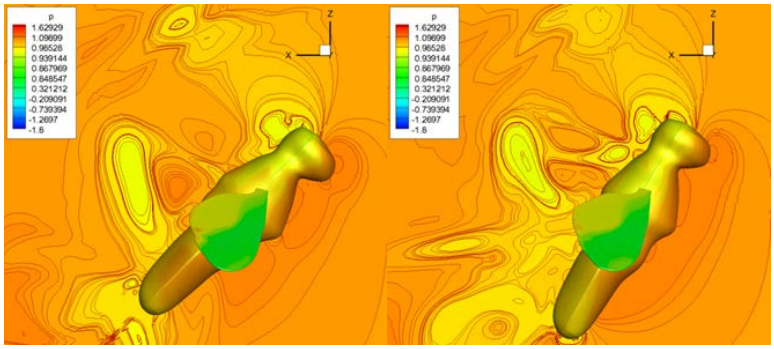

d) **e)**

Figure 4.9 Cross-sectional pressure distributions at the symmetric boundary at the middle of down-stroke: a) 0^o, b) 15^o, c) 30^o, d) 45^o, and e) 60^o.

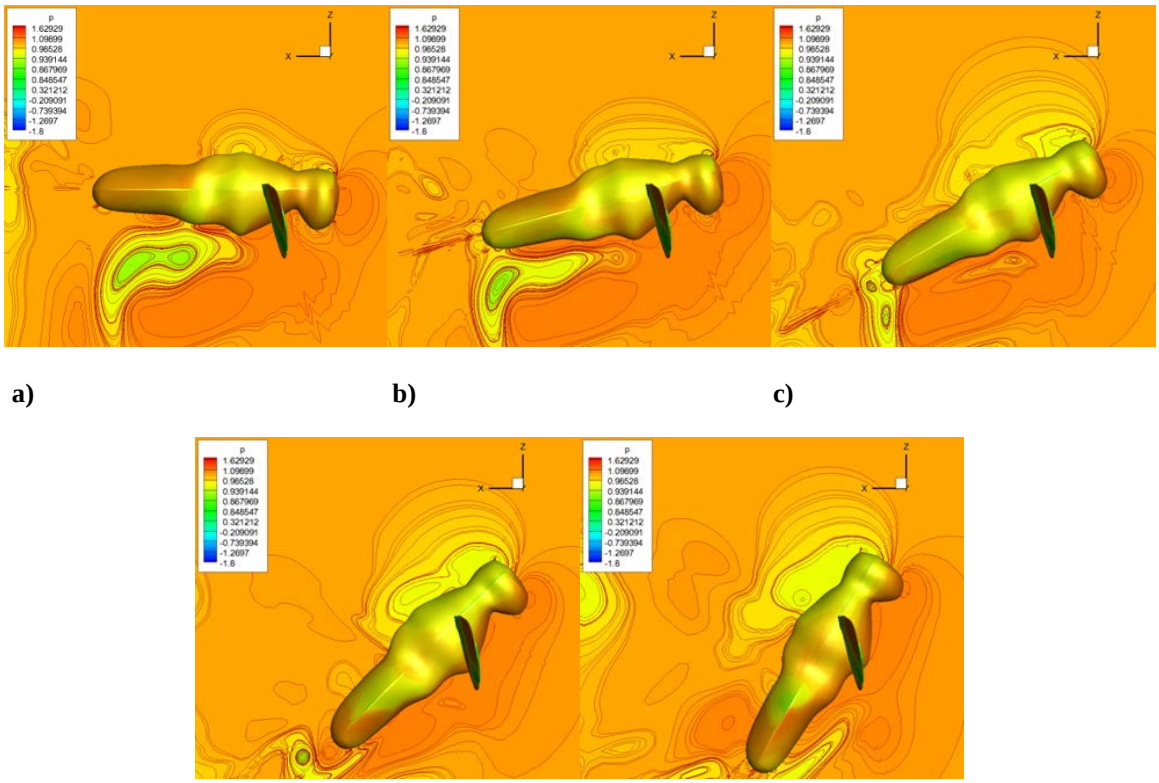

a) **b)** **c)**

d) **e)**

Figure 4.10 Cross-sectional pressure distributions at the symmetric boundary at the middle of up-stroke: a) 0^o, b) 15^o, c) 30^o, d) 45^o, and e) 60^o.

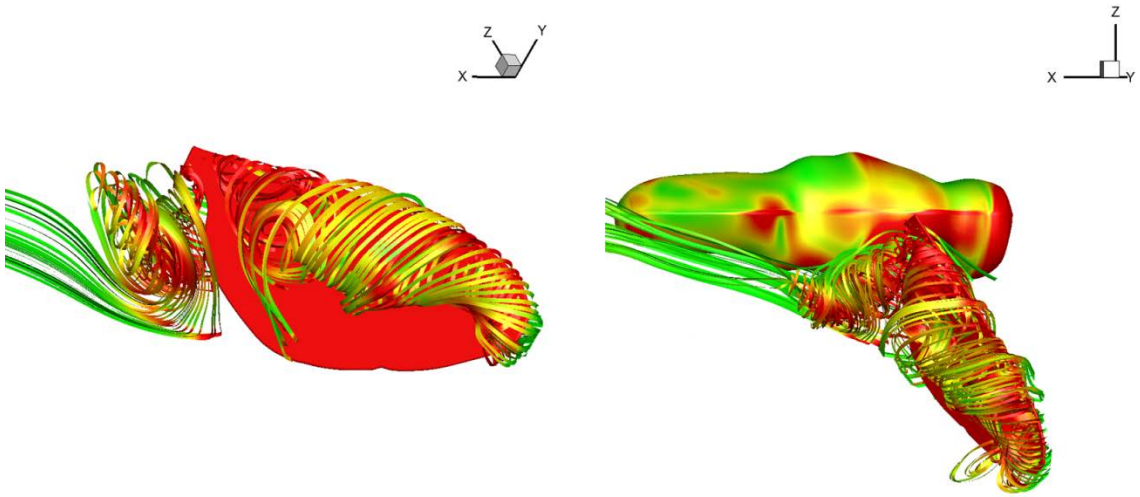

a) **b)**

Figure 4.11 Extended perfect vortex tube: a) wing only and b) wing-body case.

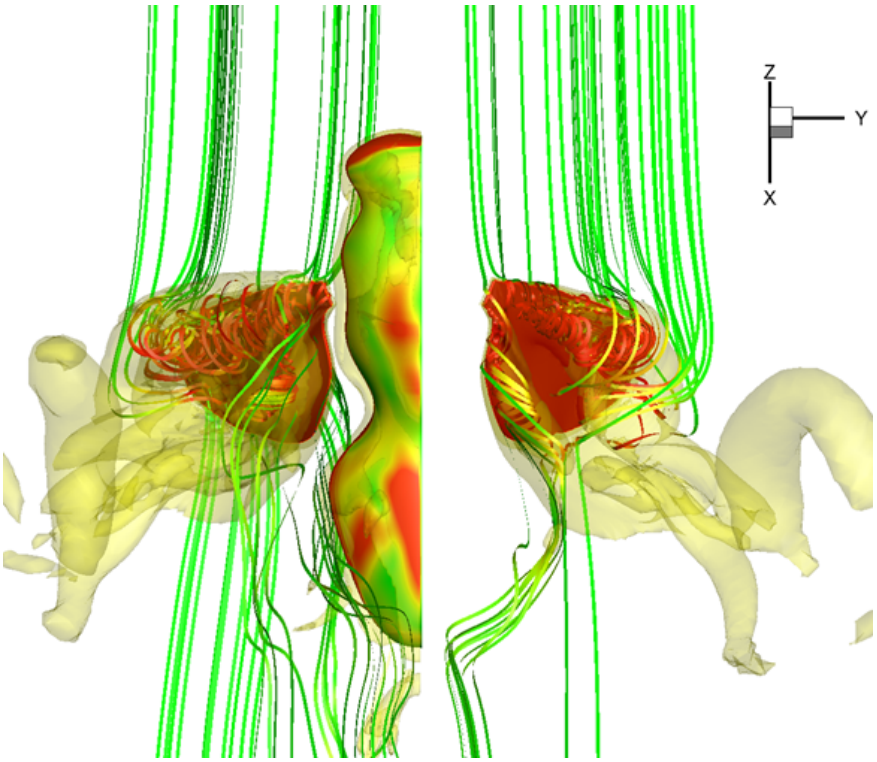

a) **b)**

Figure 4.12 Comparison of the LEV in a) wing-body and b) wing only case.

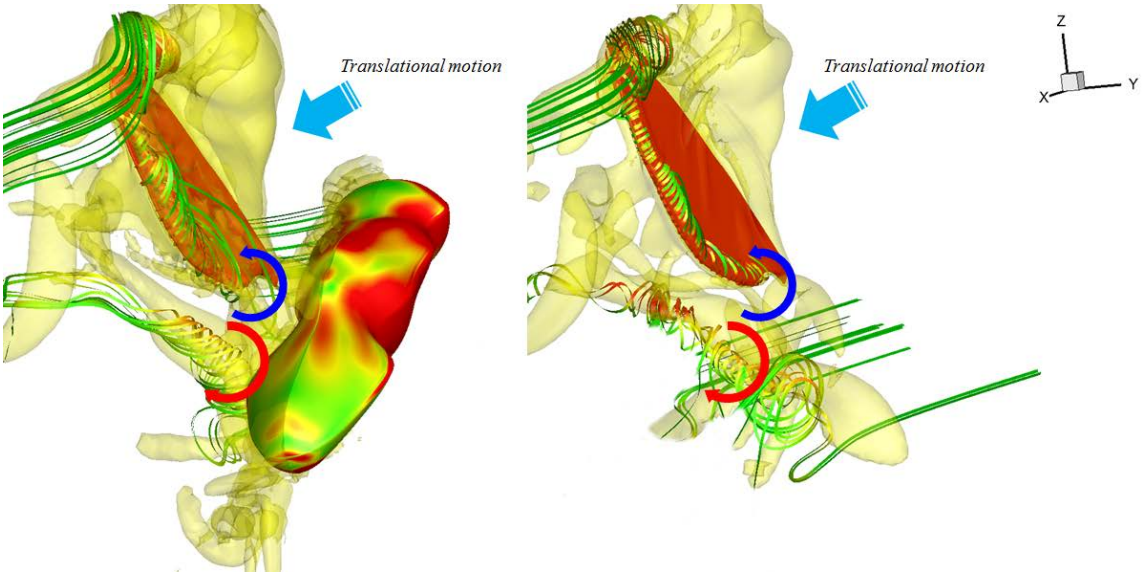

a) **b)**

Figure 4.13 Comparison of the vortex pairing phenomenon in a) wing-body and b) wing only case.

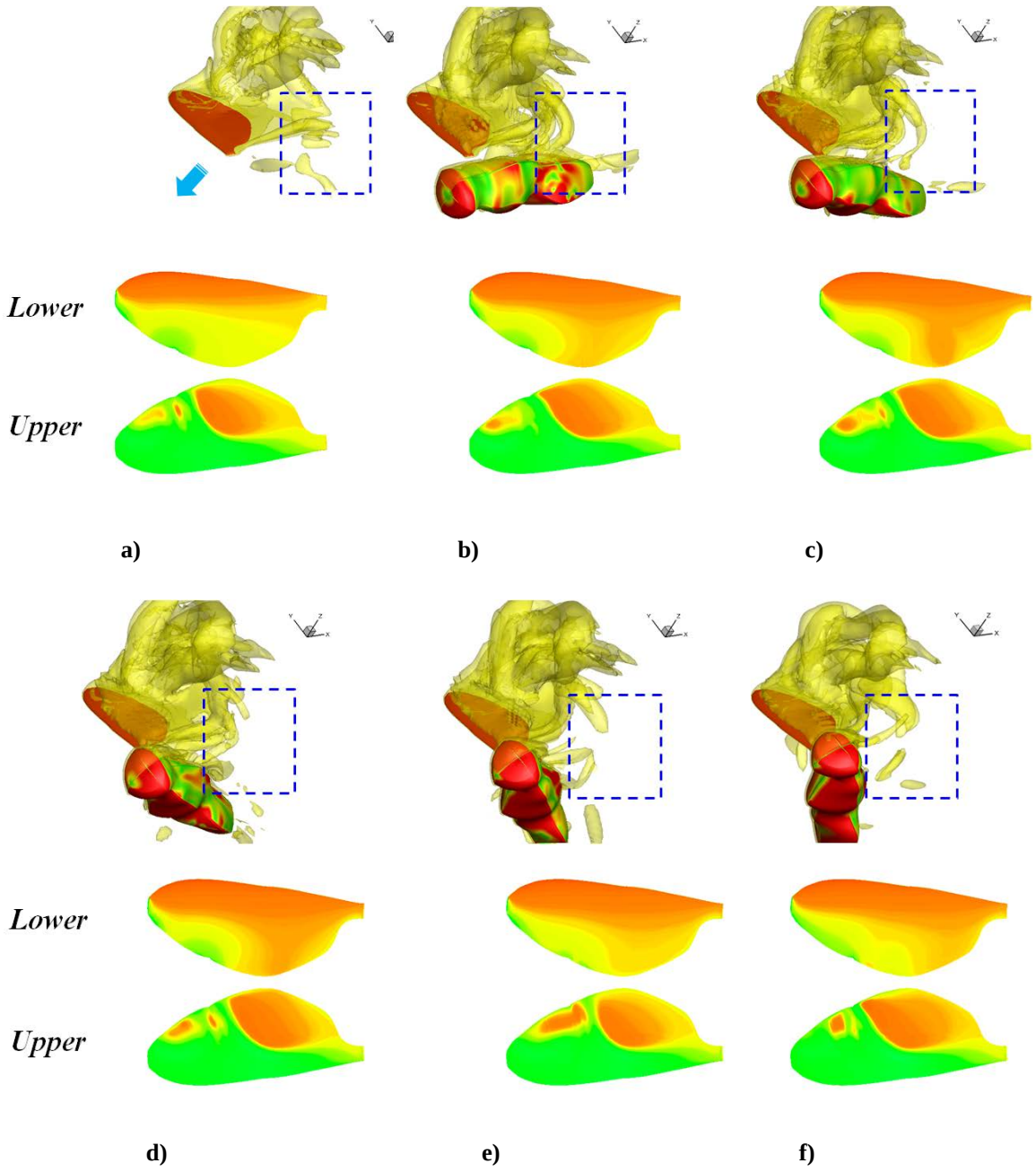

Figure 4.14 Vorticity (up) and surface pressure (down) at the middle of downstroke: a) wing only, b) 0^o, c) 15^o, d) 30^o, e) 45^o, and f) 60^o.

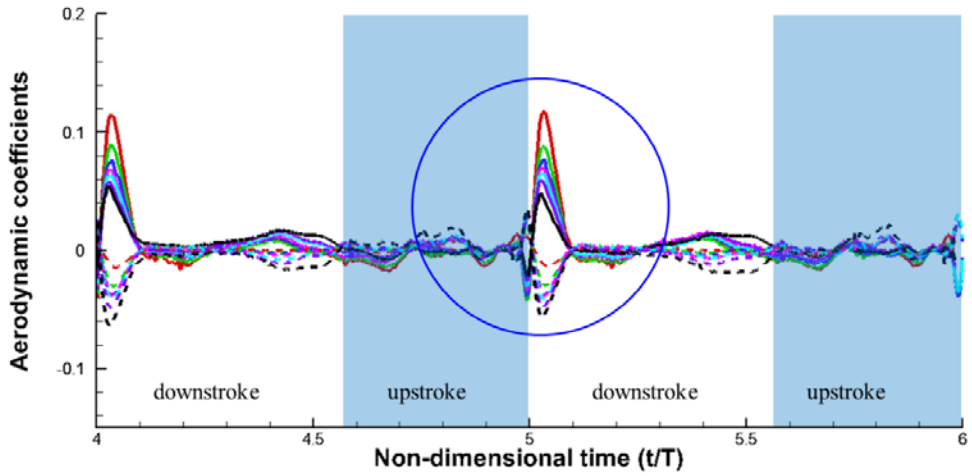

a)

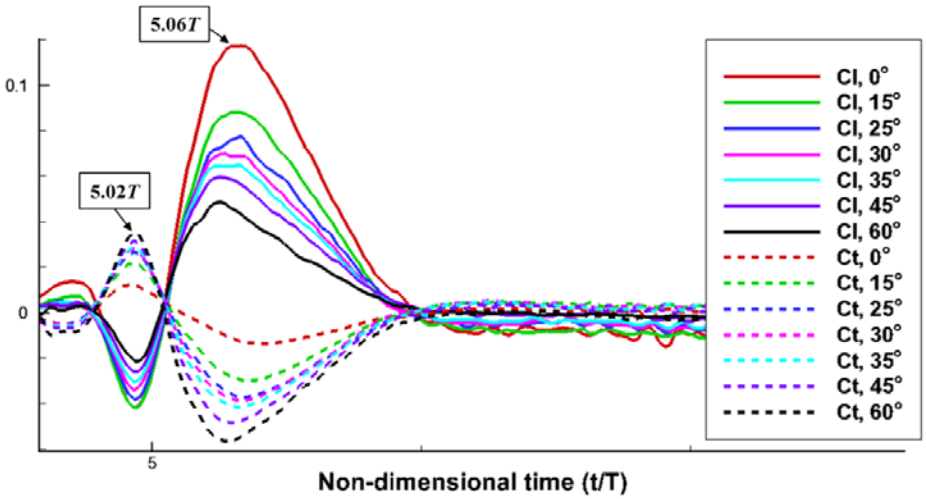

b)

Figure 4.15 Time histories of instantaneous aerodynamic coefficients on the body at various body AOA: a) lift (solid line) and thrust (dashed line) coefficients and b) close-up view of the circle in a).

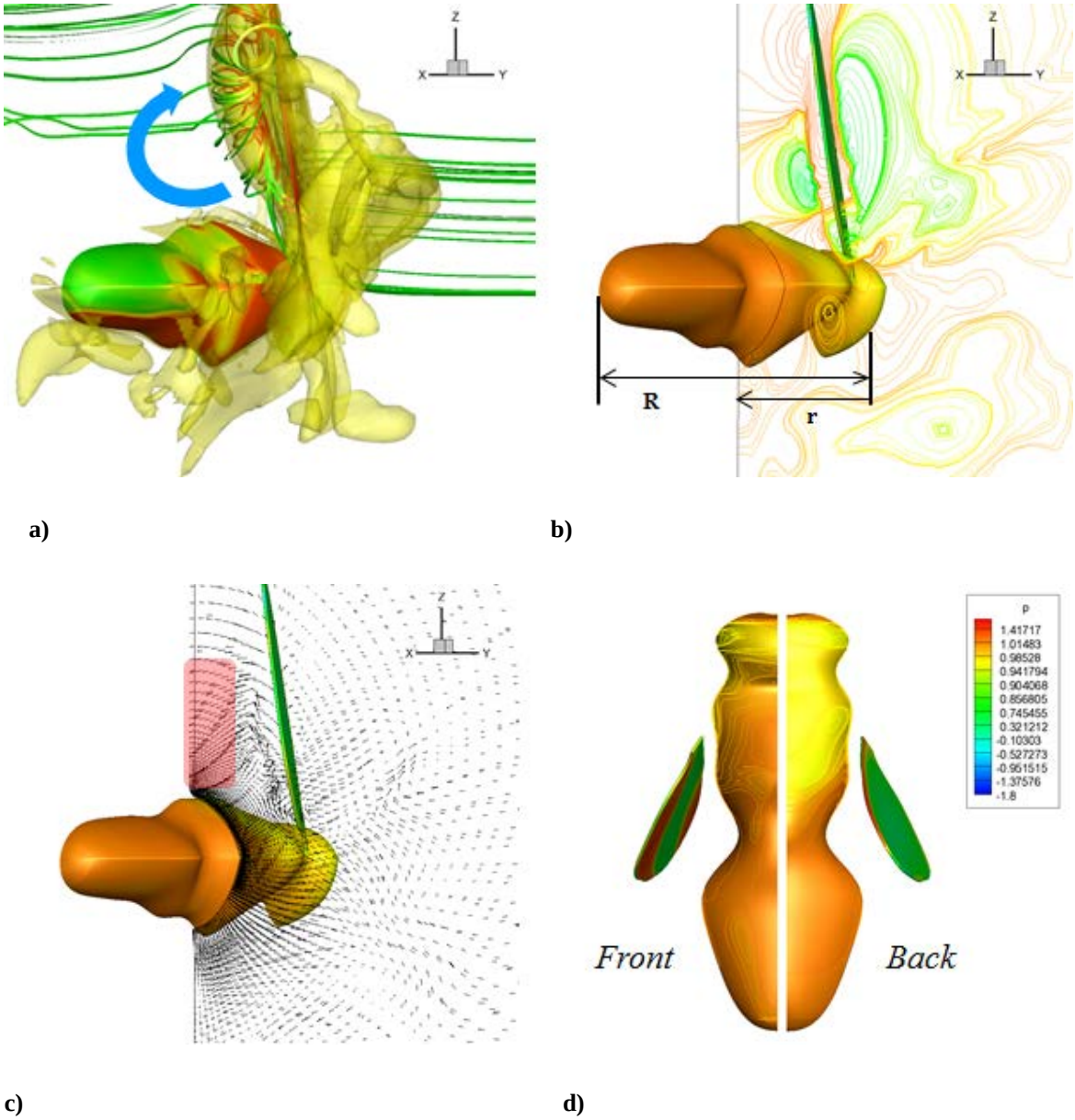

a) **b)**

c) **d)**

Figure 4.16 a) Vorticity, b) cross-sectional pressure field, c) velocity field, and d) surface pressure at time = 5.02*T*.

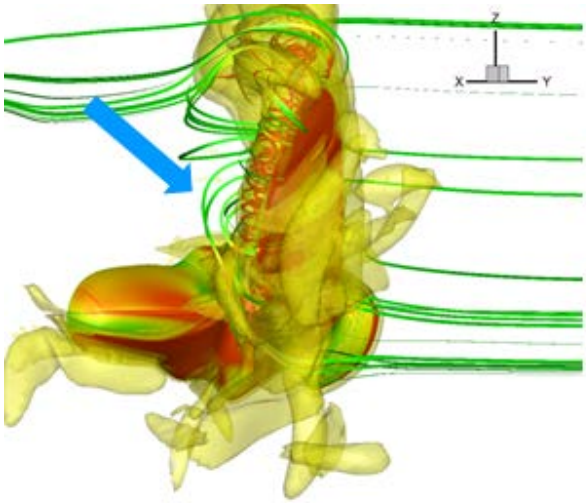

a)

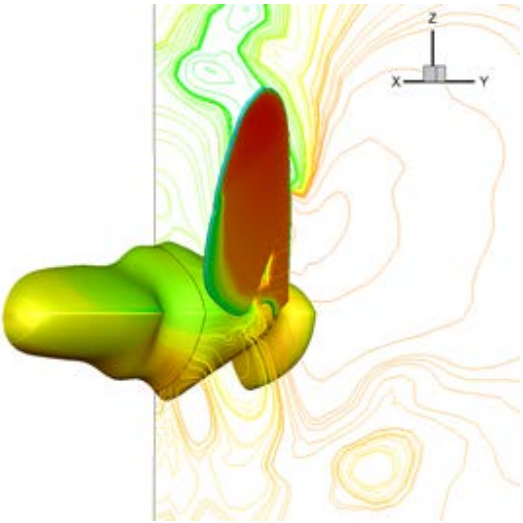

b)

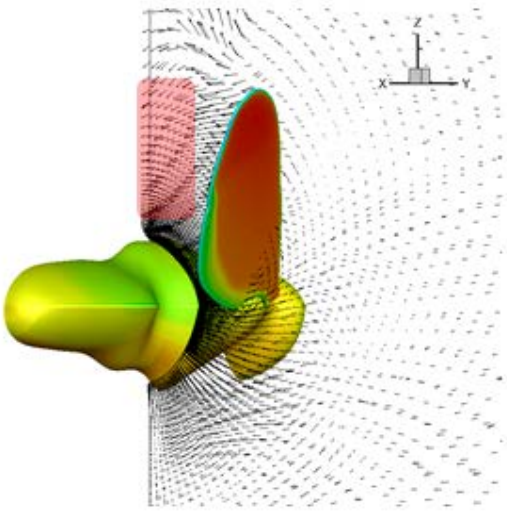

c)

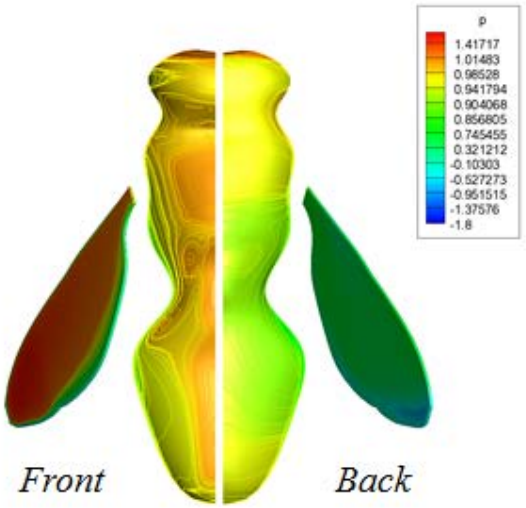

d)

Figure 4.17 a) Vorticity, b) cross-sectional pressure field, c) velocity field, and d) surface pressure at time = 5.06*T*.

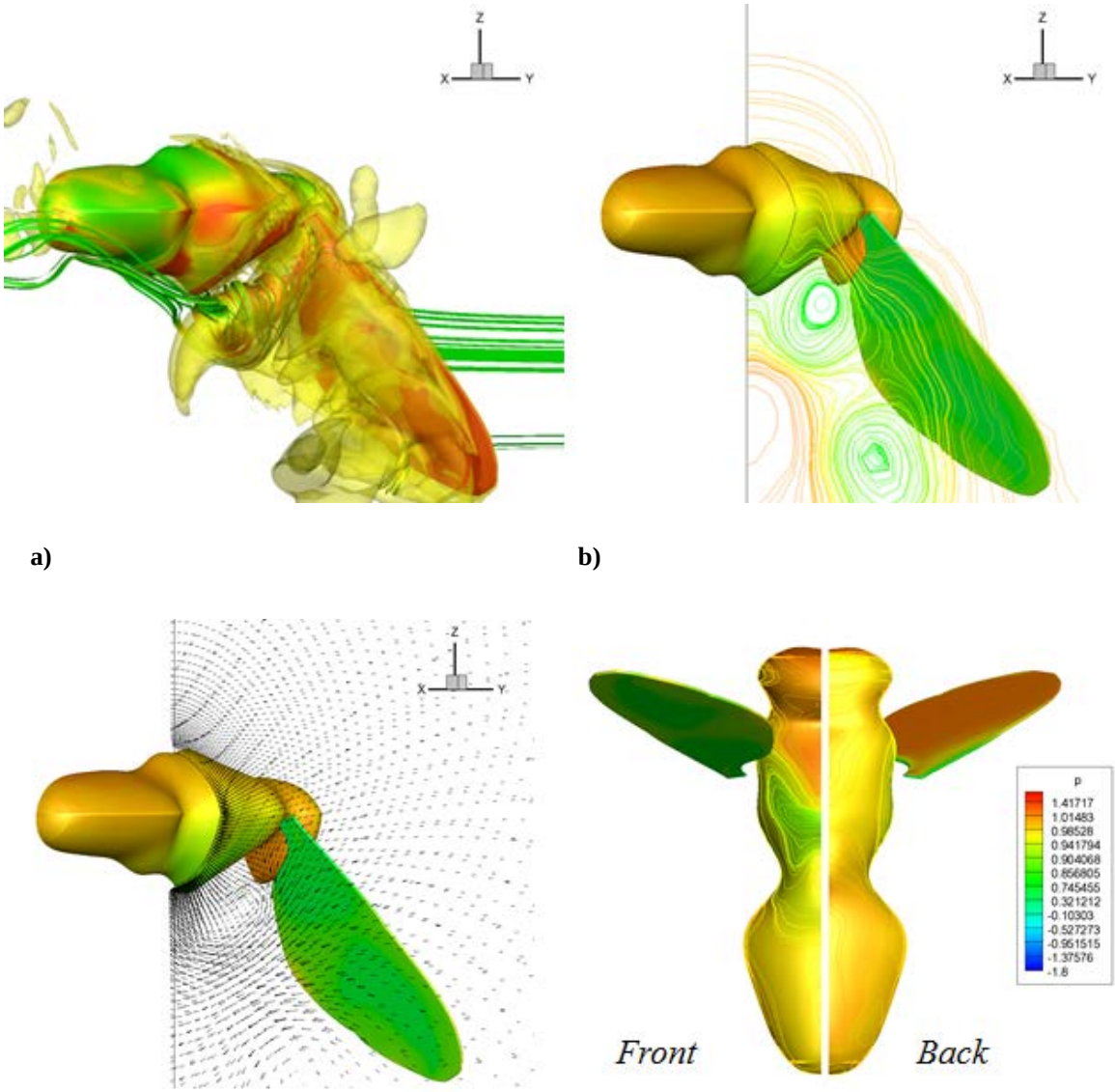

a) **b)**

c) **d)**

Figure 4.18 a) Vorticity, b) cross-sectional pressure field, c) velocity field, and d) surface pressure at time = 5.4*T*.

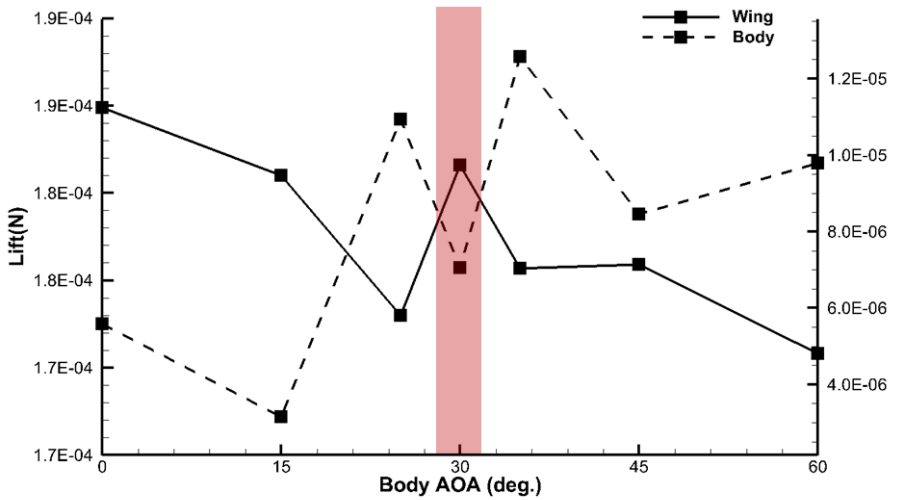

a)

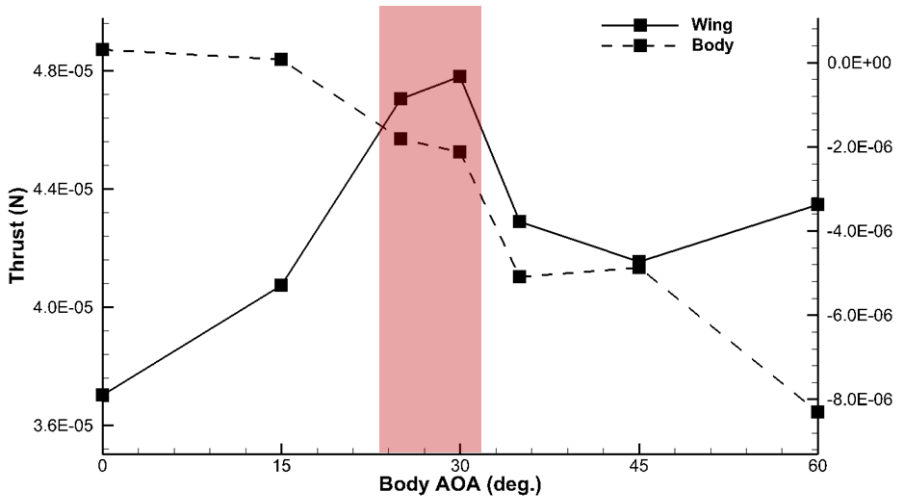

b)

Figure 4.19 a) Lift and b) thrust on the wing and body respectively, according to the body AOA.

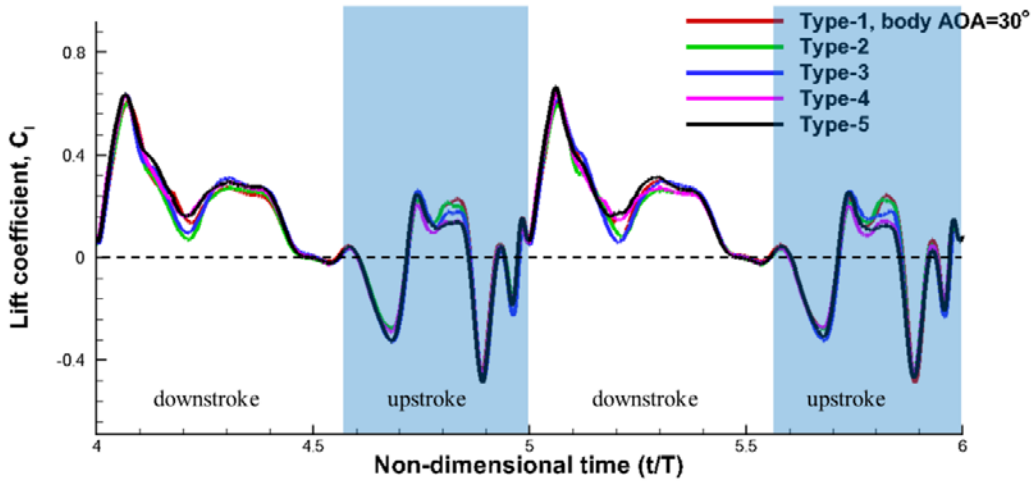

a)

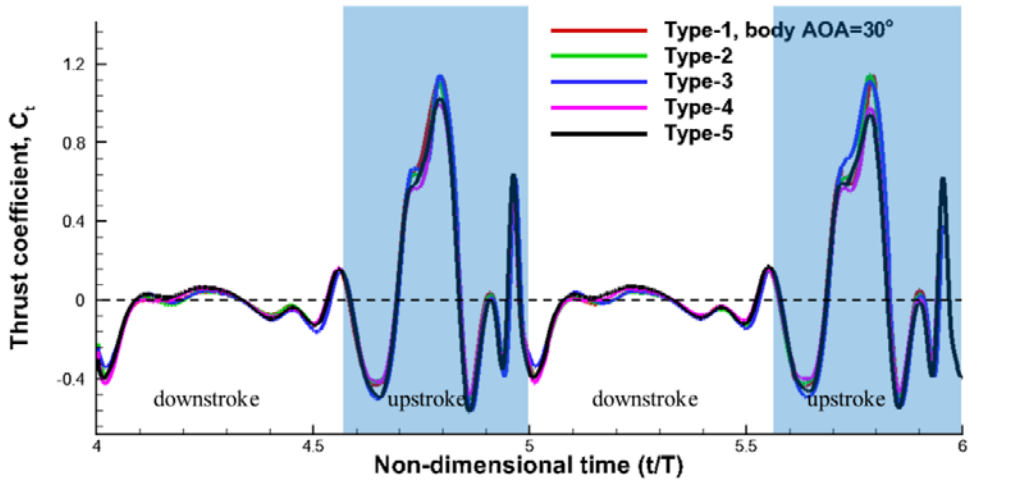

b)

Figure 4.20 Time histories of instantaneous a) lift and b) thrust coefficients according to the wing shape at the body AOA of 30 deg.

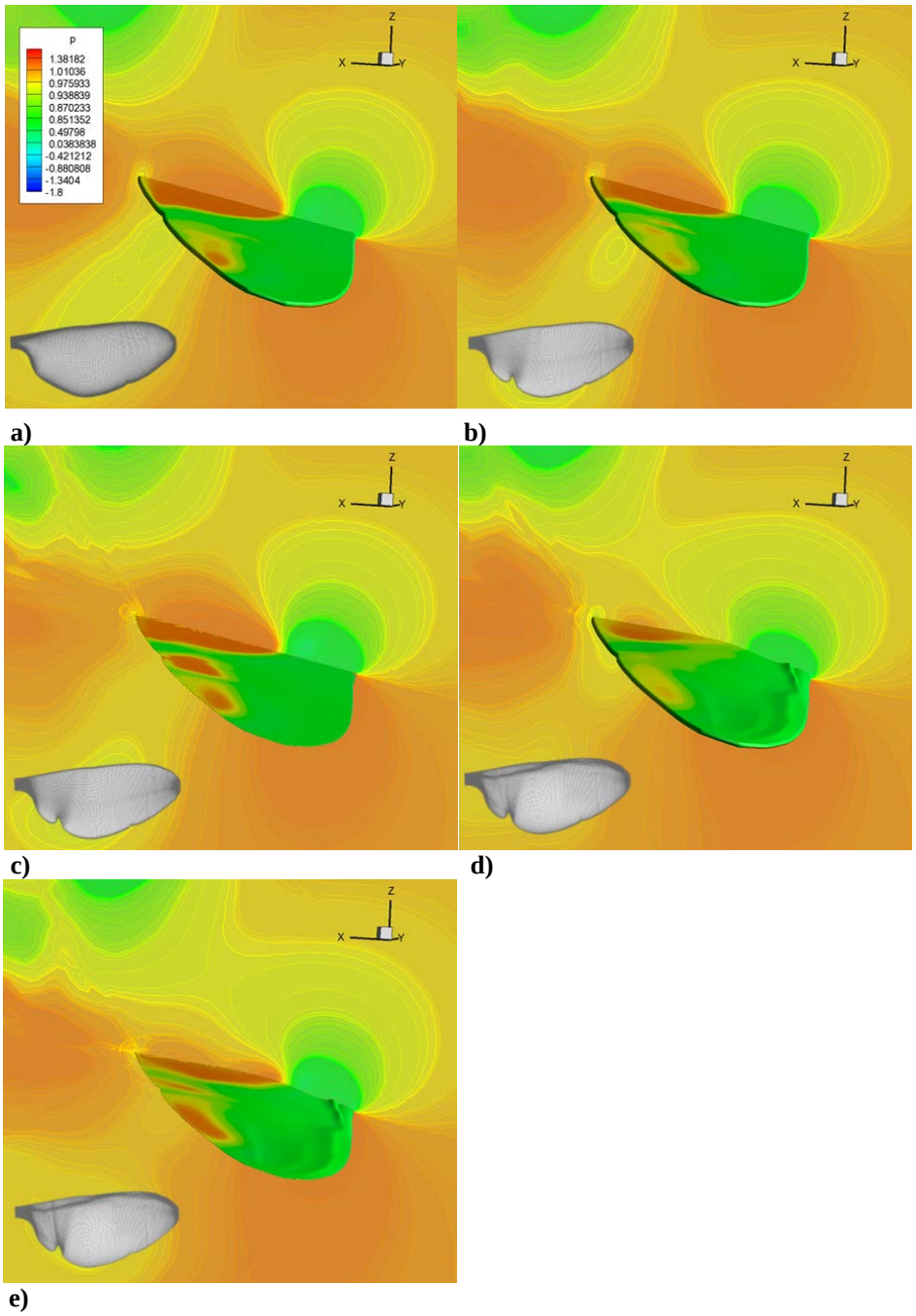

Figure 4.21 Cross-sectional pressure distributions of 5 types of wings at the middle of downstroke: a) type-1, b) type-2, c) type-3, d) type-4, and e) type-5

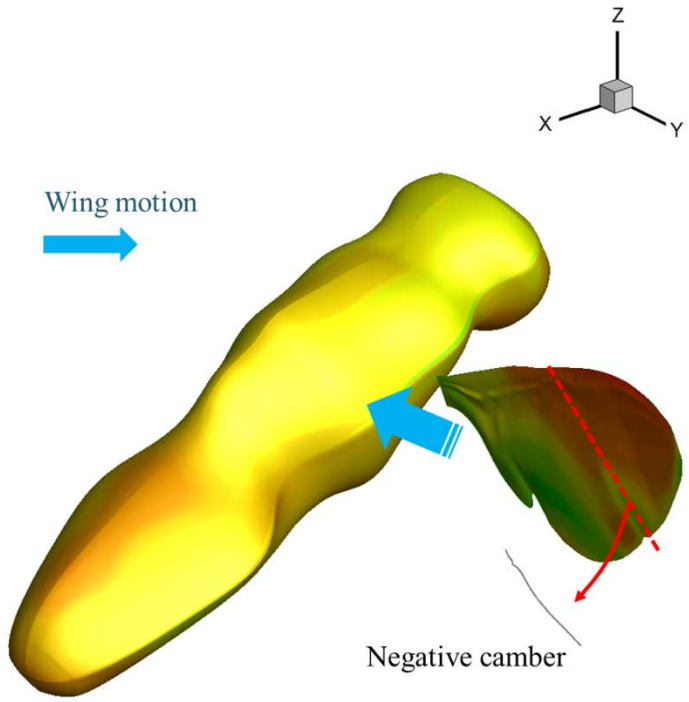

Figure 4.22 Surface pressure of type-5 wing and body at the middle of upstroke.

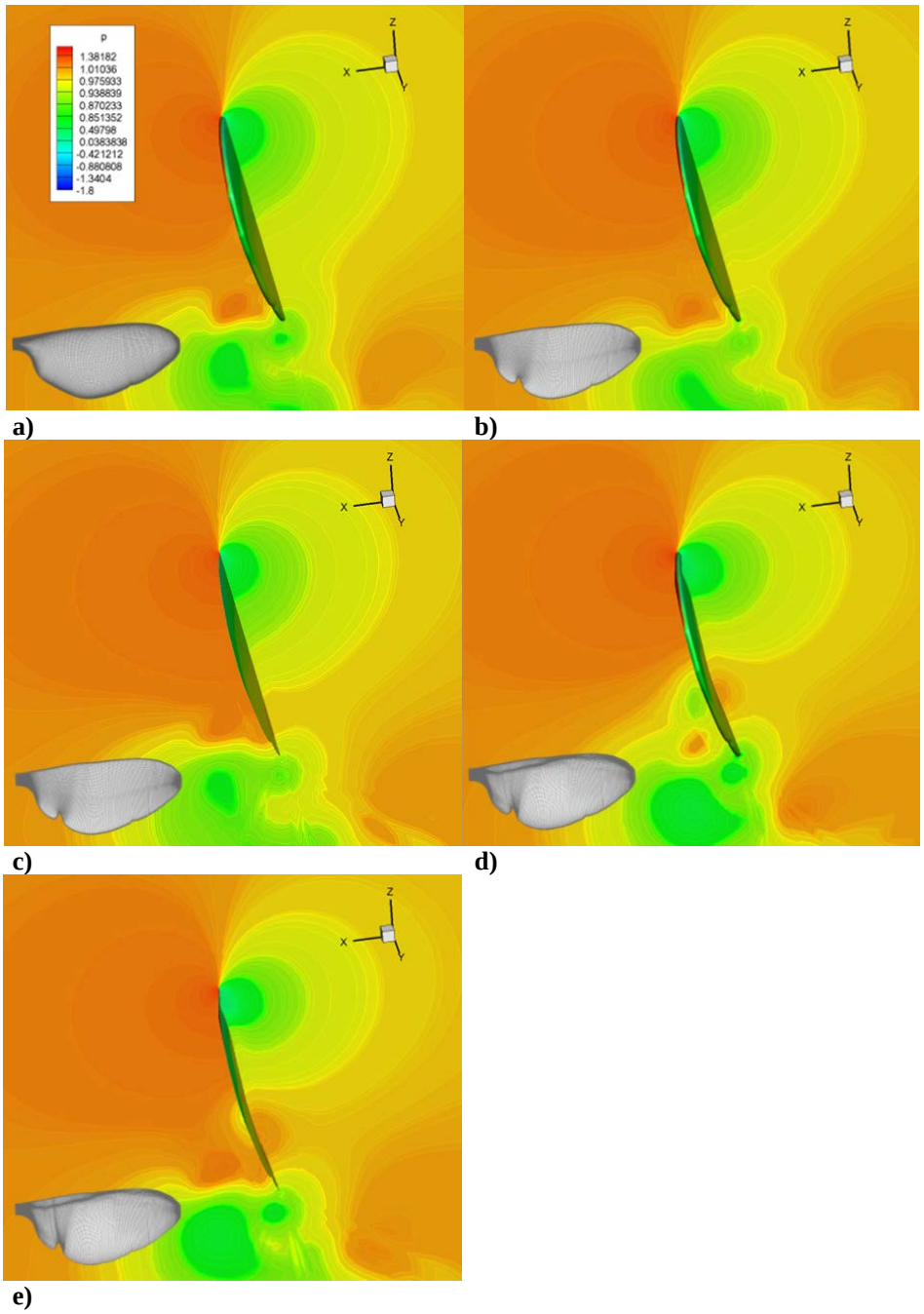

Figure 4.23 Cross-sectional pressure distributions of 5 types of wings at the middle of upstroke: a) type-1, b) type-2, c) type-3, d) type-4, and e) type-5.

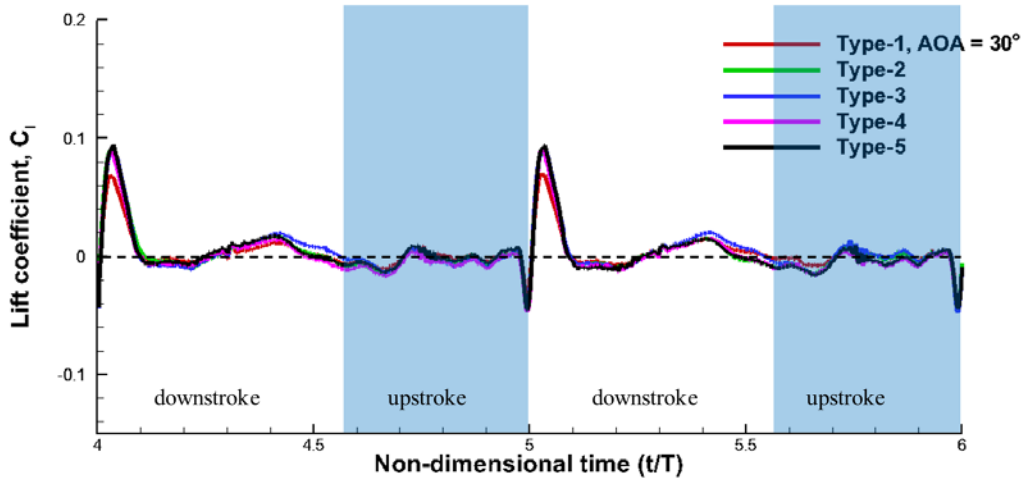

a)

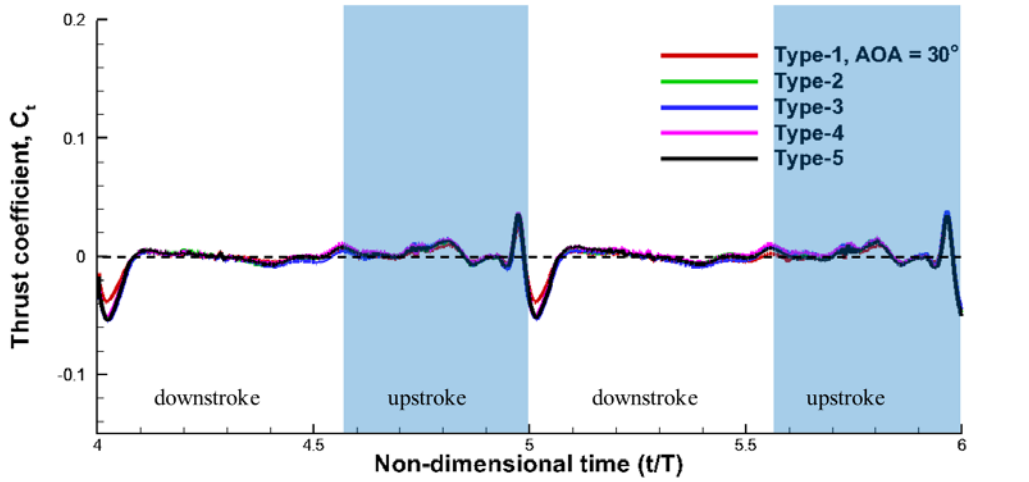

b)

Figure 4.24 Time histories of a) lift and b) thrust coefficients on the body according to the wing shape at 30 deg. AOA.

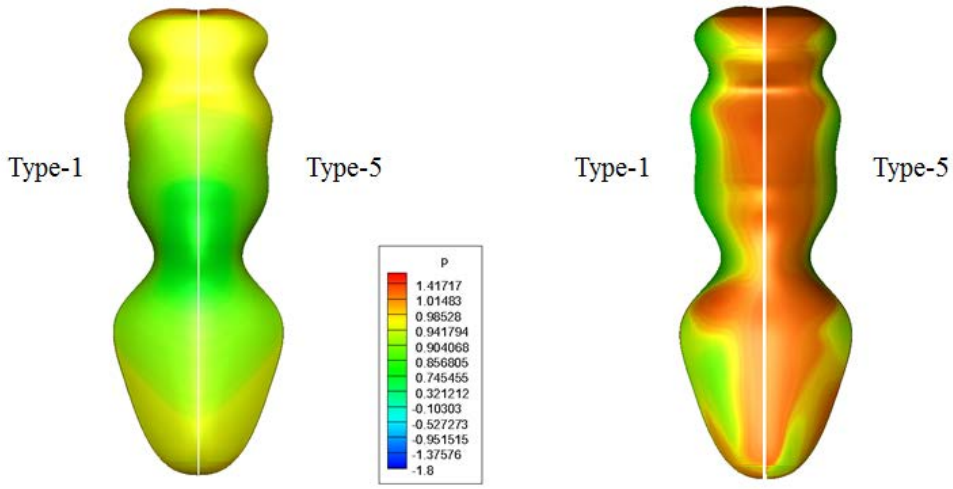

a) **b)**

Figure 4.25 Surface pressure on the body: a) back and b) front.

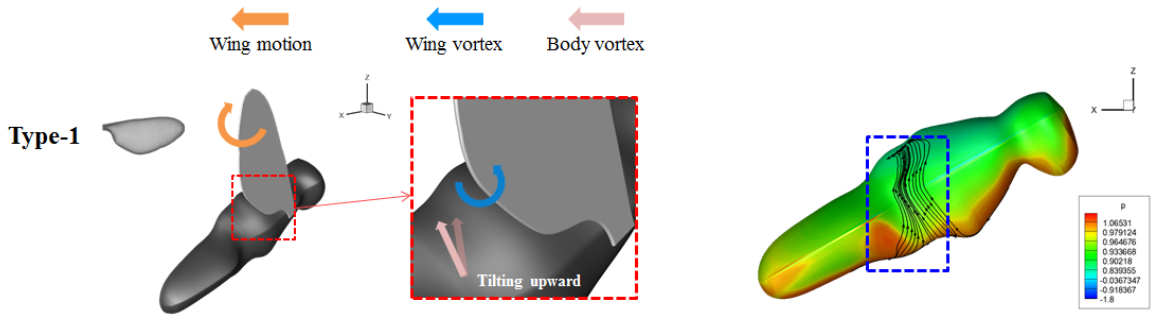

a)

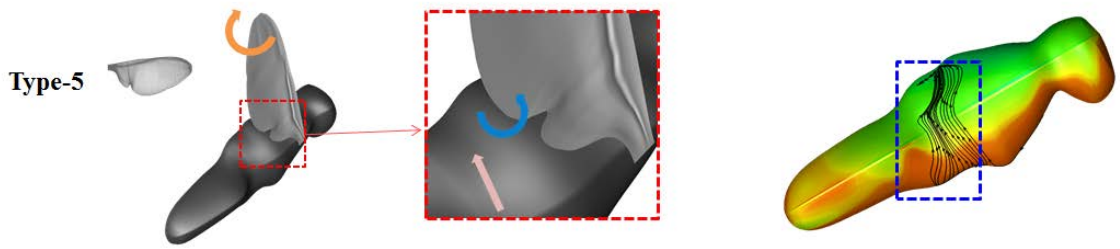

b)

Figure 4.26 Close-up view of vortex direction and pressure contour and streamline on the body between a) type-1 and b) type-5.

국문초록

본 논문에서는 날갯짓 곤충의 전진 비행 시 발생하는 비정상 유동 특성에 관한 수치적 연구를 수행하였다. 날갯짓 곤충의 날개 운동을 해석하기 위하여 검정금파리의 전진모사 비행 실험에서 관찰된 결과를 인용하였다. 본 연구의 선행 연구에서는 검정금파리 날개 운동의 2차원 및 3차원 수치해석을 통해 곤충 비행의 급격한 기동성을 이해하는데 중요한 단서가 되는 매우 흥미롭고 독특한 유동장 특성을 관찰할 수 있었다. 선행 연구의 내용을 바탕으로 본 연구에서는 크게 두 가지 연구 주제에 대해 연구를 수행하였다.

곤충 날갯짓 비행에서 날개와 주위 유체 간의 상호작용은 공력특성을 결정짓는 매우 중요한 요소 중 하나이다. 날개의 구조 유연성이 공력발생에 미치는 영향 파악하고, 곤충 비행에서 발생하는 보다 실제적인 유동 특성을 분석 하기 위해 2차원 유체-구조 연성해석을 수행하였다. 날개의 구조변형을 모사하기 위하여 세가지 형태의 날개 단면을 고려하였다. 그 결과, 유연 구조 날개에서도 선행 연구에서 관찰된 주요 유동 물리 현상 및 공력 발생 패턴이 유사하게 나타남을 확인할 수 있었다. 반면, 구조 변형에 따른 유효 받음각의 변화와 날개 표면에 작용하는 힘 벡터의 방향 변화에 의해 정량적인 공력특성은 세가지 날개에서 서로 다르게 나타났다. 또한 다양한 유동조건에 따른 공력특성 및 물리현상의 변화를 살펴보았고, 그 결과 앞전 와류, 와류 짝 현상, 와류 정체 현상과 같은 대표적인 물리현상이 다양한 유동조건 하에서도 유사하게 발생하는 것을 확인할 수 있었다.

곤충 날갯짓 비행의 정성적인 특성은 2차원 해석을 통해 어느 정도 예측 가능하나, 정량적인 특성을 분석하기 위해서는 3차원 효과를 반드시 고려해야 하며, 이를 위해 3차원 날개-몸통 전체 해석을 수행하였다. 곤충의 날갯짓 비행에서는 날개-와류, 와류-와류, 날개-몸통 상호작용이 나타남을 확인할 수 있었으며, 날개 길이 방향 유동의 존재와 역할, 그리고 복잡한 3차원 와류, 즉 와류 환의 구조를 파악할 수 있었고, 각각의 상호작용을 통해 더욱 복잡한 물리적 현상이 나타남을 확인하였다. 그 중에서 날개-몸통 해석 결과는 날개만 해석한 결과와 정성적으로 유사하나 정량적으로는 차이를 나타냈으며, 이를 통해 곤충의 날갯짓 비행에서 날개-몸통 상호작용 역시 중요한 공력 발생 메커니즘임을 확인할 수 있었다. 또한, 몸통 받음각 및 날개 형상과 같은 기하학적 요소에 대한 파라메트릭 연구를 수행하였으며, 그 결과 역시 정성적으로는 유사하나 정량적으로는 의미있는 차이를 나타냄을 확인할 수 있었다.

곤충 날갯짓 비행에서 관찰된 제자리 비행과 급격한 기동성은 초소형 날갯짓 비행체에 반드시 요구되는 비행 특성이다. 본 연구에서 분석한 곤충 날개의 구조 유연성에 대한 공기역학적 효과는 초소형 날갯짓 비행체 개발과정에서 공력 성능 개선 및 무게 감소 측면에서 유용한 정보를 제공할 것으로 기대된다. 더불어 본 연구에서 관찰된 3차원 날개-몸통-와류 상호작용에 의한 복잡한 유동 구조는 날갯짓 곤충의 급격한 기동성과 조종성을 설명할 수 있는 중요한 단서가 될 것으로 판단된다.

주요어: 전산유체역학, 유체-구조 연성해석, 날갯짓 비행, 비정상 유동, 공력 발생 메커니즘, 날개 운동 궤적, 와류 짝 현상, 와류환, 날갯짓 소형 비행체

학 번: 2009-30870

이 름: 이 근 배